Prediction of light scattering by plane parallel media

by

Bahareh Ramezan pour

A dissertation submitted to the Graduate Faculty of
Auburn University
in partial fulfillment of the
requirements for the Degree of
Doctor of Philosophy

Auburn, Alabama
August 3, 2019

Keywords: Light scattering, Radiative transfer equation, Multiple scattering, Dense particulte media, Polarization, Coherent backscattering

Approved by

Daniel Mackowski, Professor of Mechanical Engineering, Auburn University
Jay Khodadadi, Professor of Mechanical Engineering, Auburn University
Roy Knight, Associate Professor of Mechanical Engineering, Auburn University
Narendra Govil, Professor of Mathematics and Statistics, Auburn University
George Flowers, Dean of the Graduate School, Auburn University

Abstract

The primary motivation of this research is to recognize and establish features of particle deposit reflectivity and absorptivity which have potential for remote detection and characterization of the deposit. In order to interpret measurements generated by remote sensing instruments, one needs to have a detailed understanding of the scattering phenomena and its dependency to physical and chemical properties of the target. The diversity in the particle size, shape, refractive index, and packing density which compose natural and manufactured materials can affect the observable radiometric and polarimetric properties. In this regard, the main purpose of this dissertation is to use numerical simulation techniques to understand how the deposition of particulate material, with known physical, optical, and chemical properties alters the electromagnetic scattering characteristic of the deposit.

This research examines exact formulations for multiple particle scattering, coupled with up–to–date computational techniques, to directly simulate the absorption and scattering properties of particle deposits. The particulate deposits are numerically simulated using Monte Carlo methods with known distribution functions and microscopic configurations of films. One method used for predicting simulated deposit radiative properties is based on an exact superposition solution to Maxwell's time harmonic wave equations for a deposit of spherical particles that are exposed to a plane incident wave. We use a FORTRAN90 implementation of this solution (the Multiple Sphere T Matrix (MSTM) code), coupled with parallel computational platforms, to directly simulate the reflection from particle layers via a configurational averaging strategy. Another method used for the simulation is the Plane Wave Plane Parallel (PWPP) formulation, which also provides an accurate solution

to Maxwell's time harmonic wave equations for discretely inhomogeneous plane parallel media. The PWPP method, that is based on the discrete dipole approximation (DDA), can directly simulate the polarimetric scattering properties of plane parallel layers of random particulate media. In this technique the medium is modeled as a periodic lattice of unit cells extending infinitely in the lateral directions with finite or infinite depth. The PWPP method is also used to perform comprehensive computational examinations of the effect of pigment particle physical structure, chemical composition, and volume concentration on the spectral reflectance and transmittance properties of pigment–binder coatings. We also used the phenomenological radiative transfer theory (RTT) to predict scattering properties of electromagnetic radiation in media composed of randomly and sparsely distributed particles. Analytical studies of the phenomenological radiative transfer equation (RTE) have formed a separate branch of electromagnetic theory. The adding and doubling method is used as the numerical solution to the scalar and vector RTE for a plane—parallel configuration. Mie theory is used in our RTE model to predict the extinction coefficient, albedo, and scattering phase function of the particles.

Acknowledgments

During my time here at Auburn University I have been fortunate to work with many wonderful people without whom I would not be able to complete this journey.

First and foremost, I would like to express my sincere gratitude to my advisor Professor Daniel Mackowski, who has been a friend and mentor. In addition to financial support during my Ph.D. Dr. Mackowski has provided me unwavering support and invaluable guidance and insight. His encouragement, patience, enthusiasm, and immense knowledge helped me in the journey towards this degree and will inspire me to pursue my goals.

I have great pleasure in acknowledging my gratitude to my my thesis committee: Prof. Khodadadi, Prof. Knight, and Prof Govil for their practical comments, helpful contributions, and bearing with me to write this dissertation.

I would like to express my deepest appreciation to my source of my strength, my parents Eshagh and Frouzandeh, my siblings, Negar and Behnam, my grandparents Fakhri and Ali, and last but not least my ant Firouzeh. Their love and support from miles away are always with me in whatever I pursue. They all have been missed so much and I hope I will be able to meet them soon.

My acknowledgment would be inadequate without thanking my dearest friends, Zahra and Majid. Their tremendous encouragement and support helped me to reach this stage in my life.

Table of Contents

List of Figures

List of Tables

Chapter 1

Introduction, overview, theory, and methods.

1.1 Introduction

Light scattering is an important phenomenon in our daily life and it's applications are all around us. It is the underlying physical principle responsible for blue skies, rainbows, coronas, and mirages. Indeed, light scattering accounts for most optical phenomena in the earth's atmosphere. The interaction between light and matters occurs due to the heterogeneity in the molecular scale of media. All systems composed of basic elements (atoms and molecules) are considered as heterogeneous. As a result, almost all particles and objects scatter light which means any source of electromagnetic radiation (i.e. heat radiation, X-rays, microwaves, radio waves) change their intensity or polarization state as they propagate in media.

To understand scattering, we must look at matter at the microscopic level. All objects are composed of electric charges which can be excited by an oscillating beam of light. If these charges oscillate with the same frequency of the incident light, secondary radiation fields are generated by an individual charge. The superposition of these secondary electromagnetic waves is called electromagnetic scattered waves. In addition, scattering phenomenon is usually accompanied by absorption. If the electric charges do not vibrate with the same phase of the source light, the electromagnetic energy of excited fields transform into other types of energy such as thermal. In other words, dissipation of energy occurs in this process.

This basic principle implies that a beam of light attenuates as it propagates through a medium by scattering and absorption. So extinction of an incident wave can be defined as:

$$Extinction = Scattering + Absorption \tag{1.1}$$

Careful observation of the scattering phenomena indicates that electromagnetic light scattering is a complex phenomenon. An object is composed of a large number of discrete elementary charges. These particles generate secondary radiation waves which vibrate all other charges. In addition, the phase difference of all the secondary waves should be considered numerically in attempts to compute their superposition. Fortunately, there are various approaches that can be used to solve electromagnetic scattering problem.

Some of these techniques can be addressed as direct simulations. Such methods provide a superposition solution to the Maxwell's wave equations for systems with microscopically detailed configurations. The above discussion makes it clear that a large number of degrees of freedoms are involved in these methods, so direct techniques are computationally intensive by definition.

In contrast to direct methods, there are phenomenological approaches to solve electromagnetic scattering. These approaches assume that a system is composed of a large enough number of particles that radiative continuum conditions can be applied to the system. Phenomenological radiative transfer theory (RTT) provides solutions to the macroscopically electromagnetic problems using various numerical methods.

This chapter provide a thorough description of RTT and other numerical approaches to solve radiative transfer equation (RTE), considering their practical limitations in terms of the object's optical properties and morphology.

1.2 Radiative Transfer Theory

Radiative transfer theory (RTT) describes the interaction of a collimated light with a scattering and absorbing medium. The physical basis of the phenomenological RT theory is dependent on the conservation of energy of light propagating through an inhomogeneous medium. The radiative transfer equation (RTE) was for the first time applied in the atmospheric science and it has been used to deal with the multiple scattering of light by discrete random media for many decades [12, 9, 29, 57]. In the past decade, the RTE has been extensively used in several fields, such as biomedical, nuclear physics, geophysics, oceanography, astrophysics, and remote sensing. In RTE the electromagnetic radiation is treated as light rays that consist of light particles or photons. This equation is represented by an integro–differential equation describing propagation of the radiation intensity considering boundary conditions.

The electromagnetic radiation is represented by oscillating plane electromagnetic waves and transfers its energy as it propagates in media. However, traveling in the vacuum has no effects on its energy. In other words, energy and/or polarization state of an incident beam does not change through vacuum. Consequently, the energy equation in a homogeneous vacuum can be described by:

$$\frac{dI_\lambda(\mu,\varphi)}{ds} = 0, \tag{1.2}$$

where I_λ a is the specific intensity at the wavelength λ in the direction of ds (ds is an infinitesimal path element along the ray) in a cone of unit solid angle along direction μ and ϕ (μ is the cosine of the polar angle and ϕ is the azimuthal angle). The polar angle is defined such that it is positive in the upward hemisphere. We should note that to describe a monochromatic electromagnetic wave the information about the state of polarization is required in addition to the irradiance measurements. Polarimetric characteristics of the scattered waves

have more data compared to the intensity measurements. Measured polarization contain information about production mechanism of the scattered waves and propagation through objects. Polarization describes the path the electric vector field follows in the plane as the wave propagates. In general this path is an ellipse. So considering a plane wave vibrating in a ellipse plane, four quantities are needed to completely characterize the electric field state of the plane wave or we can say the polarization state can be represented by four parameters. These parameters are called Stokes parameters: I, Q, U, and V and all different polarizations conditions can be describes by these Stokes parameters.

The origin of the electromagnetic scattering phenomena is an inhomogeneity of matter or discrete elementary electric charges forming an object. The particles in the path of the incident radiation reradiate or diminish energy from the beam by scattering or absorption. The change of I_λ as it propagates along a path d_s in the presence of an object:

$$\frac{dI_\lambda(\mu,\varphi)}{ds} = -(k_{s\lambda}+k_{a\lambda})\rho I_\lambda(\mu,\varphi) + \frac{k_{s\lambda}\rho}{4\pi}\int_0^{2\pi}\int_{-1}^{1} P(\mu^t,\varphi^t\rightarrow\mu,\varphi)I(\mu^t,\varphi^t)d\mu^t d\varphi^t, \tag{1.3}$$

The energy of the incident beam changes along the path due to its interaction with the matter. This interaction includes absorption and scattering by particles along the incident ray as well as scattered radiation fields by other particles in the object toward the incident beam.

Absorption and the first order scattering (i.e., part of incident light scattered by scatterers for the first time) by particles diminish the incident energy. On the other hand, the scattered fields that merge into the incident ray acts as a source and causes an incremental increase in the incident radiation energy. In the above equation ka and ks are absorption and scattering coefficients respectively. P is the so-called single phase function and it is

defined as probability of scattering of a beam in the direction defined by μ and φ into the new direction μ' and φ'. Dividing both side of equation 1.3 by $(k_a + k_s)$ gives us:

$$\mu \frac{dI_\lambda(\mu,\varphi)}{d\tau} = I_\lambda(\mu,\varphi) - \frac{\omega_0}{4\pi} \int_0^{2\pi} \int_{-1}^{1} P(\mu^t, \varphi^t \to \mu, \varphi) I(\mu^t, \varphi^t) d\mu^t d\varphi^t, \tag{1.4}$$

where ω_0 is the single scattering albedo that is equal to $k_s/(k_a + k_s)$ and τ is the optical thickness.

There is no doubt that vector RTE (VRTE) has more applications in science and engineering since polarimetric characteristic of scattered fields contain more precise information and specific data. So far we did not take into account the state of polarization in our computations and formulations. In order to discuss numerical methods to solve VRTE, we must describe the state of polarization before we go further.

Note that to represent the polarization effects in the RTE formulas, the intensity number is replaced by a Stokes parameters vector:

$$I = \begin{pmatrix} I \\ Q \\ U \\ V \end{pmatrix} \tag{1.5}$$

where I, Q, U, and V (i.e, Stokes parameters) can be related by:

$$I^2 = Q^2 + U^2 + V^2 \tag{1.6}$$

The above discussion implies that the integro–differential radiative transfer equation is an exceedingly complex system of equations and is impractical to be solved analytically. So numerical techniques and simplifications are required to predict scattering properties using

the RTE. In order to demonstrate the computational aspects of the phenomenological RTT, we described some numerical approaches to solve the radiative transfer equation.

1.3 Different numerical methods to solve the RTE

As mentioned earlier, the radiative transfer equation has been become one of the legitimate methodologies of the classical electromagnetic scattering which has been widely used in recent decades. However, solving the general form of the radiative transfer equation, either the integral form or integro–differential form, requires some primary assumptions. The most standard assumptions in the RTT is defining the scattering medium as a plane parallel system which is extending infinitely in horizontal directions. The light source is illuminated by plane electromagnetic waves or parallel quasi–monochromatic radiation fields from above or bottom.

A variety of numeral techniques are available to solve the radiative transfer equation. Most of these methods are designed for computing multiple scattering of unpolarized or polarized light in atmosphere considering the plane parallel geometry. The oldest literatures and studies that exist on this subject are in the case of Rayleigh scattering to calculate reflected radiation fields by aerosols [12, 129]. However, not all the methods are restricted to the Rayleigh scattering conditions such as FN, discrete ordinates, spherical harmonic, adding doubling, Monte Carlo, and fast invariant imbedding methods. All these techniques has been modified to take the polarization effects into account. In the following section we discuss a summary of some of these methods.

One method for solving radiative transfer in plan-parallel media is called the F_N method, and was first introduced by Siewert in 1978 to predict radiation intensities by homogeneous plane–parallel atmosphere. Later the FN technique was extended to solve neutron transport problems [119, 43]. In 1980 Siewert introduced the F_N method for atmospheric problem [83, 21] where polarization is ignored. To solve the transport equation including the polarization

effects, a collocation technique is applied on singular integral equations. It is necessary, in this technique, to compute all of the discrete eigenvalues of the transport equation in order to derive a linear system of equations (generally sparse), which has to be satisfied at the so-called collocation points. Solving this system then leads to the solution of the RTE in plane parallel media (such as the atmosphere.)

Another method that applies Fourier decomposition to radiative transfer equation is called the discrete ordinates method. In this method all the integrals over all coordinates are replaced by finite summation of quadrature points. The basis of this method was first introduced by Chandrasekhar [12] that consider the media as a stack of homogeneous layers which leads to a system of differential equations of the first order. This system can be solved by considering continuity in the interference between layers and satisfying the boundary conditions of incident and scattering fields at target boundaries. More details and comparison with other numerical methods are available in [135, 115, 114, 118]. Although this method is popular, it sometimes gives errors and unreasonable results due to limited resolution of scattering angles. In addition, it is not accurate and efficient for optically thick medium.

The spherical harmonic method, which is also called the P_L-approximation, is another technique to evaluate multiple scattering in a plane parallel media. Davison [18] and Lenoble [71] introduced this method for the first time when the polarization effects were ignored. Similar to the discrete ordinates method, Fourier decomposition is applied to the RTE. A system of linear ordinary differential equations is derived by expanding the intensity vector using Legendre functions. In this system of equations, each constant coefficient corresponds to each homogeneous layer of the plane parallel medium. Then one can solve these equations by applying the boundary conditions of scattering and incident fields at reflected surfaces and the continuity across the layer interfaces [37, 2]. Note that this technique has some restrictions for optically thin media.

Another common approximation method to solve RTE is the Monte Carlo method. The idea of this technique is to track the path of each photon through the medium and locate them at each scattering and absorption interactions, then follow them to another event inside the absorbing and scattering medium. The simulation is based on the random numbers and directions. The principles of the Monte Carlo technique are explained in detail s which can be found in previous works [10, 139, 33, 61]. The event points are determined by sampling the probability distribution based on the albedo and phase function. This process is repeated until the net distribution of all samples generates a realistic estimation, but to achieve an accurate result a large number of photons should be emitted and captured to make the error or Monte Carlo noise small enough so that each photon has a minor contribution to the net output.

The fast invariant imbedding method also can be used to calculate the reflection matrix for a plane parallel medium with a finite thickness. Fundamentally, this method describes the variation of reflection as a function of the optical thickness. Sato et al. [112] introduced this technique for the first time when where the polarization is ignored and Mishchenko [87] extended it for polarized light. Utilizing quadrature formula for the integrals over spherical directions in the radiative transfer equation leads to a system of differential equations that can be solved by predictor–corrector technique.

1.4 Adding and doubling method

1.4.1 Principle of the adding and doubling method

A variety of numerical techniques are available to solve the RTE which describe radiative energy of polarized light in an absorbing and scattering plane parallel medium. However, as discussed earlier, most of these approaches impose restrictions on the medium properties or incoming light. One of the most popular methods to solve the radiative transfer equation

in plane parallel media is adding and doubling. This method was originally introduced by Van de Hults in 1963 [128] for unpolarized light; in 1971 Hansen [46, 47] and Hovenier [55] extended this method to take polarization into account. The method was then modified to consider multiple scattering effects for applications in atmospheric science [129]. There have been more comprehensive studies and improvements for this method which make it the most efficient, exact, and easy to implement to date.

We should note that the adding and doubling method is exact in the sense that the accuracy of the simulation outputs is affected only by the accuracy of the input data. There is no restriction regarding the target thickness and one can compute the scattering properties for a plane parallel deposit with any finite optical thickness by considering the slab as a pile of thin layers.

In order to calculate the scattering properties by the adding and doubling method, we suppose that the reflection and transmission of two thin homogenous layer is known. Then one can calculate scattering properties for the whole target. Note that this technique is referred to as the doubling method if all the sublayers are identical and it is called adding if different sublayers are added to each other.

In general, the adding and doubling method can be considered as an exact and efficient method to study the effects of multiple scattering in randomly horizontal media. It has been successfully applied in biological, atmospheric, and oceanic sciences. Also, it has many applications in remote sensing to calculate reflectance from the ground, the air, and space. Since it is an accurate and fast method, it has been used in inverse scheme of the RTE to generate optical properties of the turbid media [108, 107].

For a basic understanding of the adding and doubling method, we consider a plane parallel inhomogeneous target with arbitrary thickness. The slab is illuminated evenly from the top; the intensity of the light does not vary from point to point at the top surface. Also note that there are no internal sources of radiation fields and no boundaries in the

horizontal direction. We shall now divide the deposit into layers with small optical thickness in the sense that each layer can be considered as a homogeneous target in which the single scattering albedo and phase function are independent of the position and they do not change over the target thickness.

Also, it is worth mentioning that optical thickness is a dimensionless quantity representing the physical thickness times extinction coefficient; in other word it gives a measurement of how much extinction occurs for radiation field passing some distance in a medium. In this study, optical thickness which is denoted by τ is measured from the top boundary and it increases downward.

1.4.2 Layer Initialization

As mentioned earlier, solving the radiative transfer equation by the adding and doubling procedure involves knowledge of the reflection and transmission for the first two layers. Choosing an accurate method to calculate the scattering properties of these layers is another important decision in the adding and doubling technique, because any source of numerical errors in the initial layers are growing as we double the layer in each step of the doubling the layer and minor inaccuracy would result in a huge error at the end.

Several methods have been used to compute the reflection and transmission of the initial layers like diamond initialization [136], successive scattering [56], and infinitesimal generator [44]. Numerical experiments have shown that the most accurate and convenient way to begin this computations is with an optically thin layer in the sense that multiple scattering effects can be neglected. Hansen [48, 46] showed that the reflection and transmission by a thin deposit considering the single scattering can be calculated by the following formulas:

$$\mathbf{R_1}(\tau;\mu,\mu_0,\phi-\phi_0)=\frac{\tilde{\omega}_0}{4(\mu+\mu_0)}\left\{1-\exp\left[-\tau\left(\frac{1}{\mu}+\frac{1}{\mu_0}\right)\right]\right\}\times\mathbf{P}(\mu,\mu_0,\phi-\phi_0), \qquad (1.7)$$

$$\mathbf{T_1}(\tau;\mu,\mu_0,\phi-\phi_0)=\frac{\tilde{\omega}_0}{4(\mu-\mu_0)}\left[\exp\left(\frac{-\tau}{\mu}\right)-\exp\left(\frac{-\tau}{\mu_0}\right)\right]\times\mathbf{P}(\mu,\mu_0,\phi-\phi_0),\ \text{if}\ \mu\neq\mu_0, \tag{1.8}$$

$$\mathbf{T_1}(\tau;\mu,\mu_0,\phi-\phi_0)=\frac{\tilde{\omega}_0\tau}{4\mu_0^2}\exp\left[\frac{-\tau}{\mu_0}\right]\mathbf{P}(\mu,\mu_0,\phi-\phi_0),\ \text{if}\ \mu=\mu_0, \tag{1.9}$$

where $P(\mu,\mu_0,\phi-\phi_0)$ is the phase matrix and ω_0 is single scattering albedo. Phase function is calculated by the famous Mie theory. Each element in this matrix depends on the scattering angle, α, which is given by:

$$\cos(\alpha)=\pm\mu*\mu_0+(1-\mu^2)^{1/2}*+(1-\mu_0^2)^{1/2}*\cos(\phi-\phi_0), \tag{1.10}$$

1.4.3 The doubling method

In 1963, Van de Hulst [128] showed that the reflection and transmission of any arbitrary thickness slab can be calculated by dividing it to multiple thin layers. The adding and doubling technique is based on the knowledge of the reflected and transmitted fields for each layer. The method then starts with computing the scattering properties of a layer which is composed of two initial thin layers. Suppose that the only light source is present illuminating the target from the bottom and there is no internal radiation. Based on the equations 1.7, 1.8, and 1.9 one can calculate the reflection and transmission for the first two layers and now suppose we placed the layers on top of each other. The goal is to compute the scattering fields for the combined layer. The situation is schematically shown in Fig2.1.

As it can be seen in the figure (Fig2.1), the light is reflected back and between the layers and at each reflection event a part of the radiation filed is lost. We should mention that absorption would diminish the light energy as well in the absorbing medium. So a series of reflection and transmission happens in the layers but it will converge due to the

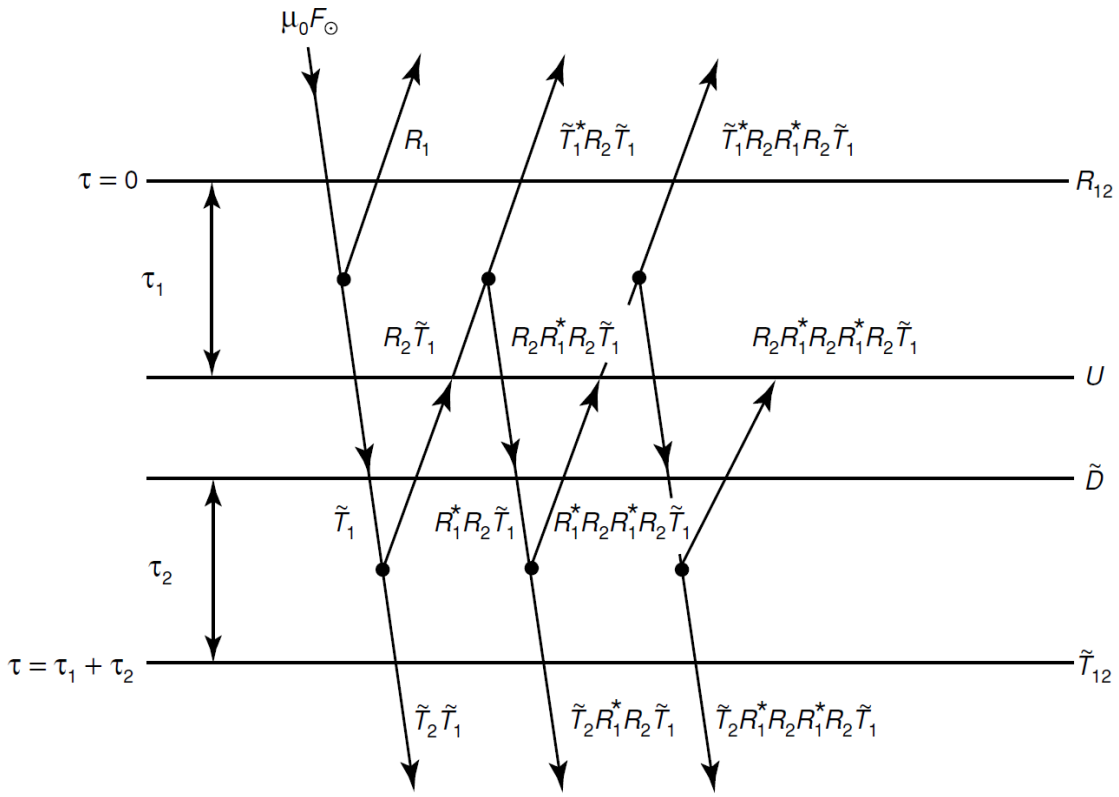

Figure 1.1: Schematic represents the doubling method. Two layers with known scattering fields and optical thicknesses of τ_1 and τ_2 are placed on top of the other. The incident light is reflected and transmitted upwards and downwards in multiple scattering events by the combined layer (K. N. Liou, 2002 [72])

physical reason. Note that the convergence is faster in absorbing targets. So many order of scattering take place in each layer. One can calculate the intensity of the light that passes the interference for the first time by the following formula:

$$\mathbf{I}^{(1)}(b', \mu, \varphi) = e^{-b'/\mu}\mathbf{I}_{it}(\mu, \varphi) + \frac{1}{\pi}\int_0^1 \mu' d\mu' \int_0^{2\pi} d\varphi' \mathbf{T}'(\mu, \mu', \varphi - \varphi')\mathbf{I}_{it}(\mu', \varphi'), \tag{1.11}$$

Then, if this field is reflected by the lower layer, the intensity coming to the upper layer will be equivalent to:

$$\mathbf{I}^{(2)}(b', \mu, \varphi) = \frac{1}{\pi}\int_0^1 \mu' d\mu' \int_0^{2\pi} d\varphi' \mathbf{R}''(\mu, \mu', \varphi - \varphi')\mathbf{I}^{(1)}(b', \mu', \varphi'), \tag{1.12}$$

A portion of $I^{(2)}$ can be reflected downward with the intensity of:

$$\mathbf{I}^{(3)}(b', \mu, \varphi) = \frac{1}{\pi} \int_0^1 \mu' d\mu' \int_0^{2\pi} d\varphi' \mathbf{R}^{*\prime}(\mu, \mu', \varphi - \varphi') \mathbf{I}^{(2)}(b', \mu', \varphi'), \tag{1.13}$$

where $R^{*'}$ and $T^{*'}$ are reflections and transmissions of the first layer respectively when the light is incident from bottom. However layers are considered to be homogeneous and identical, so they can be simply computed by the following symmetry relations:

$$\mathbf{R}^*(\mu, \mu_0, \varphi - \varphi_0) = \mathbf{R}(\mu, \mu_0, \varphi_0 - \varphi) \tag{1.14}$$

$$\mathbf{T}^*(\mu, \mu_0, \varphi - \varphi_0) = \mathbf{T}(\mu, \mu_0, \varphi_0 - \varphi) \tag{1.15}$$

This procedure will repeat again and again, so the incident beam will be scattered infinite times by the layers. Each time that the light reflects or passes the interface, its intensity decreases due to reflection, transmission, and absorption in absorbing media. Due to this physical phenomenon, this infinite series of scattering will converge after some terms or after a small number of reflections and transmissions. We can simplify equations by calculating a new parameter Q:

$$\mathbf{Q}_1(\mu, \mu_0, \varphi - \varphi_0) = \frac{1}{\pi} \int_0^1 \mu' d\mu' \int_0^{2\pi} d\varphi' \mathbf{R}^{*\prime}(\mu, \mu', \varphi - \varphi') \mathbf{R}''(\mu', \mu_0, \varphi' - \varphi_0), \tag{1.16}$$

$$\mathbf{Q}_{p+1}(\mu, \mu_0, \varphi - \varphi_0) = \frac{1}{\pi} \int_0^1 \mu' d\mu' \int_0^{2\pi} d\varphi' \mathbf{Q}_1(\mu, \mu', \varphi - \varphi') \mathbf{Q}_p(\mu', \mu_0, \varphi' - \varphi_0), \tag{1.17}$$

$$\mathbf{Q}(\mu,\mu_0,\varphi-\varphi_0)=\sum_{p=1}^{\infty}\mathbf{Q}_p(\mu,\mu_0,\varphi-\varphi_0), \tag{1.18}$$

Hence the downward reflection intensity from the upper layer can be rewritten as:

$$\mathbf{I}^{(3)}(b',\mu,\varphi)=\frac{1}{\pi}\int_0^1\mu' d\mu'\int_0^{2\pi}d\varphi'\mathbf{Q}_1(\mu,\mu',\varphi-\varphi')\mathbf{I}^{(1)}(b',\mu',\varphi'), \tag{1.19}$$

The reflection from the lower layer that passes the interface for the second time:

$$\begin{aligned}\mathbf{I}^{(5)}(b',\mu,\varphi)=&\frac{1}{\pi}\int_0^1\mu' d\mu'\int_0^{2\pi}d\varphi'\mathbf{Q}_1(\mu,\mu',\varphi-\varphi')\mathbf{I}^{(3)}(b',\mu',\varphi')=\\&\frac{1}{\pi}\int_0^1\mu'' d\mu''\int_0^{2\pi}d\varphi''\mathbf{Q}_1(\mu,\mu'',\varphi-\varphi'')\times\frac{1}{\pi}\int_0^1\mu' d\mu'\int_0^{2\pi}d\varphi'\mathbf{Q}_1(\mu'',\mu',\varphi''-\varphi')\mathbf{I}^{(1)}(b',\mu',\varphi'),\end{aligned} \tag{1.20}$$

Likewise, all the reflection and transmission fields can be calculated based on the Q parameter. As shown by the adding Equations 1.16 to 1.20 downward and upward radiation fields at the interface of the combined layer can be employed in the form:

$$\begin{aligned}\mathbf{D}(b',\mu,\mu_0,\varphi-\varphi_0)=&\mathbf{T}'(\mu,\mu_0,\varphi-\varphi_0)+e^{-b'/\mu_0}\mathbf{Q}(\mu,\mu_0,\varphi-\varphi_0)\\&+\frac{1}{\pi}\int_0^1\mu' d\mu'\int_0^{2\pi}d\varphi'\mathbf{Q}(\mu,\mu',\varphi-\varphi')\mathbf{T}'(\mu',\mu_0,\varphi'-\varphi_0),\end{aligned} \tag{1.21}$$

$$\begin{aligned}\mathbf{U}(b',\mu,\mu_0,\varphi-\varphi_0)=&e^{-b'/\mu_0}\mathbf{R}''(\mu,\mu_0,\varphi-\varphi_0)\\&+\frac{1}{\pi}\int_0^1\mu' d\mu'\int_0^{2\pi}d\varphi'\mathbf{R}''(\mu,\mu',\varphi-\varphi')\mathbf{D}(b',\mu',\mu_0,\varphi'-\varphi_0),\end{aligned} \tag{1.22}$$

Now, we can easily calculate the reflection and the transmission of the combined layer using the following equations:

$$\begin{aligned}\mathbf{R}(\mu,\mu_0,\varphi-\varphi_0) =&\mathbf{R}'(\mu,\mu_0,\varphi-\varphi_0)+e^{-b'/\mu_0}\mathbf{U}(b',\mu,\mu_0,\varphi-\varphi_0)\\ &+\frac{1}{\pi}\int_0^1\mu' d\mu'\int_0^{2\pi}d\varphi'\mathbf{T}^{*\prime}(\mu,\mu',\varphi-\varphi')\mathbf{U}(b',\mu',\mu_0,\varphi'-\varphi_0),\end{aligned} \tag{1.23}$$

$$\begin{aligned}\mathbf{T}(\mu,\mu_0,\varphi-\varphi_0) =&e^{-b''/\mu}\mathbf{D}(b',\mu,\mu_0,\varphi-\varphi_0)+e^{-b'/\mu_0}\mathbf{T}''(\mu,\mu_0,\varphi-\varphi_0)\\ &+\frac{1}{\pi}\int_0^1\mu' d\mu'\int_0^{2\pi}d\varphi'\mathbf{T}''(\mu,\mu',\varphi-\varphi')\mathbf{D}(b',\mu',\mu_0,\varphi'-\varphi_0),\end{aligned} \tag{1.24}$$

The first term in above equation, Equ.1.24, represents the unscattered part of incident field that passes the slab directly. So one can use the equations 1.23 and 1.24 to compute the reflection and transmission matrices for the combined layer based on the scattering properties of each layer separately. Then, all these steps can be repeated over and over until the desire thickness is reached.

1.4.4 Computational and numerical strategies

To solve all adding equations in the last section, we need to integrate over polar angles (theta and phi). To evaluate these integrations over azimuth and zenith angles, we need to use numerical approaches. In this study, the azimuthal dependency were evaluated numerically using quadrature. This means that all integration over μ and ϕ in above equations are converted to a finite sum which is shown mathematically by the following formulas:

$$\int_0^1 d\mu f(\mu)=\sum_{i=1}^{n}\omega_i f(\mu_i), \tag{1.25}$$

where μ_1, μ_2, μ_3, ...,μ_n are quadrature points calculated by Radau quadrature formula and ω_i represents weight function corresponding to μ_i.

The accuracy of this numerical approach strongly depends on the number of quadrature points (n) in Equ. 1.25. In other words, the more points used, the more precise results are obtained. To evaluate the integration over zenith angles, we converted the integration to the sum of equidistant points in the range of 0 to 360. This numerical approach can be written as:

$$\int_0^1 d\phi f(\phi) = \sum_{i=1}^{m} \omega_i f(\phi_i), \tag{1.26}$$

where ω_1, ω_2 … ω_n are weight functions corresponding to points in the ϕ direction.

It should be noted that after converting integrals to sums over quadrature and zenith points, the above equations can be viewed as a matrix multiplications of $m \times n$ by $m \times n$, in which each element represents scattering at μ and ϕ directions corresponding to incident light in μ_0 and ϕ_0 angles when polarization is ignored. Also, each element in the reflection or transmission super-matrices is replaced by a 4×4 matrix when polarization effects analyses are desired [19]. Therefore, all the above operations and equations can be replaced in terms of super-matrices:

$$\mathbf{Q}_1 = \mathbf{R}'^{*}\mathbf{R}'', \tag{1.27}$$

$$\mathbf{Q}_{p+1} = \mathbf{Q}_1\mathbf{Q}_p, \tag{1.28}$$

$$\mathbf{Q} = \sum_{p=1}^{\infty} \mathbf{Q}_p, \tag{1.29}$$

$$\mathbf{D} = \mathbf{T}' + \mathbf{Q}\mathbf{E}(b') + \mathbf{Q}\mathbf{T}', \tag{1.30}$$

$$\mathbf{U} = \mathbf{R}''\mathbf{E}(b') + \mathbf{R}''\mathbf{D}, \tag{1.31}$$

$$\mathbf{R} = \mathbf{R}' + \mathbf{E}(b')\mathbf{U} + \mathbf{T}'^{*}\mathbf{U}, \tag{1.32}$$

$$\mathbf{T} = \mathbf{E}(b'')\mathbf{D} + \mathbf{T}''\mathbf{E}(b') + \mathbf{T}''\mathbf{D}, \tag{1.33}$$

where $E(b)$ is a diagonal $m \times n$ by $m \times n$ matrix in which each diagonal element represents an unscattered light at a specific scattering direction.

Using this technique to approximate the integrals in the RTE leads to have the results at separate and discrete directions corresponding to the quadrature points. One tactic to increase the accuracy of these numerical approaches is using more discrete points in zenith and azimuth angles in such a way that the number of points in ϕ direction should be approximately twice the number of points in θ direction. Also, by increasing the optical thickness, the number of n and m should be increased as well.

1.4.5 Coding and results

The adding and doubling method based on the above equations is written by MATLAB software to provide an accurate computation for reflection and transmission in plane parallel medium by considering the multiple scattering effect. This code also expanded to study radiation scattering fields of polarized light. There is no limitation on the value of medium thickness; however, by increasing the optical thickness more quadrature points should be applied in both zenith and azimuth directions to keep the same accuracy. This is due to the fact that using insufficient numbers of discrete points in a very thick medium induce an artificial absorption in the outputs. As a result run time increases by increasing the optical thickness. The number of division points can be obtained by trial and error.

The MATLAB code has been applied for various materials. Since this method is not restricted to Rayleigh scattering or non-absorbing media, this code can be used to compute

reflection and transmission for objects with wide range in albedo and size parameters with arbitrary polarized incident light. However, an increment in runtime has been observed for materials with large particles; this is due to the fact that Mie theory is used to compute the phase function.

The results are compared to the multiple sphere T matrix method ($MSTM$), an exact technique to calculate scattering properties. We will discuss this method in the next chapter. More details also can be found at [78, 80].

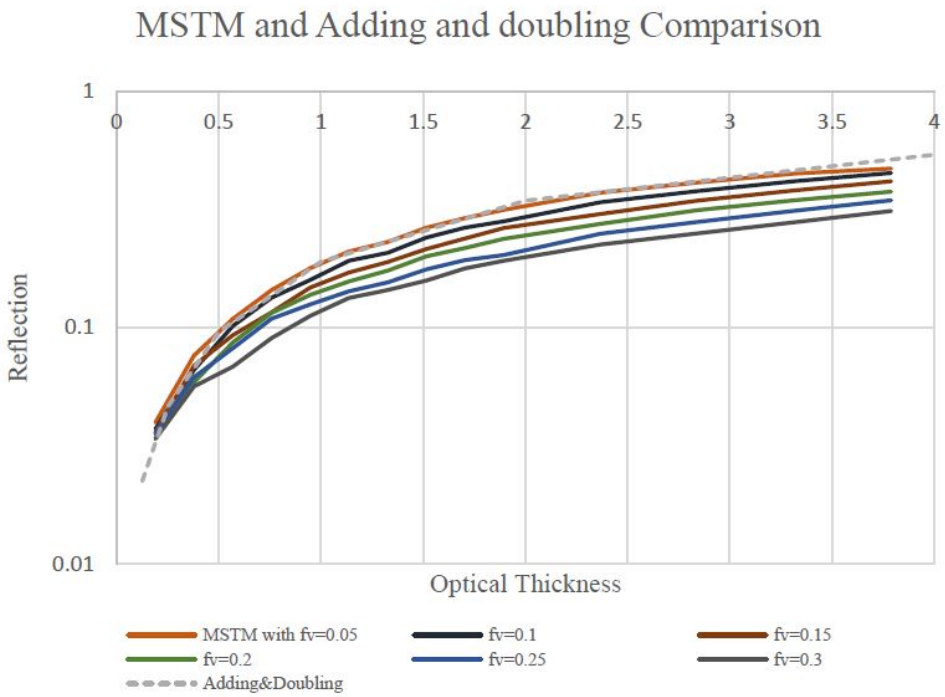

Figure 1.2: Reflection versus optical thickness of a TiO_2 slab

In Fig.2.2 directional-hemispherical reflection is plotted versus the optical thickness of a target composed of TiO2 spherical particles for different particle volume fraction values. The particle volume fraction is defined as the number of particles in a unit volume of the system and its dependency to the optical thickness of the system when particles are considered in

sphere can be shown by:

$$f_v = \frac{4a\tau}{3HQ_{ext}} \tag{1.34}$$

where a is the particle radius, Q_{ext} is the Mie extinction efficiency for the sphere, and H is the physical thickness of the target.

As one can see the results of the MSTM and adding and doubling methods converge when volume fraction of particles in the slab is smaller than five percent. However, when particle volume fraction exceed this number the RT theory overestimate the reflection from the film. This is due to the fact that theoretically the radiative transfer equation is valid only for media with small volume fractions; more details are discussed in the following section.

1.4.6 Dependent Scattering

We have seen in the last section that the RTE only applies to media with low packing densities. Derivation of the RTE from Maxwell's equations is dependent on limiting conditions regarding the scattering medium. One of these assumptions is that randomly positioned particles in the medium are widely separated from each other. Each particle is located in the far-field zone of the other particles. This implies that scattering properties of the individual particles in the target are independent of the existence of the other particles. The RTE/VRTE method includes the single scattering properties such as the extinction and phase matrices for the particulate medium rather than quantities effecting by the particle group. Also, in the RTE we assume that the observation point is in the far-field zone of the scattering medium. These assumptions explicitly indicate that in the RTE we should consider each particle as an independent scatterer in which near-field interference effects between scattered waves are ignored.

To understand interference effects between scatterers, consider a target with packed particles such that the scattering of each particle affects extinction by other particles. These

effects can be studied in two mechanisms. The first is near-field interparticle impact and describes the change of the net incident field on each particle by other particles. This effect modifies the amount of the absorption as well as scattering of each scatterer. The second mechanism is called far–field effect or coherent addition. The constructive and destructive interference of scattered radiation is considered in the far field effect. This affects the quantity and quality of scattering fields. We can therefore conclude that the RTE/VRTE is not valid for the case of large particle volume fractions and the assumptions of independent scattering fails for densely packed media. On the other hand, many industrial systems and technologies are utilize densely packed media, such as the packed fluidized bed, oil and gas fired furnaces, nuclear fuel rods, radiative burners, coal combustor, solid propellant rockets, chemical reactors, and paint layers. Thus it is necessary to have an exact and effective method that can predict the scattering properties of particulate media in various range of the particle packing density.

The modified radiative transfer equations in packed media has been studied analytically and experimentally by various researchers. All literature in this area is limited to either Rayleigh size (very small particles) or geometric size (very large particles). Several of these studies considered only the effect of the coherent addition while others examined the dependent scattering for Rayleigh scattering where only the far-field mechanism was studied [3, 8, 137, 58]. Also, Churchill and Clark [16] and, Chan and Tien [11] considered the same effect in geometric optic limits. Nimr and Arpaci [1] investigated the role of the near–field and far–field effects for two different pair distribution functions, impulse and linear models. However Kumer and Tien [68] considered both consequences of the dependent scattering in a scattering and absorbing medium for Rayleigh scattering with a limitation on the index of absorption such that spherical particles satisfy Rayleigh-Debye scattering. Y. Ma et al. [75] studied the influence of the multiple scattering on scattering and absorption in which the

radiative transfer equation was modified by effective propagation constant and effective reflective index. Extinction rate and phase function for dense media were calculated by Tsang and Kong [124, 125] based on the quasi-crystal approximation with coherent potential. Wen et al. [134] used these results to formulate propagation constant and albedo of coherent waves for small particles. Theoretical and experimental results were plotted for different volume fraction and they compared with the independent RTE too. In the geometric optic limit Kaviany[64] investigated the aspects of dependent scattering for materials with volume fraction larger than 0.006.

A regime map is shown in Figure 1.3, representing the boundary between dependent and independent scattering based on the different particle size and particle volume fraction. For the first time Hottel et al. [53] proposed that dependent scattering is not only a function of volume fraction but also c/λ (where c is the interparticle clearance and λ is wavelength), and suggested that dependent scattering effect can be considered where $c/\lambda > 0.3$. Later Tien [122] proved that the transition from dependent scattering to independent scattering happen when $c/\lambda = 0.5$. Figure 1.3 shows that this transition is not sharp and it has a smooth slope especially for particles in the same size as the wavelength.

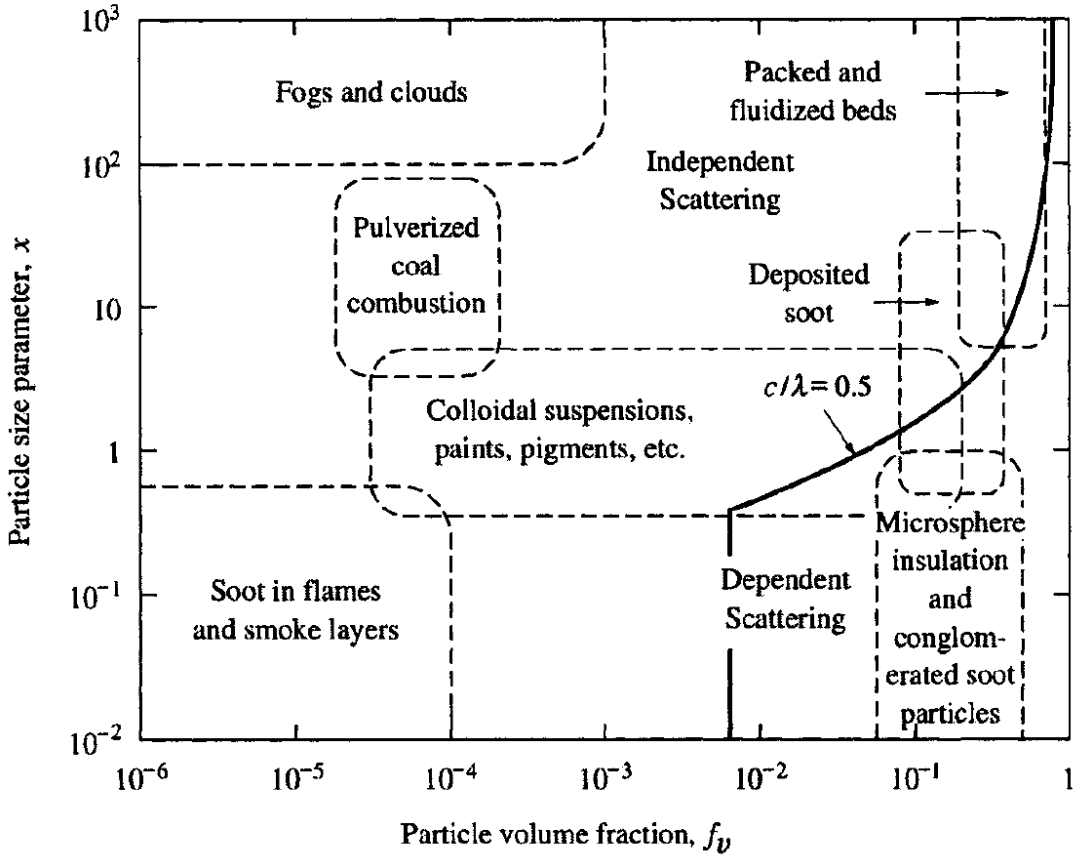

Figure 1.3: Independent and dependent scattering regime map (C. L. Tien, 1988 [122])

1.5 Numerical methods to solve Maxwell's wave equations

Maxwell's equations which are the fundamental equations of the classic electromagnetism lead to complex mathematical analysis and complicated numerical approaches. Analytical solutions are mostly available for simple geometries such as sphere and cylinder. We can argue that Mie theory (also called Lorenz-Mie theory), is the only analytical solution to Maxwell's wave equations (MWEs) for spherical geometry. However, this method and their related computational techniques have been evolved rapidly during past decades. Various numerical approaches have been developed and extended to directly simulate the electromagnetic (EM) wave scattering based on the exact solution to macroscopic MWEs. MWEs

in a source free domain considering time dependency of $exp(-i\omega t)$ for all fields are:

$$\begin{aligned} \nabla \times \mathbf{E} &= i\omega \mathbf{B}, \\ \nabla \times \mathbf{H} &= -i\omega \mathbf{D}, \\ \nabla . \mathbf{D} &= 0, \\ \nabla . \mathbf{B} &= 0 \end{aligned} \tag{1.35}$$

where $\mathbf{E}$ and $\mathbf{B}$ are electric field and magnetic induction which related to electric displacement $\mathbf{D}$ and magnetic field $\mathbf{H}$ by:

$$\begin{aligned} \mathbf{D} &= \varepsilon_0 \mathbf{E} + \mathbf{P}, \\ \mathbf{H} &= \frac{\mathbf{B}}{\mu_0} - \mathbf{M}, \end{aligned} \tag{1.36}$$

where $\mathbf{M}$ is the magnetization and $\mathbf{P}$ is electric dipole moment or electric polarization. In free space ε_0 and μ_0 are permittivity and permeability respectively.

A general solution to the MWE's provides a relationship between the incident field (source) and scattered fields and describes the scattered fields for an arbitrary object. Full–wave methods to the time–harmonic solutions of MWE's can be classifies to two techniques: Integral equation and partial differential equation. There are several methods that can be considered as an extension to the Mie theory such as the superposition strategy which used in the T–matrix method or Discrete dipole approximation (DDA).

1.5.1 Integral equation

Any solutions to the MWEs should satisfy the boundary conditions, i.e., the interface of two media. Integral equation methods are desirable techniques for solving Em problems. In electromagnetic integral equation methods is an important technique for the boundary value problems. Using this technique for inhomogeneous media will transform MWEs to an integral equation over the volume of the system. But if the method is applied to a homogeneous

scatterer, it will reduce the dimension of the problem to one due to the fact that the whole domain is reduced to only interface boundaries. So the integral equation method leads to considerable reduction on the degrees of freedom of the problem. There are two numerical integral equation methods including the surface integral equation (SIE) and volume integral equation (VIE). For the special case of the boundary conditions in the problem when sources and equations can be restricted to the boundary of the problem one can use the SIE. But if the conditions do not allow to use the SIE, the IVE can be applied based on the volume discretization of the target. The integral equation technique was first applied on the simple geometries involving two–dimensional problems such as long cylinder. Later, in 1965 it developed to three–dimensional problems. In 1993 Lakhtakia and Mulholland used method of moment and coupled dipole method to numerically solve the volume integral equations.

To solve MWEs using integral equation, we need to use the convolution concept by Fourier transform technique which leads to develop the Green's function method. One can use the Green's functions to derive the integral equations. In the VIE, the volume of the system is divided to two regions including a region which is occupied by the matter (V_int) and external part which is vacuous (V_extt). To discuss these numerical methods, we first present the MWEs for a homogeneous medium in response to the point source $\mathbf{J}(\mathbf{r})$:

$$\nabla \times \nabla \times \mathbf{E}(\mathbf{r}) - k^2 \mathbf{E}(\mathbf{r}) = i\omega\mu \mathbf{J}(\mathbf{r}) \tag{1.37}$$

where $k^2 = \omega^2 \mu\varepsilon$ is a constant (k is the wavenumber of the free space). The above equation can be rewritten for electric and magnetic fields in interior and external regions when there

is no external sources:

$$\begin{aligned} &\nabla \times \mathbf{E}(\mathbf{r}) - i\omega\mu_0 \mathbf{H}(\mathbf{r}) = 0 \\ &\qquad\qquad\qquad\qquad\qquad\qquad \text{for external volume} \\ &\nabla \times \mathbf{H}(\mathbf{r}) + i\omega\varepsilon_0 \mathbf{E}(\mathbf{r}) = 0 \end{aligned} \tag{1.38}$$

$$\nabla \times \mathbf{H}(\mathbf{r}) + i\omega\varepsilon_0 \mathbf{E}(\mathbf{r}) + i\omega\varepsilon_0[\varepsilon_1(r) - 1]E(\mathbf{r}) = 0 \quad \text{for internal volume} \tag{1.39}$$

where ε_1 is the permittivity of the matter. In above equation, we can consider the term $-i\omega\varepsilon_0(\varepsilon_1(r) - 1)\mathbf{E}(\mathbf{r})$ as the source or electric current density. It has been shown that [] the electric field $\mathbf{E}(\mathbf{r})$ is the solution of the volume integral equation:

$$\mathbf{E}(\mathbf{r}) = i\omega\mu \int_V \mathbf{J}(\mathbf{r}').\overline{\mathbf{G}}(\mathbf{r}', \mathbf{r}) d(\mathbf{r}') \tag{1.40}$$

where $\overline{\mathbf{G}}(\mathbf{r}', \mathbf{r})$ represents dyadic Green's function. Based on the (1.43), one can show that the Green's function is the solution to the following equation for a homogeneous medium.

$$\nabla \times \nabla \times \overline{\mathbf{G}}(\mathbf{r}, \mathbf{r}') - k^2 \overline{\mathbf{G}}(\mathbf{r}, \mathbf{r}') = \overline{I}\delta(\mathbf{r} - \mathbf{r}') \tag{1.41}$$

where $\mathbf{G}(\mathbf{r})$ the solution to the above equation can be represented as:

$$\overline{\mathbf{G}} = (\overline{I} + \frac{\nabla\nabla}{k^2}) \frac{e^{ik|\mathbf{r}-\mathbf{r}'|}}{4\pi|\mathbf{r} - \mathbf{r}'|} \tag{1.42}$$

1.5.2 Discrete Dipole Approximation

Introduction

the discrete dipole approximation (DDA) is a general technique to simulate scattering and absorption of electromagnetic radiation filed from objects with arbitrary shapes. This method is a popular and flexible tool in which target is considered as a continuum volume which is composed of small elementary subvolumes. In other words, the solid is approximated by a limited collection of polarizable points or dipole points that their distance from each other is small compared to the incident wavelength. Each dipole in the target interacts with both incident field and scattering fields from all other dipoles. Due to this interaction all dipoles become polarized and are said to have dipole moments.

The basic of this method was first introduced by DeVoe [22, 23] in 1964. However, the method applied only on molecular aggregates which their dimensions were small compared to the incident wavelength. The retardation effects also were not included in this technique. Later Purcell and Pennypacker [109] developed DDA method to study interstellar dust grains considering retardation effects. Discrete dipole approximation, which sometimes is referred to as couple dipole approximation, was further reviewed and expanded by Draine in 1988 [25] and later by Draine and Flatau in 1993 [26] who also developed the DDSCAT software. Several computer implementations of DDA technique have been written such as the DDSCAT, ADDA and ZDD; however, DDSCAT is the most popular one and is freely available based on the Fortran-90 language. The historical development and numerical aspects of the DDA was discussed by Yurkin and Hoekstra [138]. Also, Penttilä et al discussed various methods based on the DDA technique and compared the software and their accuracies.

The discrete dipole approximation technique is a flexible technique regarding the target geometry, particle size and shape. It has been applied to various geometries such as prisms,

rectangular, ellipsoids and cylinder. Also this method can be used in both inhomogeneous and anisotropic objects.

The method also is employed in periodic targets. The basic of this idea first introduced by Markel [85] for one dimensional dipoles and later it extended by Chaumet et al [13] in 2003. He studied the scattering of a plane wave by the two dimension parallelepipeds. Later Chaumet and Sentenac [14] developed the DDA for a double periodic structure with finite defects. Bruce and Flatau in 2008 [27] calculated the scattering amplitude matrix and Mueller matrix for targets with one and two dimensional periodic arrays.

Framework of the DDA method

In the DDA method the scatterer is divided to subvolumes that each of them represents a dipole with a polarizability tensor α. Assuming the dipoles are located at r_j for $j = 1, 2, , N$ (having N dipoles), so each dipole can be represented by its polarizability of α_j.

The dipole moment can be assigned as a scalar number or a diagonal tensor with equal elements $\alpha_{j,xx} = \alpha_{j,yy} = \alpha_{j,zz}$ for isotropic materials. If the target of interest is anisotropic, this tensor is not diagonal anymore; although, α is diagonalizable by choosing an appropriate coordinate system at a location of each dipole.

There are different methods and formulas to assign the best value to the dipole polarizabilities. The Clausius-Mossotti relation was used by Purcell and Pennypacker [109] to obtain α_j:

$$\alpha^0_{j,ll} = \frac{3}{4\pi n}\frac{\epsilon_{ll} - 1}{\epsilon_{ll} + 2}, \tag{1.43}$$

where ϵ_j is the dielectric function at r_j and n is the dipole density. This equation is exact at the limit $kd \to 0$ when there are infinite cubic lattices [62]. Many other methods were introduced by other researchers to calculate the dipole polarizabilities [25, 41, 59, 45, 30], but most of them failed at certain conditions. Drain and Goodman [28] considered the lattice

dispersion relation (LDR) in long wavelength limit $kd \ll 1$.

$$\begin{aligned}
\alpha^{LDR} \approx & \frac{\alpha^{CM}}{1+(\alpha^{CM}/d^3)[(b_1+m^2b_2+m^2b_3S)(kd)^2-(2/3)i(kd)^3]}, \\
& b_1 = -1.891531, \qquad b_2 = 0.1648469, \\
& b_3 = -1.7700004, \qquad S = \sum_{j=1}^{3}(\hat{a}_j\hat{e}_j)^2,
\end{aligned} \tag{1.44}$$

where a is a unit vector to describe the incident direction and e is another unit vector for polarization state. Comparing different results based on different dipole polarizability showed that LDR relation has the most accurate results when $|m|kd \lesssim 1$ [28, 26]. Therefore, one of the important criteria in DDA is having small lattice spacing (d) compared with the incident wavelength. Moreover, the number of dipoles (N) should be large enough so the target shape can be accurately represented by dipoles. So considering V and a_{eff} as the actual volume and effective radius of the target respectively, these conditions lead to

$$N > (4\pi/3)|m|^3(ka_{eff})^3, \tag{1.45}$$

After calculating the polarizability of dipoles, it is straightforward to obtain polarization at dipole locations:

$$\mathbf{P}_j = \alpha_j \mathbf{E}_j, \tag{1.46}$$

where E_j is the electric field at the location r_j. This electric field is a superposition of the incident field and all the other electric fields scattered by other $N-1$ dipoles. So E_j can be described by

$$\mathbf{E}_j = \mathbf{E}_{\mathrm{inc},j} - \sum_{k \neq j} \mathbf{A}_{jk}\mathbf{P}_k, \tag{1.47}$$

The contribution of all dipoles at position k that results in the electric field in position j is presented by $\mathbf{A}_{jk}\mathbf{P}_k$ including the retardation effect. Then the element of matrix A can be

computed by:

$$\mathbf{A}_{jk} = \frac{\exp(ikr_{jk})}{r_{jk}} \times \left[k^2(\hat{r}_{jk}\hat{r}_{jk} - \mathbf{1}_3) + \frac{ikr_{jk} - 1}{r_{jk}^2}(3\hat{r}_{jk}\hat{r}_{jk} - \mathbf{1}_3) \right], \quad j \neq k, \tag{1.48}$$

where $k = \omega/c$ and $r_{jk} = |r_j - r_k|$. Let A_{jj} defines as α_j^{-1}, so the scattering equation can be simplified to:

$$\sum_{k=1}^{N} \mathbf{A}_{jk}\mathbf{P}_k = \mathbf{E}_{\text{inc},j}, \tag{1.49}$$

Since A is a 3×3 matrix, equation (1.37) can be transferred to a system of equations with $3N$ equations and $3N$ unknown polarizations (P_j). Different numerical techniques can be used to solve this complex linear system of equations. Since N is a large number, direct method is practically impossible. however there are several iterative techniques that can be useful and efficient such as Complex conjugate Gradient (CCG) method [25], that is much faster than direct method. Flatau [34] compared different algorithms such as PBCGT and PETRKP. Also various methods are available in DDSCAT version 7.3 based on the different applications.

Once polarization is solved, the cross sections can be evaluated:

$$\mathbf{C}_{\text{ext}} = \frac{4\pi k}{|\mathbf{E}_0|^2} \sum_{j=1}^{N} \text{Im}(\mathbf{E}_{\text{inc},j}{}^* \cdot \mathbf{P}_j), \tag{1.50}$$

$$\mathbf{C}_{\text{abs}} = \frac{4\pi k}{|\mathbf{E}_0|^2} \sum_{j=1}^{N} \left\{ \text{Im}[\mathbf{P}_j \cdot (\alpha_j^{-1})^* \mathbf{P}_j^*] - \frac{2}{3}k^3 |\mathbf{P}_j|^2 \right\}, \tag{1.51}$$

Moreover the scattering cross section can be obtained by:

$$\mathbf{C}_{\text{sca}} = \mathbf{C}_{\text{ext}} - \mathbf{C}_{\text{abs}}, \tag{1.52}$$

To have an efficient computation strategy, fast Fourier transform (FFT) [113, 42, 35] was used for matrix-vector multiplication, as a result $O(NlogN)$ operations is required for this multiplication rather than $O(N^2)$ operations. Because number of dipoles (N) is a large value in discrete dipole approximation, using FFT can save a huge time and memory in coding.

Chapter 2

Radiative transfer equation and direct simulation prediction of reflection and absorption by particle deposits.

Abstract

Two methods for computing the normal incidence absorptance and hemispherical reflectance from plane parallel layers of wavelength–sized spherical particles are presented. The first method is based on an exact superposition solution to Maxwell's time harmonic wave equations for a system of randomly–positioned spherical particles excited by an incident plane wave. The second method is based upon the scalar radiative transport equation (RTE) applied to a plane parallel medium. Comparisons are made using five values of particle refractive index, sphere size parameters ranging from 1 to 4, and particle volume concentrations ranging from 0.05 to 0.4. The results indicate that the multiple sphere T matrix method (MSTM) and RTE predictions of hemispherical reflectance and absorptance converge when particle volume fraction becomes small. At higher volume fractions the RTE can yield results for hemispherical reflectance that, depending on the particle size and refractive index, significantly depart from the exact predictions. On the other hand, RTE and MSTM predictions of absorptance have a much closer agreement which is largely independent of the sphere optical properties and volume concentration.

2.1 Introduction

In recent years, remote sensing methods have been recognized as an important and valuable means to detect and identify the physical and chemical characteristics of particulate material deposited on natural or artificial surfaces. Obviously, the interpretation of remote sensing observations depends on an accurate prediction of scattering properties of bulk materials. In principle, such properties are fundamentally governed by the macroscopic Maxwell's wave equations (MWE)s, yet the microscopic–level complexity of particle deposits has, until recently, made direct solution of MWEs for deposits unfeasible. Because of this, effective medium theories and radiative transport models have traditionally been used to estimate the reflectance and absorption properties of deposits [4, 132, 130]. In effective medium theories, an inhomogeneous deposit is modeled as an effectively homogeneous layer characterized by an effective refractive index. This quantity can be obtained by an appropriate mixing rule as a function of particle concentration, pair correlation function, and single scattering properties. The coherent reflection and transmission by the layer can then be obtained by applying the Fresnel relations to the effectively homogeneous film [4, 132, 130].

The phenomenological scalar radiative transport (RT) theory treats the object as an absorbing and scattering medium, with an albedo, extinction coefficient, and scattering phase function obtained from the single scattering properties of the constituent particles. Reflection and absorption can be computed from an appropriate solution technique to the RT equation. A comprehensive examination of the relation of RT theory to the fundamental–level, Foldy–Lax description of multiple scattering has been presented recently by Mishchenko et al. [91]. Among the conditions inherent in RT theory are the assumptions that each particle lies in the far-field region of the other particles, and that the relative positions of the particles are uncorrelated. In closely-packed media these assumptions are not valid. However, there is

a growing progress to modify and apply the RT methodology to densely-packed particulate systems, via dense-media RT theories [52, 140, 102, 90].

In contrast to the techniques mentioned above, a superposition solution to the MWEs can provide, in principle, an exact method to calculate the reflectance and absorptance of particle deposits [80]. Such a method can be viewed as a direct simulation: the solution would be applied to a microscopically–detailed configuration of particles and would provide a detailed description of the scattered field resulting from plane wave incidence and the associated reflectance and absorptance of the configuration. Such methods are, by definition, computationally intensive, as the degrees of freedom in the solution will be directly proportional to the number of particles.

This work examines two methods to predict the radiative properties of plane-parallel layers of wavelength–sized spherical particles. The first method is the exact multiple sphere superposition method, coupled with high-performance computational strategies. We use the FORTRAN 90 implementation of this solution, the multiple sphere T Matrix (MSTM) code, to perform direct simulations of EM wave propagation in large-scale systems of spheres [82, 81]. This technique is used in order to study the effects of particle concentration on the spectral directional-hemispherical reflectance and directional absorptance [122] in dense media. The second method is the adding and doubling algorithm for solution of the scalar RTE applied to a plane parallel medium [20, 46], combined with Mie theory to compute the extinction coefficient, albedo, and scattering phase function of the spherical particles.

We begin this chapter by describing the mathematical formulation of the MSTM and RT techniques. In section 3, a comparison is made between these two methods for five values of particle material refractive index. The refractive index values include both large and small magnitudes of the real and imaginary parts, and are representative of highly refractive pigments and gold in the visible wavelengths and mineral matter in the visible and mid IR. The MSTM target models, in these computations, are comprised of randomly distributed

spherical particles with size parameters $x = \mathrm{k}a = 2\pi a/\lambda = 1, 1.5, 2$, and 4 where k, a and λ denote wavenumber, particle radius and radiation wavelength. Targets are generated with particle volume fractions varying from 0.05 to 0.4, and the dimensionless target thickness, $\mathrm{k}H$, ranges from a monolayer (i.e., $\mathrm{k}H_T \sim 2x$) to values on the order of 50-100.

As mentioned earlier, the framework of the RT theory is based on the mutual far–field and uncorrelated positions for the particles, and this approximation will fail in a densely packed medium. Therefore, an additional purpose of this work is to test the accuracy of the scalar RTE in predicting the absorption and hemispherically–integrated reflection for media with relatively large particle volume fractions. In addition, the MSTM method becomes impractical for deposits with large optical thickness. In this respect, by using the simulations to identify the errors between the exact and RTE results, as well as classifying these errors based on the sphere refractive index, size parameter, deposit volume fraction, and optical thickness, we hope to identify the conditions under which the fast and efficient RT procedure can be applied to particle deposits.

2.2 Computation methods

2.2.1 Multiple sphere T Matrix method

The MSTM method was used to calculate light scattering and absorption properties of targets consisting of spherical particles. This method implements the analytical solution to the time harmonic MWEs for a cluster of N_S spheres, with each sphere characterized by size parameter $x_i = \mathrm{k}\, a_i$, complex refractive index $m_i = m_i' + i m_i''$ and position vector $\mathbf{r}_i$, for $i = 1, 2, \ldots N_S$. At points external to the spheres, the vector electric field amplitude will be given as the superposition of the incident field and fields scattered from each sphere,

$$E_{ext} = E_{inc} + E_{sca} = E_{inc} + \sum_{i=1}^{N_S} E_{sca,i} \tag{2.1}$$

The incident and scattered fields are represented by expansions of regular and outgoing vector spherical wave functions (VSWFs) which are the vector eigenfunctions to the homogeneous vector Helmholtz equation,

$$E_{inc} = \sum_{n=1}^{L_S^i} \sum_{m=-n}^{n} \sum_{p=1}^{2} f_{mnp}^i N_{mnp}^{(1)}(r) \tag{2.2}$$

$$E_{sca,i} = \sum_{n=1}^{L_S^i} \sum_{m=-n}^{n} \sum_{p=1}^{2} a_{mnp}^i N_{mnp}^{(3)}(r - r_i) \tag{2.3}$$

in which $N_{mnp}^{(t)}$ denotes the regular ($t = 1$) and outgoing ($t = 3$) VSWF of azimuthal degree m, order n, and TM/TE mode p. In equations (2.2) and (2.3), f^i and a^i are known incident and unknown scattering coefficients, respectively. The objective of this method is to calculate the scattering coefficients for each sphere and to achieve this goal, continuity equations are applied at the surface of each particle in the cluster. To employ the boundary conditions at the surface of sphere i, the scattered fields from all the other particles are transformed, using the VSWF addition theorem, to a regular expansion centered about i. Mie theory is then used to relate the exciting and scattered fields for the sphere[79]. This leads to a system of equations for the scattering coefficients,

$$a_{mnp}^i + \bar{a}_{np}^i \sum_{\substack{j=1 \\ j \neq i}}^{N_s} \sum_{l=1}^{L_S^i} \sum_{k=-l}^{l} \sum_{q=1}^{2} H_{mnp\ klq}^{ij}\ a_{klq}^j = \bar{a}_{np}^i\ f_{mnp}^i \tag{2.4}$$

where $\bar{a}^i$ denotes the Mie scattering coefficient for sphere i, which depends on m_i and x_i. The outgoing VSWF translation matrix, H^{ij}, depends only on the dimensionless position of i relative to j. When the spheres in the cluster have the same truncation limit L_S, Eq. (2.4) represents a set of $2N_S L_S(L_S + 2)$ linear equations for the scattering coefficients.

Iterative methods are used to obtain a solution for a given incident plane wave direction and polarization.

The MSTM computations involved clusters (described below) containing on the order of $N_s \sim 10^3 - 10^4$ spheres. Even on parallel platforms, such large systems of spheres could require days of computational time to obtain a solution to Eq. (2.4); the main bottleneck being the N_s^2 scaling of the matrix-vector multiplication used to compute the exciting field at each sphere. To make the computations feasible a modification of the publicly–available MSTM code was employed. The modification used a discrete Fourier convolution, coupled with the Fast Fourier Transform (FFT) algorithm, to perform the translation operation in Eq. (2.4). The process involves three basic steps, being 1) translation of the sphere-centered outgoing expansions onto a new set of origins corresponding to a regular lattice, 2) mutual translation among the lattice origins using the FFT convolution, and 3) translation of the regular exciting field, centered about the lattice origins, to the original sphere origins. This procedure can decrease the computational time by up to a factor of 100. A paper detailing the procedure is currently in preparation.

Cylindrical targets, of radius R_T and thickness H_T were created by a simple Monte Carlo scheme which randomly filled the volume with N_S spheres of radius a; spheres were not allowed to overlap, and a sphere was considered inside the target when the sphere origin was inside the target volume. The volume fraction of the spheres was estimated as

$$f_v = \frac{4N_S a^3}{3R_T^2 H_T} \tag{2.5}$$

A configuration of spheres, corresponding to a volume fraction of 0.3, is shown in Fig. 2.1. To simulate plane-parallel conditions, the target radius R_T should be considerably larger than all other length scales present in the problem. For the sphere size parameters used in this investigation (1–4) and most of the volume fraction/target thickness combinations, target

radii of $kR_T \sim 40 - 60$ were sufficient to produce reflectance results that were invariant to increasing R_T.

For each solution for a target, the scattered power into the backwards hemisphere was obtained by numerical quadrature of the scattered intensity, obtained for two mutually orthogonal linear polarization states of the incident wave, over the hemisphere. The directional–hemispherical reflectance was then obtained by dividing the integrated power by the target cross section πR_T^2. Directional absorptance was calculated from the ratio of the total absorption cross section of the target to the target cross section. The simulation methodology does not allow a direct calculation of the directional–hemispherical transmittance of the target, due to the effect of diffraction by the finite–radius target on the forward scattered field. However, for highly absorbing, optically thick targets, for which the transmittance would be expected to be vanishingly small, the results would consistently yield reflectance + absorptance to within 2% of unity.

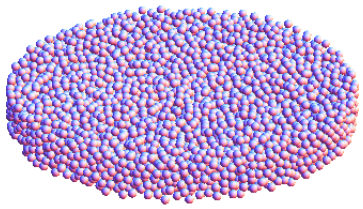

Figure 2.1: Spherical particle target sample used in MSTM computations.

A difficult situation to model was that corresponding to moderate to high optical thickness and small volume fraction. This could create a target with a dimensionless thickness on the order of $kH_T \sim 100$, and thus require a target radius that was, at least, two or three times this amount. For such conditions the standard (non-FFT based) solution strategy was used in MSTM; due to the relatively large spacings between the spheres in low f_v conditions the iterative solution converges very rapidly.

2.2.2 Radiative Transfer Theory

The adding and doubling method (AD) was used to generate numerical solutions to the scalar RTE for plane-parallel media [20, 55, 54]. The scalar (or phenomenological) RTE is an integro–differential equation for the specific spectral intensity, and provides an approximation to the specific intensity relative to that obtained from the vector RTE. For the case of directional–hemispherical reflectance and transmittance, the error in this approximation is expected to be on the order of a few percent [69]. Mie theory was used to calculate the extinction cross section, single-scattering albedo, and scattering phase functions of the particles. Adding–doubling is a recursive method, in which the bidirectional reflection and transmission matrices for a combined pair of layers are generated from the scattering properties of the individual layers. Initial values of the reflection and transmission matrices are obtained from the optically–thin limit of the RTE, for which the matrices become functions solely of the single scattering properties of the particles. The numerical computation is implemented by means of the Radau quadrature formula in the zenith direction and employing equally spaced points for azimuth dependency. The required number of quadrature points, for a specific set of sphere properties, was established empirically. The calculations were validated against the results of the vector radiative transport equation for the case of Rayleigh scattering [17]. In addition, the results for all sphere classes satisfied energy conservation to within a fraction of a percent.

2.3 Computational results

The MSTM calculations presented in this work were run on the Auburn University College of Engineering compute cluster, using 16 processors. Each MSTM data point corresponds to the average generated from 10 randomly–sampled configurations of the target. The amount of time required to generate a point could vary from 10 minutes to 3 days, depending on

the number of spheres in the configuration and the sphere size parameter and refractive index. The adding and doubling code was written in MATLAB language and run on a desktop computer. Given the scattering phase function, as calculated by standard Lorenz-Mie theory, the computational time to calculate reflection and transmission matrices over the presented range of optical thicknesses was typically around 2 hours.

Shown in Figs. 2.2–3.6 are predictions of hemispherical reflection versus optical depth as calculated by RT and MSTM procedures for refractive index of $m = 2.5$, 1.54, $1.9 + 0.03i$, $1.46 + 2.75i$, and $0.15 + 3.15i$. The first, second, and last values are typical of pigment materials (i.e., TiO_2), quartz/fused silica, and gold in the visible wavelengths, whereas the third and fourth can be associated with quartz at certain IR wavelengths. The plots (*a*, *b*, *c*, and *d*) within each figure correspond to a fixed value of size parameter and curves within each plot show the MSTM results for various volume fractions and the RT estimation. The incidence is normal for all calculations, and reflectance is plotted vs. optical thickness τ, which is defined by

$$\tau = \frac{3 f_v \, H_T \, Q_{ext}}{4 \, a} \tag{2.6}$$

where Q_{ext} is the Mie extinction efficiency for the sphere. For a fixed sphere size parameter and refractive index, the RT hemispherical reflectance is a function solely of τ, whereas the MSTM reflectance (for a sufficiently large target radius $\mathrm{k}R_T$) will depend on the individual values of $\mathrm{k}H_T$ and f_v. Note that all of the MSTM calculations in Figs. 2.2–3.6 do not extend to the maximum plotted optical thickness of 4; the limit in such cases represents the maximum computationally feasible result for the associated N_S and/or target volume.

Several observations can be made regarding the results in these figures. First of all, the predictions of the hemispherical reflection by the RTE and MSTM converge when the particle volume fraction in the medium is less than around five percent. However, at higher volume fractions the RT results can depart significantly from the exact simulations. Another

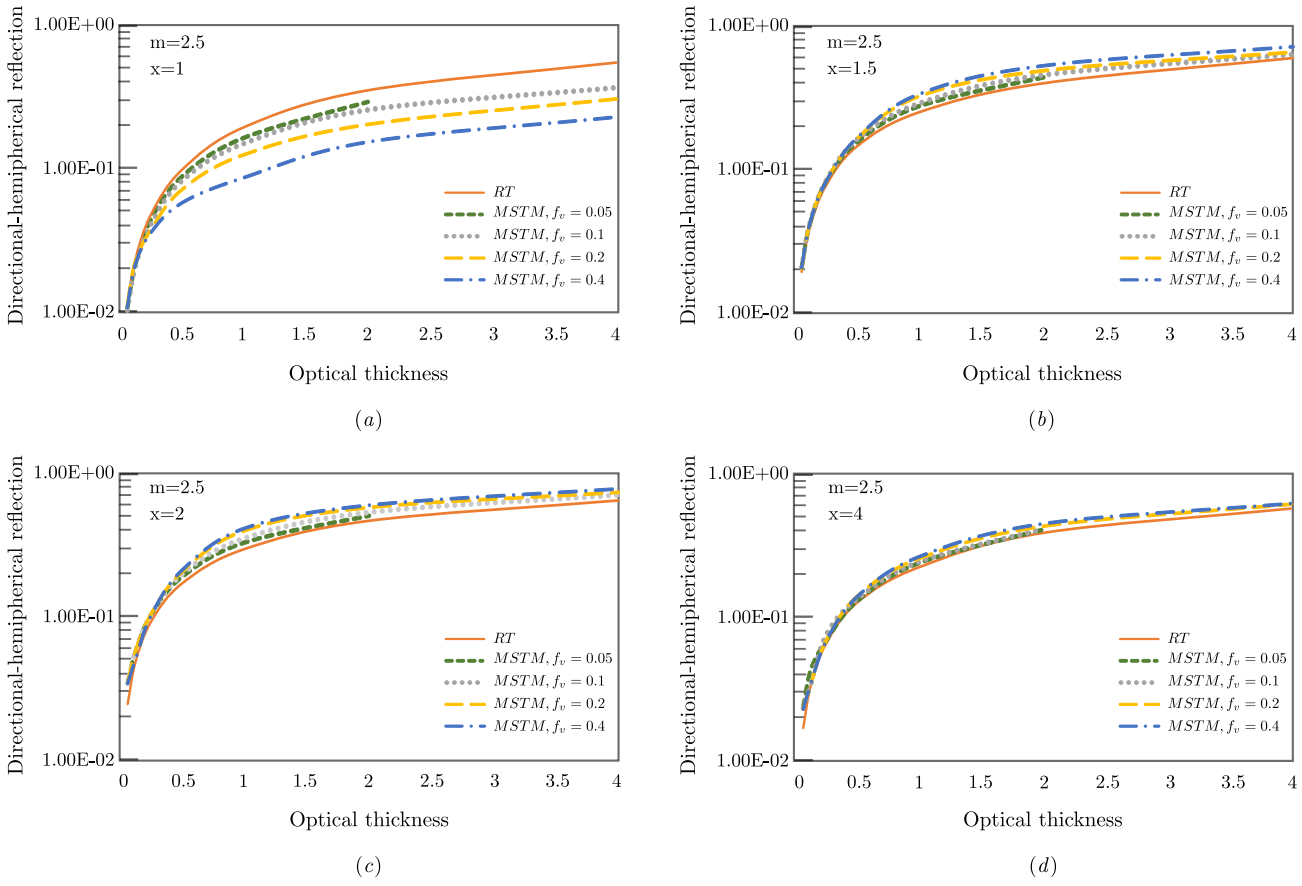

Figure 2.2: MSTM and RT computations for directional-hemispherical reflection from the modeled deposit with refractive index of $m = 2.5$ as a function of optical thickness.

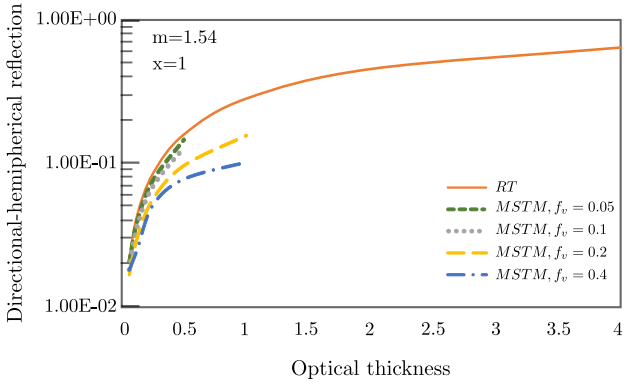

(a)

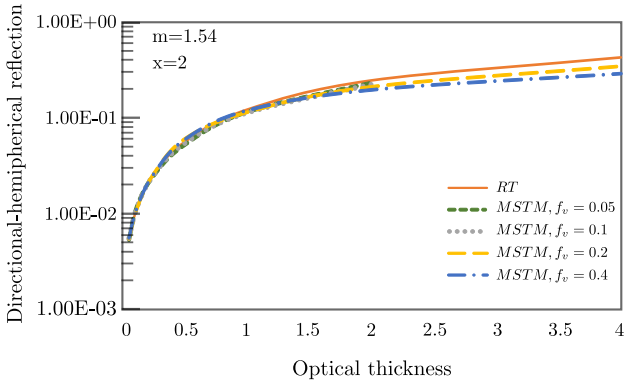

(b)

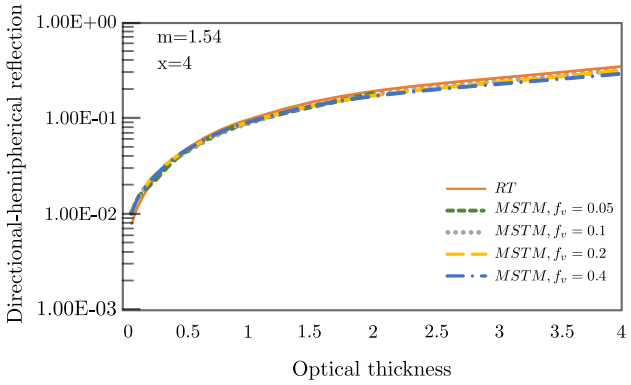

(c)

Figure 2.3: The same as in Fig. 2.2 except for the material with $m = 1.54$.

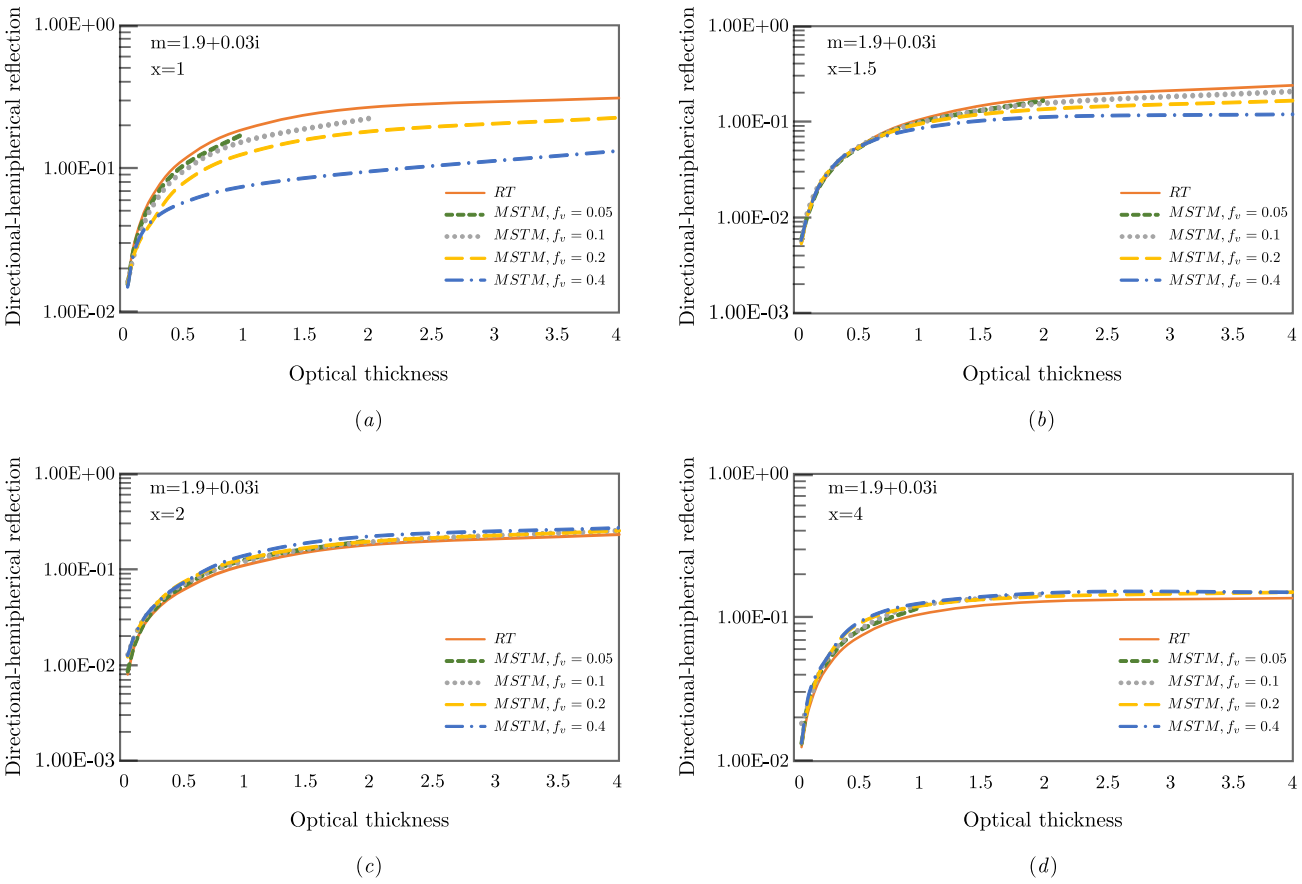

Figure 2.4: The same as in Fig. 2.2 except for the material with $m = 1.9 + 0.03i$.

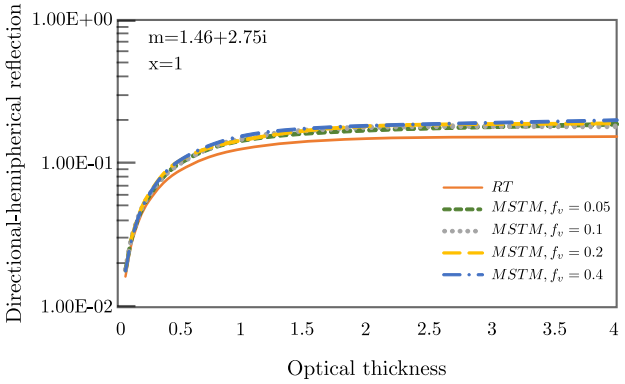

(a)

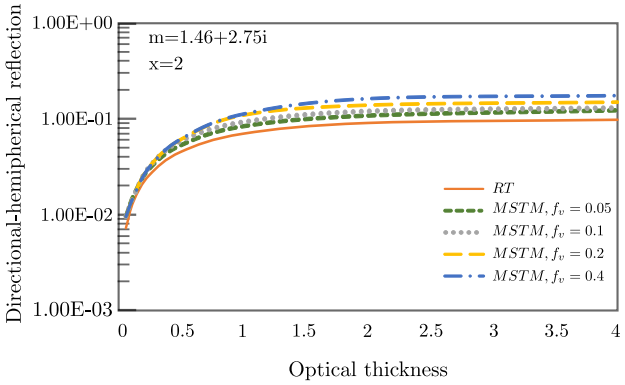

(b)

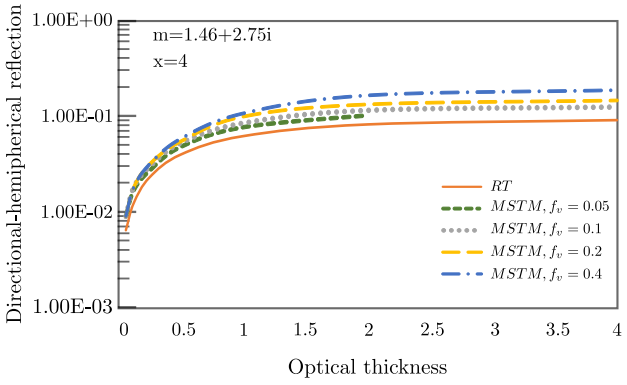

(c)

Figure 2.5: The same as in Fig. 2.2 except for the material with $m = 1.46 + 2.75i$.

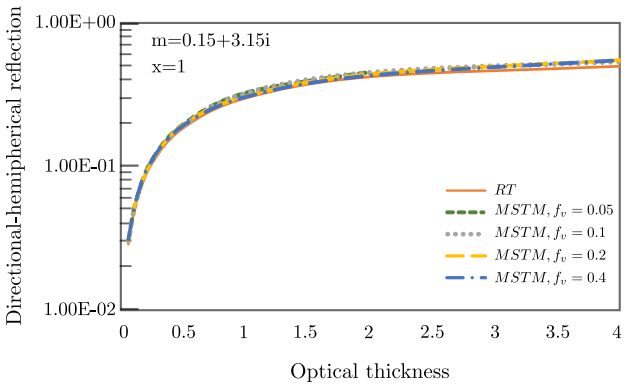

(a)

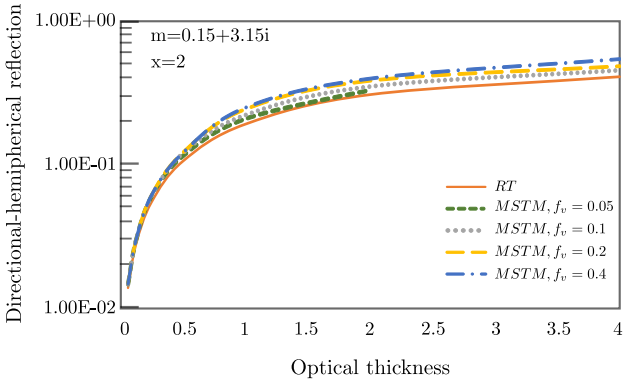

(b)

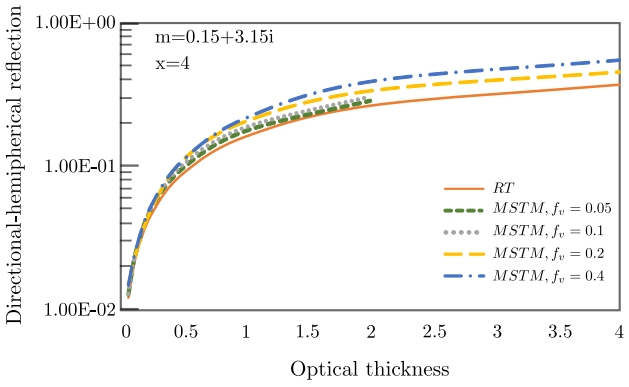

(c)

Figure 2.6: The same as in Fig. 2.2 except for the material with $m = 0.15 + 3.15i$.

important observation is that, for a set sphere size parameter and refractive index, the RT reflectance is either consistently larger or smaller than the MSTM reflectance for all examined volume fractions and optical thicknesses. In other words, as $f_v \to 0$, the MSTM results, for fixed sphere properties, monotonically approach the RT limit from either above or below. It is worth emphasizing that we were unable to associate the sign or magnitude of the MSTM-RTE difference with the single scattering efficiency, albedo, or asymmetry parameter of the sphere.

The presented results in the plots can be relevant for the interpretation of the reflection behavior of densely packed media based on the size parameters of particles. One can see from Figs. 2.2–3.4 that, for refractive indices with a small (or zero) imaginary part m'', the differences between RT and MSTM reflectance are greatest for the size parameter of unity and decrease as size parameter increases. However, the situation is reversed for refractive indices with a large imaginary part. As the results in Figs. 3.5 and 3.6 demonstrate, the greatest differences between the RT and MSTM reflectance now occur for a size parameter of 4. In particular, the RT/MSTM differences are nearly negligible for gold particles when $x = 1$, yet become appreciable at $x = 4$. An additional feature of the large m'' results is that an increase in f_v leads to an increase in reflectance for all particle size parameters. The situation for small or zero m'', on the other hand, is more complicated: different size parameters can lead to MSTM reflectance either larger or smaller than RT.

The effect of particle concentration on the normal absorptance of the deposit is examined in Figs. 3.7, 3.8, and 3.9, which correspond to refractive indices of $m = 1.9 + 0.03i$, $1.46 + 2.75i$, and $0.15 + 3.15i$, respectively. In stark contrast to reflectance, there are no significant differences in the MSTM and RT absorptances for the range of volume fractions and size parameters. To offer an interpretation of this behavior, we note again that the RT model is based on two key assumptions: the particles are in their mutual far field, and the particle positions are uncorrelated. This first assumption addresses the field exciting the individual

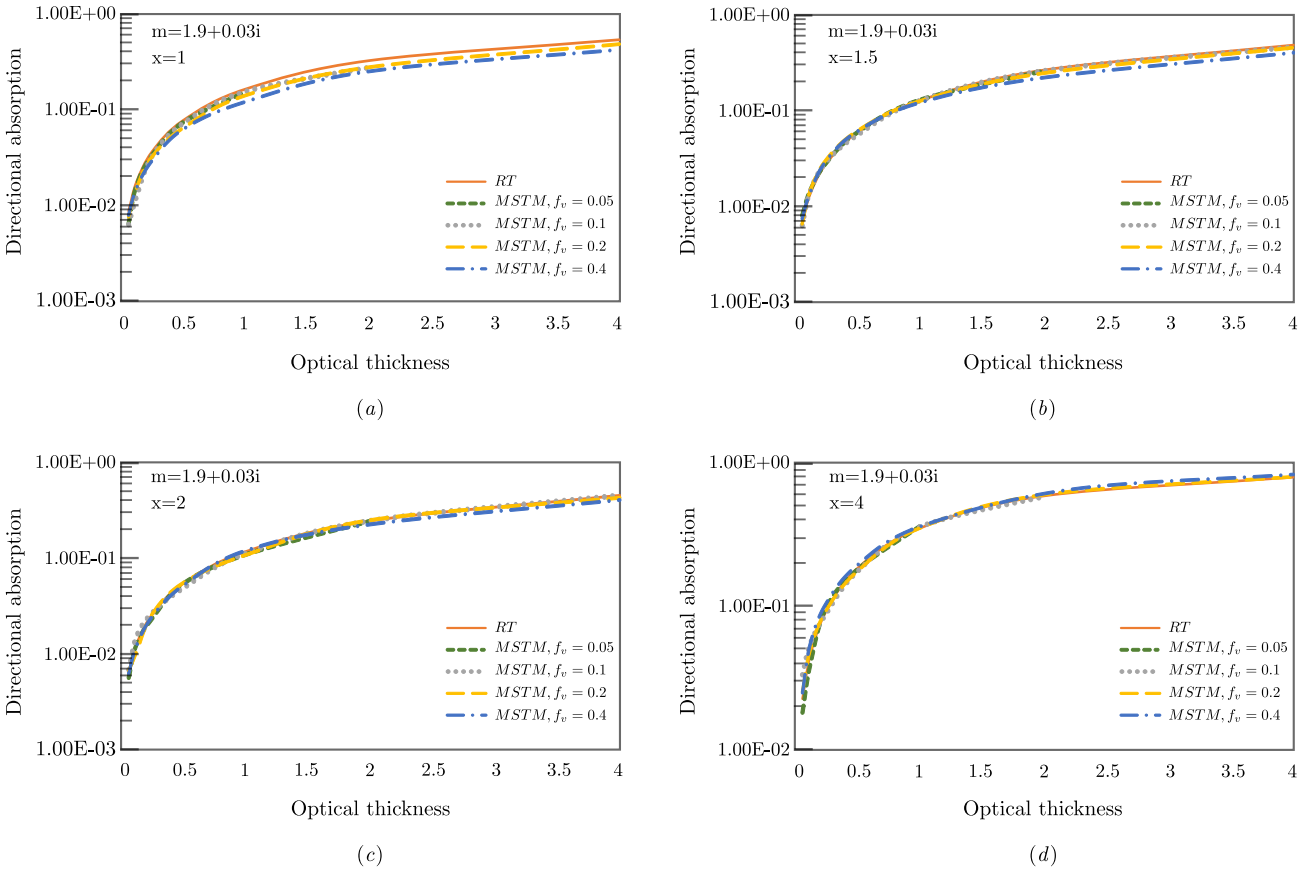

Figure 2.7: MSTM and RT computations for directional absorption from the modeled deposit with refractive index of $m = 1.9 + 0.03i$ as a function of optical thickness.

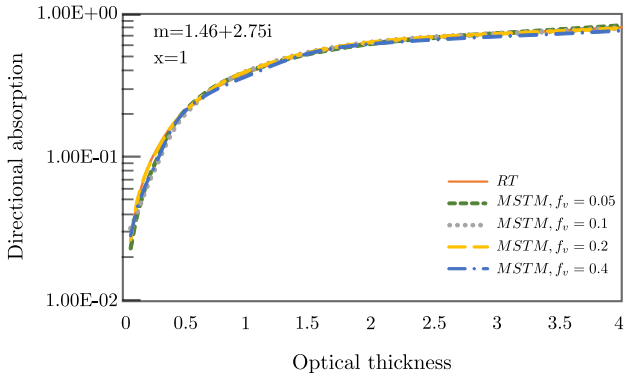

(a)

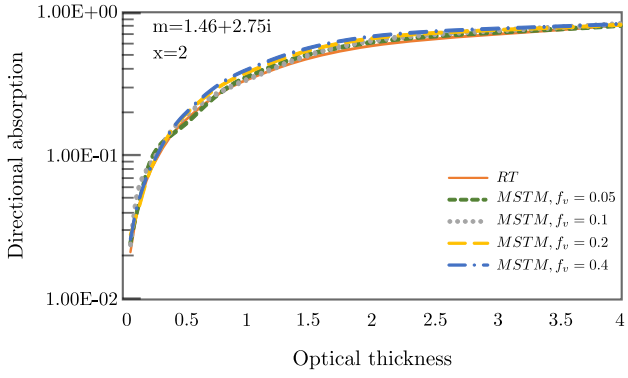

(b)

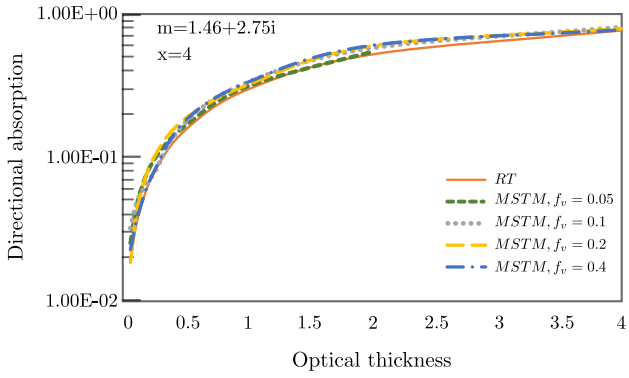

(c)

Figure 2.8: The same as in Fig. 3.7 except for the material with $m = 1.46 + 2.75i$.

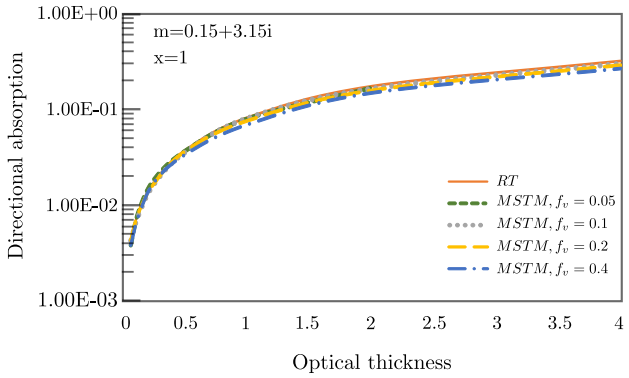

(a)

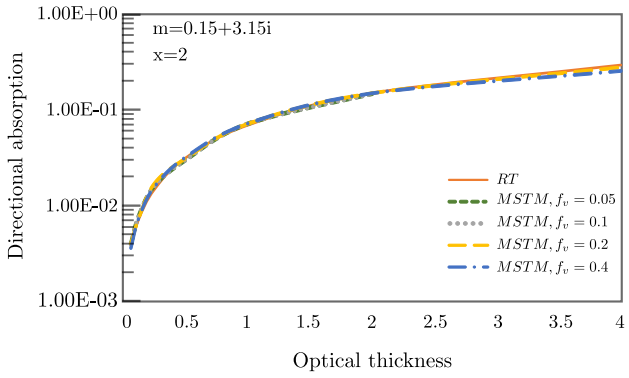

(b)

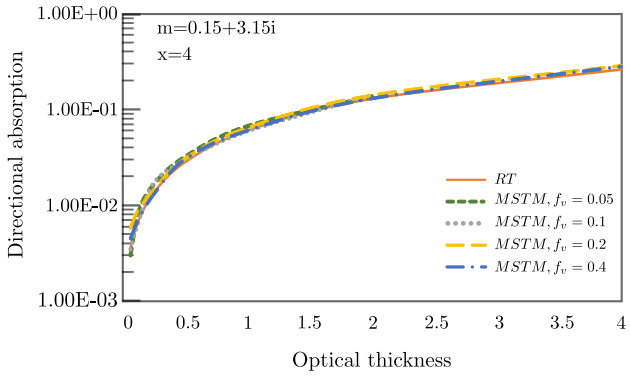

(c)

Figure 2.9: The same as in Fig. 3.7 except for the material with $m = 0.15 + 3.15i$.

particles, and whether or not it can be represented as a transverse wave. The second, on the other hand, relates to the far–field interference of waves scattered by separate particles, and whether or not such interference will contribute to the scattered power from the system. In this respect, differences between the RT and MSTM predictions of absorptance would be associated primarily with the first mechanism, i.e., near–field effects. Since no significant differences in absorptance are observed, we can conclude that — for the conditions examined here – the differences in RT and MSTM reflectance with increasing f_v are primarily the result of increasing correlation among the particles. This conclusion is consistent with recent observations by Mishchenko et al., in which an improved correspondence between vector RTE predictions and polarimetric measurements of bidirectional reflection from dense particle systems was obtained by using a modified phase matrix, which takes into account the particle pair correlation function as a function of particle volume fraction [92].

2.4 Conclusion

The main conclusion – being that the scalar, independent—scattering RTE cannot reliably predict the spectral hemispherical reflectance of densely packed systems of wavelength–sized particles – is not especially surprising given the fundamental assumptions inherent in the RTE. A more noteworthy conclusion is that the RTE predictions, when applied to such systems, can be either greater or smaller than the benchmark MSTM results. In this respect, the so–called mechanism of dependent scattering – which corresponds simply to conditions under which the RTE is not valid – can either enhance or attenuate reflection from the particle layer. Our limited calculations suggest that – as expected – the magnitude of this effect is dependent on the particle volume fraction, yet the direction of the effect (enhancement or attenuation) is an interdependent function of the particle size parameter and refractive index. In particular, we did not observe a correlation between the direction of the dependent scattering effect and a simple single–scattering property of the sphere.

An additional point we wish to make is that the MSTM–based direct simulation of reflection from particle deposits is entirely feasible on relatively modest (by today's standards) parallel computational platforms. As such platforms advance and become more accessible, we expect that direct simulation methodology will emerge as a practical means of calculating reflection and absorption by discretely inhomogeneous layers such as pigment films, regolith, powder coatings, and so on. The finite, 3-D target methodology used in this investigation has shortcomings when applied to optically thick conditions, as such conditions will require targets with large lateral width in order to model plane parallel conditions. We are currently exploring two approaches to extend the direct simulations to optically thick conditions. One approach is to use direct simulation to calculate the reflection and transmission matrices of a target that is optically thin yet contains sufficient particles to account for dependent scattering effects. The adding-doubling method can then be applied, using these matrices, to predict the reflection and transmission from media of arbitrarily larger thicknesses. The second approach is to reformulate the superposition solution to a plane layer by the use of periodic conditions. In addition, we are currently extending the computations to examine polarized bidirectional reflection from particle layers, and the results of these computations will be presented in a subsequent report.

Chapter 3

Direct prediction of bidirectional reflectance by dense particulate deposits.

Abstract

To observe and study the effects of the volume packing density on polarimetric scattering by deposited particulate materials, a comparison is made between the vector radiative transport equation (VRTE) and the plane wave plane parallel (PWPP) models for the polarized bidirectional reflectance and transmittance from plane parallel layers of randomly distributed, wavelength–sized particles. Calculations have been performed on ice and mineral materials with refractive indices of $\mathsf{m} = 1.31$ and $\mathsf{m} = 1.5 + 0.01\mathsf{i}$ respectively. In these simulations, particle volume fraction ranges from around 0.05 to 0.3 for deposits consisting of spherical particles with size parameters of one and two.

It is found that the PWPP model results converge to those predicted by the VRTE at small ($\sim$ 5% or less) particle volume fractions. At higher volume fractions, the difference between the PWPP and VRTE results depends strongly on the particle size and refractive index, yet not so much on the optical thickness (equivalently, volume of particles per unit area of layer).

PWPP simulation results of coherent backscattering effects – brightness opposition and polarization opposition effects – for ice and mineral particles are also represented. Their dependency on the particle volume fraction and particle size has been discussed.

3.1 Introduction

In recent work we examined the prediction of directional–hemispherical spectral reflectance by random deposits of wavelength–sized spherical particles, as performed by exact and by phenomenological methods [110]. The exact method in this work was the multiple sphere superposition solution to the time–harmonic Maxwell wave equations (MWEs), whereas the phenomenological method was the scalar radiative transport equation (RTE) applied to a plane parallel medium, with single–scattering albedo and scattering phase functions obtained from Mie theory.

Our results showed that RTE predictions of directional–hemispherical spectral reflectance became less accurate, relative to the exact method, as particle concentration approached densely packed conditions (i.e., particle volume fractions $f_v \sim 0.2 - 0.5$ for monodispersions). This was, of course, entirely expected, as it is assumed in the RTE that particles are in their mutual far–field radiation zones of each other [89]; for spheres with order–unity size parameters, such conditions are reached at f_v below around 0.02-0.05.

In this chapter, we extend this examination to the prediction of bidirectional, polarized spectral reflectance and transmittance from a plane parallel layer of spherical particles. Instead of the exact superposition solution, we employ the plane wave plane parallel (PWPP) model, derived in [77], to generate numerical solutions to the MWEs for the particle layer. The PWPP model represents the plane parallel, discretely inhomogeneous layer as a square, 2D periodic lattice of unit cells. The thickness of the cell spans that of the layer, and the cell width is chosen to be well larger than the characteristic correlation length of the particles. The cell contains a microscopically-detailed configuration of the particulate medium, which is generated using Monte Carlo methods, and the entire layer is excited by a linearly polarized plane wave of set incidence. The PWPP method directly calculates the directional distribution of reflected and transmitted electric field amplitude for the configuration, and average

(random media) properties are obtained by averaging over multiple, randomly–sampled cell configurations.

Simulation experiments are performed on two categories of particles, representing weakly-absorbing mineral matter and ice particles. The particles are taken to be spherical in shape, monodisperse, and can have size parameter of one and two. A range of particle volume fractions was applied to each set deposit. Based on the simulation results, we discuss under what conditions it is appropriate to use the classical VRTE method to simulate scattering properties by the deposit, and how the polarized radiation fields depend on the sphere size, refractive index, deposit volume fraction, and thickness. Such research is relevant to remote sensing applications, such as detecting and identifying particulate man–made or natural systems. Numerous investigations have been performed to understand the impact of the optical and physical characteristics of particulate materials on scattering properties [111, 67, 106, 105, 131, 141, 95] specially in the dense packed media [60, 74, 127, 98].

This chapter is organized as follows: the following section is a short summary of computational methodologies; i.e., the PWPP technique and the adding and doubling method that is used to solve the VRTE. Section 3 presents a comparison of scattering matrix elements predicted by these two techniques. Finally, a summary and conclusion are presented in the last section.

3.2 Theoretical background

3.2.1 Periodic Plane Parallel model

The key objective of the MWEs solver is to generate a solution for the scattered field produced by plane wave incidence on a microscopically–detailed configuration of an inhomogeneous plane parallel medium. Given this capability, the sought random–medium scattering

properties of the medium can be obtained by the appropriate averaging of the configuration–dependent properties over multiple randomly–sampled configurations. The degrees of freedom (DOF) in the plane-wave scattering solution method, when applied to a volume V containing an inhomogeneous medium, will generally scale with $\mathrm{k}_0^3 V$ where $\mathrm{k}_0 = 2\pi/\lambda_0$ is the free space wavenumber. Since the target, in this case, is laterally infinite, some approximation or idealization of the medium geometry is needed to produce a finite system of equations.

In our previous examination, we modeled the particle layer as a finite-volume cylindrical target having a radius significantly larger than all other characteristic lengths in the problem [110]. Random configurations of spheres were generated in the target volume, and the multiple sphere T matrix (MSTM) code was used to compute the scattered field produced by incidence along the z axis (i.e., normal incidence). The hemispherical reflectance was obtained by numerical integration of the scattered intensity over the backwards hemisphere and the normal absorptance was obtained from the total absorption cross section, both quantities divided by the target projected area. Hemispherical transmittance was obtained from these two properties via energy conservation. We demonstrated empirically that a sufficiently large target radius could be identified that resulted in radius–independence of the calculated hemispherical properties.

A limited set of calculations, using the MSTM code, also demonstrated that the finite-volume target model of a plane parallel medium suffered significant drawbacks when used to predict either bidirectional reflection or hemispherical reflection at non-normal incidence, in that increasingly oblique scattering or incidence angles required larger target radii to establish target–independent results. Furthermore, the direct calculation of transmission, either hemispherical or directional, is corrupted by the forward diffraction that is present in any scattering calculation of a finite–sized target.

For this (and other reasons), we adopted for this study a computational model that explicitly accounts for the infinite volume of the scattering medium. The approach used follows that developed by [27, 121] in which periodic conditions are imposed in the lateral plane. Specifically, the plane parallel layer is assembled from a 2D infinite periodic lattice of $W \times W \times H$ unit cells, where W is the cell width and H the thickness of the layer, with each unit cell containing a microscopically-specified and identical inhomogeneous distribution of material. As opposed the formulations in [27, 121, 76], in which a discrete dipole (DD) model was adapted to the 2D periodic lattice, an integral formulation and associated computer code specific to the periodic, plane parallel layer was derived and developed.

This formulation is described in detail in [77]; a brief synopsis will be given here. In what follows all lengths are made dimensionless by scaling with k_0, and the time harmonic factor is taken to be $e^{-\mathrm{i}\,\omega\,t}$. Within the layer the complex electric field amplitude will be governed by

$$(-\nabla \times \nabla \times + \epsilon(\boldsymbol{\rho}, z)\,)\;\mathbf{E}(\boldsymbol{\rho}, z) = 0 \tag{3.1}$$

in which $\boldsymbol{\rho} = \hat{\mathbf{x}}\, x + \hat{\mathbf{y}}\, y$ is the lateral position vector, z is the depth coordinate, and $\epsilon = \mathsf{m}^2$ is the position-dependent permittivity. The periodic conditions of the electric field amplitude in the lateral plane are identically satisfied by the expansion

$$\mathbf{E}(\boldsymbol{\rho}, z) = \sum_{\mathbf{s}} \mathbf{p}^{\mathbf{s}}(z)\, e^{\mathrm{i}\,\mathbf{k}_\rho^{\mathbf{s}} \cdot \boldsymbol{\rho}} \tag{3.2}$$

in which $\mathbf{k}_\rho^{\mathbf{s}}$ is the 2D reciprocal lattice (RL) vector given by

$$\mathbf{k}_\rho^{\mathbf{s}} = \mathbf{k}_\rho^0 + \frac{2\pi \mathbf{s}}{W}, \quad \mathbf{s} = s_x\, \hat{\mathbf{x}} + s_y \hat{\mathbf{y}}, \quad s_x,\ s_y = 0, \pm 1,\ \pm 2, \ldots \tag{3.3}$$

with $\mathbf{k}_\rho^0$ denoting the project of the incident propagation vector onto the lateral plane, and $\mathbf{p}^{\mathbf{s}}(z)$ is a vector amplitude function for the $\mathbf{s}$ RL mode. By utilizing the orthogonality

properties of the exponential functions when integrated over the lateral area of the unit cell, a system of vector ordinary differential equations (ODEs) in z can be obtained from Eq. (3.1) for each RL mode index $\mathbf{s}$. This system can be put in the form

$$\left(-\widetilde{\nabla}^{\mathbf{s}} \times \widetilde{\nabla}^{\mathbf{s}} \times +\overline{\epsilon}\right) \mathbf{p}^{\mathbf{s}}(z) = -\mathbf{a}^{\mathbf{s}}(z;\overline{\epsilon}) \tag{3.4}$$

where

$$\widetilde{\nabla}^{\mathbf{s}}\times = \begin{pmatrix} 0 & -d/dz & \mathsf{i}\,\mathrm{k}_y^{\mathbf{s}} \\ d/dz & 0 & -\mathsf{i}\,\mathrm{k}_x^{\mathbf{s}} \\ -\mathsf{i}\,\mathrm{k}_y^{\mathbf{s}} & \mathsf{i}\,\mathrm{k}_x^{\mathbf{s}} & 0 \end{pmatrix} \tag{3.5}$$

The source function $\mathbf{a}^{\mathbf{s}}(z;\overline{\epsilon})$ – which is equivalent to a displacement field – is defined by

$$\begin{aligned} \mathbf{a}^{\mathbf{s}}(z;\overline{\epsilon}) &= \sum_{\mathbf{s}'} \left(\epsilon^{\mathbf{s}-\mathbf{s}'}(z) - \overline{\epsilon}\,\delta_{\mathbf{s}-\mathbf{s}'}\right) \mathbf{p}^{\mathbf{s}'}(z) \\ &= \sum_{\mathbf{s}'} \hat{\epsilon}^{\mathbf{s}-\mathbf{s}'}(z;\overline{\epsilon})\,\mathbf{p}^{\mathbf{s}'}(z) \end{aligned} \tag{3.6}$$

with $\delta_{\mathbf{s}-\mathbf{s}'}$ denotes the Kronecker delta function, and $\epsilon^{\mathbf{s}}(z)$ denotes the lateral finite Fourier integral transform of the permittivity distribution in the unit cell:

$$\epsilon^{\mathbf{s}}(z) = \frac{1}{W^2} \int_{-W/2}^{W/2} dx \int_{-W/2}^{W/2} dy\, e^{-\mathsf{i}\,\mathbf{k}_\rho^{\mathbf{s}}\cdot\boldsymbol{\rho}}\, \epsilon(\boldsymbol{\rho}, z) \tag{3.7}$$

The complex–valued parameter $\overline{\epsilon}$ can be viewed as a reference (or effective) permittivity of the medium: it has no effect on the amplitude function $\mathbf{p}^{\mathbf{s}}(z)$ for a given spatial distribution of permittivity and a given incidence – which can be seen by combining Eqs. (3.6) and (3.4) – yet it will have a substantial effect on the numerical effort required to obtain a solution. It is implicitly assumed that the summation over the x and y RL indices in Eqs. (3.2) and

(3.6) can be truncated at some appropriate maximum index s_{max}, which would result in $(2\,s_{max}+1)^2$ vector ODEs in all.

A 1D dyadic Green's function (DGF) can be derived for the ODE of Eq. (3.4). Unlike the free space DGF used in traditional DD methods, the DGF employed here explicitly accounts for the boundaries of the slab at $z = 0$ and H. Specifically, the DGF gives the $\mathbf{s}$-mode field at point z resulting from a source at point z', with both z and z' residing within a slab of thickness H and uniform permittivity $\overline{\epsilon}$ that is backed on both sides by a medium of unit permittivity. A 1D integral solution to Eq. (3.4) can be constructed from the DGF via

$$\mathbf{p}^{\mathbf{s}}(z) = \Phi^0(z;\overline{\epsilon})\,\delta_{\mathbf{s}} + \int_0^H \mathbf{G}^{\mathbf{s}}(z,z';\overline{\epsilon})\cdot\mathbf{a}^{\mathbf{s}}(z';\overline{\epsilon})\,dz', \quad 0<z<H \tag{3.8}$$

where $\Phi^0(z;\overline{\epsilon})$ is the complex vector amplitude existing in the homogeneous reference slab, of permittivity $\overline{\epsilon}$, when excited by the incident wave, and $\mathbf{G}^{\mathbf{s}}(z,z';\overline{\epsilon})$ is the DGF for the slab.

An integral equation for the source function $\mathbf{a}^{\mathbf{s}}(z;\overline{\epsilon})$ is obtained from the discrete convolution of Eq. (3.8) with the transformed permittivity, per Eq. (3.6). This equation is discretized by dividing the layer thickness into N_H elements, each of thickness $d_H = H/N_H$, and within which the source function is assumed constant. Likewise, the transformed permittivity in Eq. (3.7) is calculated, at each layer element, by dividing the lateral area into N_W^2 square elements each of width $d_W = W/N_W$, assigning a uniform permittivity to the element based upon the material distribution within the element, and approximating the Fourier integrals with a discrete Fourier transform; this operation can be performed with a FFT. The working system of equations so derived appear as

$$\mathbf{a}^{\mathbf{s},j} - \sum_{\mathbf{s}'}\hat{\epsilon}^{\mathbf{s}-\mathbf{s}',j}\sum_{j=1}^{N_H}\mathbf{G}^{\mathbf{s}',j,j'}\cdot\mathbf{a}^{\mathbf{s}',j'} = \hat{\epsilon}^{\mathbf{s},j}\,\Phi^{0,j} \tag{3.9}$$

where superscript j denotes the depth coordinate. The application of the DFT to calculation of the permittivity spectrum constrains the largest RL mode index to $s_{max} = N_W/2$, and the

associated maximum wavevector magnitude to $\mathrm{k}_{max} = \pi/d_W$. In the calculations performed here a significantly smaller range of RL modes will be retained; this is discussed further at the end of this section.

The scattered far-field from the periodic layer takes the form of a diffraction pattern, i.e., a discrete superposition of transverse plane waves with propagation direction vectors $\mathbf{k^s}$ given by

$$\mathbf{k^s} = \mathbf{k}_\rho^\mathbf{s} + \sigma\, \mathrm{k}_z^\mathbf{s} \tag{3.10}$$

$$\mathrm{k}_z = \left(1 - \left|\mathbf{k}_\rho^\mathbf{s}\right|^2\right)^{1/2} \tag{3.11}$$

with $\sigma = \pm 1$ denoting whether the wave is propagating upwards (transmission) or downwards (reflection). The complex amplitude of the $\mathbf{s}$ mode reflected or transmitted wave will be a function solely of the corresponding $\mathbf{s}$ mode source coefficients. Only the propagating RL modes, corresponding to $\left|\mathbf{k}_\rho^\mathbf{s}\right| < 1$, will appear in the far-field reflection and transmission, yet the evanescent modes ($\left|\mathbf{k}_\rho^\mathbf{s}\right| > 1$) will contribute to the coupling of EM energy between lattice planes (per Eq. (3.9)) and as such will indirectly affect the far-field scattering. The polar angle increment between diffraction peaks is $\sin\Delta\theta = 2\pi/W$, or $\Delta\theta \sim 2\pi/W$ for $2\pi/W \ll 1$, and in this respect a criterion for the unit cell width W is that it be sufficiently large to provide a sufficiently fine RL mesh to resolve the directional features of reflection and transmission.

The discretized numerical model in Eq. (3.9) contains $3N_W^2 N_H$ degrees of freedom (DOF), with the 3 accounting for the $3D$ vector nature of the source function. A limited set of calculations presented in [77] indicated that – under random media conditions – the number of RL modes could be truncated to a value $N_R^2 \ll N_W^2$ with negligible effect on the calculated hemispherical reflectance and transmittance properties of the layer [76]. A convenient parameter for indicating the cutoff point is the wavenumber k_R, defined so that

$N_R = W\mathrm{k}_R/\pi = N_W d\mathrm{k}_R/\pi$. Setting $\mathrm{k}_R = 1$ would include primarily the propagating modes in the calculation, and $\mathrm{k}_R = \pi/d$ would include all N_W^2 modes. Implementing this strategy is basically equivalent to performing a spectral windowing (or filtering) operation on the permittivity distribution in direct space. That is, the convolution over index $\mathbf{s}'$ in Eq. (3.9) would be performed by the ubiquitous FFT procedure, and doing so requires storage of the permittivity distribution at $4N_R^2$ spatial points. This distribution is obtained by first generating permittivity distributions in the W^2H unit cell, which are then FFT'd, square windowed, and inverse FFT'd back to the spatial domain. The advantage of the method is that it retains the benefits of the large W – in that it can be chosen to provide a sufficiently small angular resolution – while reducing the size of the system of equations to a tractable level.

A simple Monte Carlo algorithm is used to produce random configurations of spheres in the unit cell. The algorithm places N_S spheres in the cell subject to the constraint that the spheres do not overlap, and no part of the sphere extends beyond the boundaries at $z = 0$ and H. Periodic conditions are identically imposed on the lateral boundaries: a part of a sphere extending beyond one boundary will be placed on the inside surface of the opposite boundary. This procedure is contrived in that it does not attempt to explicitly model the physical mechanisms of particle deposit formation, yet it does create an inhomogeneous medium comprised of impenetrable monodisperse spheres that, statistically, have a uniform volume concentration. This medium is not claimed to be realistically representative of natural particulate media, yet it does provide a controlled condition to which the computational models (PWPP, VRTE) can be applied. The particle volume fraction reported in the calculation results represents the average within the cell, i.e., $f_V = 4\pi N_S\, a_S^2/3W^2H$.

A Fortran-90+MPI code was developed to generate solutions to Eq. (3.9). For a given unit cell configuration and incident direction, calculation of the 2×2 complex amplitude matrix and the 4×4 Stokes matrix, for reflection and transmission and at each propagating

RL mode, require a pair of solutions to Eq. (3.9) for two mutually orthogonal incident polarizations. The linear system in Eq. (3.9) is solved iteratively using the biconjugate gradient algorithm, and the convergence rate of this algorithm is strongly affected by the choice of the reference permittivity $\bar{\epsilon}$. In [77] it was shown that the optimum $\bar{\epsilon}$ corresponds to the effective permittivity of the medium, which describes the propagation and attenuation of the coherent field. In the present work we use a heuristic scheme to assign a value to $\bar{\epsilon}$, in which

$$\overline{\mathsf{m}} = \sqrt{\bar{\epsilon}} = \mathsf{m}_V + \mathsf{i}\,\frac{\kappa}{2} \tag{3.12}$$

where m_V is the volume-averaged complex refractive index of the unit cell, and κ is the dimensionless radiative transfer extinction coefficient calculated from

$$\kappa = \frac{3Q_{ext}\, f_V}{4a_S} \tag{3.13}$$

with Q_{ext} the Mie extinction efficiency for the sphere of dimensionless radius a and refractive index m_S and f_V is the particle volume fraction in the cell.

Calculation of observable polarized bidirectional reflection and transmission, for random media, require configuration averages of the amplitude and Stokes matrices at the propagating RL directions. The coherent reflection and transmission elements of the layer correspond to those calculated from the configuration–averaged reflected and transmitted amplitudes, and the diffuse reflection and transmission elements are obtained by subtracting the coherent properties from the configuration–averaged values. In our simulations the particle positions between any two configurations are completely uncorrelated, and for this case the coherent reflection and transmission will theoretically average to zero for all directions except $\mathbf{s} = (0, 0)$, i.e., specular reflection and line-of-sight transmission. This condition is automatically imposed in the calculations, so that diffuse reflection/transmission, at any direction except $\mathbf{s} = 0$, is simply the averaged reflected/transmitted matrix elements.

In the present investigation the incident direction is taken to be normal: this results in a computational advantage as well as a computational problem. The advantage is that for normal incidence the incident plane – which is used to define the parallel and perpendicular components of the incident polarization – can be analytically rotated to coincide with the scattering plane for each RL direction. This allows the reflection and transmission matrix elements, computed for each configuration, to be numerically averaged over azimuthal angle, and considerably reduces the number of configurations needed to produce steady averages.

The disadvantage of normal incidence is that it makes problematic the computational identification of coherent backscattering effects. It's name notwithstanding, coherent backscattering would be classified as a diffuse effect in the present investigation: it is a feature of scattering by a discretely random inhomogeneous medium for a specific configuration (which is present because the particles are impenetrable and have finite size), whereas coherent reflection, as defined here, is due entirely to the fact that the layer boundaries are fixed from one configuration to another. The angular width of the coherent backscattering peak will be also be proportional to the particle number density, whereas the coherent reflection peak (a.k.a., the specular peak) would appear as a delta function (i.e., zero angular width) for the idealized model.

For normal incidence the specular reflection direction (the reflection of the incident direction in the $x - y$ plane) coincides with the backscattering direction (the reverse of the incident direction). Both the averaged reflection matrix elements, and those computed from the averaged amplitude, will be relatively large at the specular reflection direction, and because of this the calculation of the diffuse component can suffer from numerical loss–of–precision errors. In addition, the coherent reflection can exhibit interference behavior with changing H, which is an artifact of the idealized, perfectly–flat geometrical model of the layer [104]. In principle this effect should be absent in the diffuse reflection component at $\mathbf{s} = 0$, yet our calculations results indicate that some physically anomalous behavior

can be present (e.g., "negative" coherent backscattering) especially for relatively small layer thicknesses. We should mention that the perfectly flat boundary of the layers is artificial and not representative of natural particle deposits or layers. The Monte Carlo procedure used to generate the configurations results in a 'surface roughness' length scale comparable with the particle radius; in natural conditions the roughness length would be expected to be considerably larger. The simple model has been chose primarily so that the condition for the particle volume fraction going from zero to some uniform set value over a distance of a particle diameter can be tested. This allows for a less ambiguous comparison with VRTE calculations in that, for the latter, we can take the scattering medium properties to be uniform.

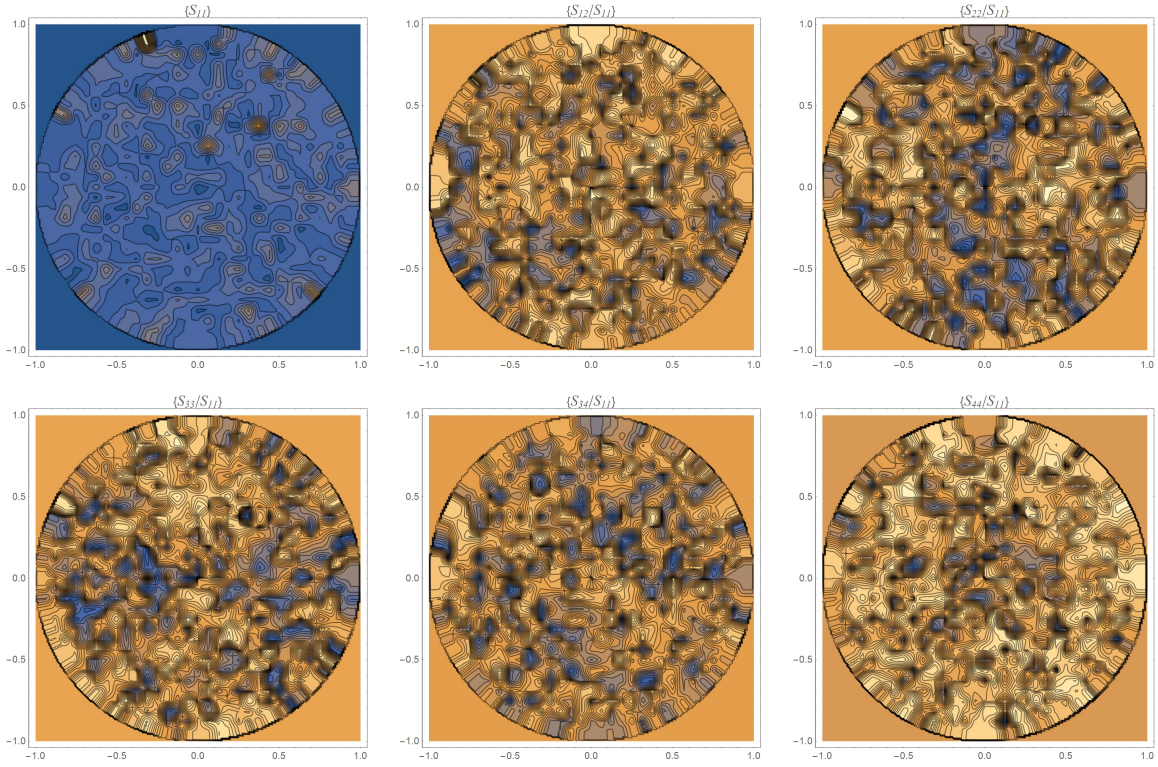

Figure 3.1: Two dimensional plots of scattering matrix elements for light reflected by ice deposit. The thickness of the deposit is 20 and ice particles have the nondenominational radius of two. This plots depicts the normalized diffuse reflection for one configuration of random positioned ice particles.

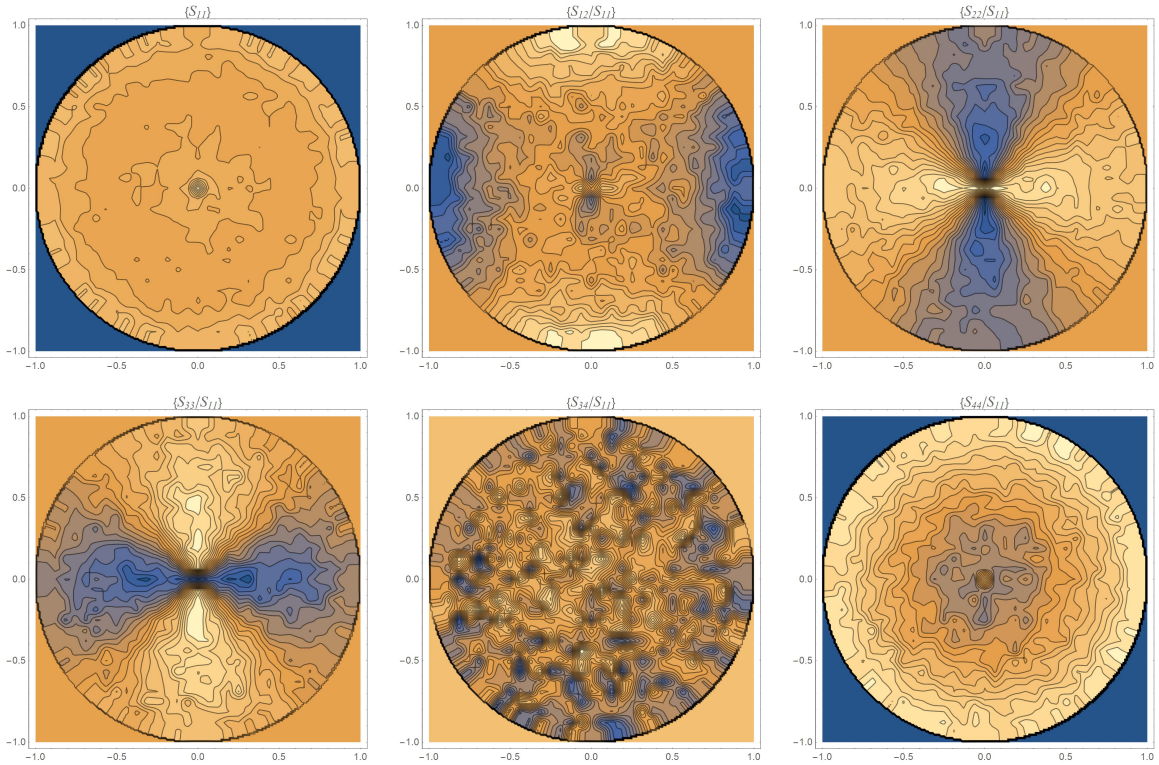

Figure 3.2: The same as in Fig.4.1, except that it was averaged out over 500 configurations of random positioned ice particles.

An indication of the need for configuration averaging is illustrated in Figs. 1 and 2. Figure 1 shows the directional distribution of reflection matrix elements calculated for a single configuration, in this case a deposit of unit size parameter ice spheres ($m = 1.31$) with a volume fraction of 0.2 and dimensionless thickness 20. The horizontal and vertical axes correspond to $\sin\theta\cos\phi$ and $\sin\theta\sin\phi$, with θ and ϕ denoting the polar and azimuth angles. Incidence is normal, and the matrix elements are defined with the incident plane corresponding to the $\hat{x}-\hat{z}$ plane. The actual inhomogeneity of the configuration produces the characteristic speckle pattern seen in Fig. 1. Figure 2 shows the distributions averaged over 500 randomly sampled configuration. As can be seen, averaging extinguishes the speckle pattern, and results in the emergence of the macroscopic reflection characteristics of the layer.

3.2.2 Radiative Transfer Theory

The adding-doubling (AD) method for targets in parallel plane geometry provides one of the most accurate solutions to the radiative transfer equation. The method was introduced by Van de Hulst [128] and developed by Haan [20] to solve the VRTE which fully accounts for polarization effects. The target is considered as a pile of thin sublayers in the sense that each layer can be assumed as a homogeneous medium, so the optical properties do not vary along the optical thickness. The essence of the technique is based on the successive scattering back and forth between the slab layers. The method assumes the knowledge of the reflection, transmission, and absorption for a single thin layer. In this study, the first layer is thin enough so one can neglect the multiple scattering effects. Therefore, its optical properties can be represented by single scattering properties of the medium (i.e., phase function, albedo, extinction efficiency). One can then calculate the reflection and transmission by doubling the first thickness and repeat the process until the desired thickness is reached. It is important to note that integrations over the polar scattering directions were solved numerically using the

Radau quadrature approximation. Numerical integration over azimuthal angle was handled by means of equal distance points between $\theta_{scat} = 0°$ and $\theta_{scat} = 360°$, such that the number of points in the azimuth direction was at least two times the total quadrature points.

In these simulations, the first layer has an optical thickness $\tau = 2^{-30}$. The phase function and albedo were evaluated using the classical Lorenz–Mie theory. The number of quadrature points was between 30 and 40 and azimuthal angles of 60 to 80 points depending on the optical thickness. The adding-doubling VRTE code was written in the MATLAB and performed on a workstation computer.

3.3 Comparison of VRTE and PWPP for bidirectional reflectance and transmittance

The comparison of VRTE and PWPP models are presented in this section. We calculated the reflection and transmission matrices, for normal incidence, of particulate materials consisting of ice, with $\mathsf{m} = 1.31$, and weakly-absorbing mineral matter with $\mathsf{m} = 1.5 + 0.01\mathsf{i}$. The particles were modeled as monodisperse spheres with dimensionless radii of $a = 1$ and 2. The calculations are conducted using values of particle volume fractions of approximately f_v= 5%, 10%, 20%, and 40%, such that the optical thickness, denoted by τ, remains constant in each case:

$$\tau = K_{ext} H = \frac{3}{4} \frac{H}{a} f_v Q_{ext} \tag{3.14}$$

where K_{ext} and Q_{ext} are the dimensionless extinction coefficient and extinction efficiency calculated by Mie theory, and H is the dimensionless thickness of the target. This process allows us to apply simulations on a target ranging from a thick deposit with a dilute concentration of particles to a thin densely–packed slab (close to a monolayer in some cases).

Optical Properties (PWPP Method)

Material	Volume Fraction	Number of Particles	Optical Thickness	Dimensionless Thickness	Hemispherical Reflection	Hemispherical Transmission
Type 1	0.050	9611	0.232	80	0.089	0.114
Type 1	0.098	9611	0.174	40	0.075	0.082
Type 1	0.131	9611	0.153	30	0.070	0.069
Type 1	0.196	9611	0.098	20	0.050	0.040
Type 1	0.261	9611	0.066	15	0.033	0.023
Type 2	0.053	1284	0.867	80	0.094	0.482
Type 2	0.107	1284	0.681	40	0.084	0.408
Type 2	0.143	1284	0.570	30	0.079	0.353
Type 2	0.214	1284	0.409	20	0.082	0.252
Type 2	0.285	1284	0.250	15	0.061	0.160
Type 3	0.067	13127	0.937	80	0.202	0.216
Type 3	0.134	13127	0.722	40	0.169	0.156
Type 3	0.179	13127	0.592	30	0.143	0.117
Type 3	0.268	13127	0.411	20	0.092	0.062
Type 3	0.354	13127	0.329	15	0.0545	0.039
Type 4	0.046	1098	2.384	80	0.200	0.506
Type 4	0.091	1098	2.070	40	0.185	0.492
Type 4	0.122	1098	1.840	30	0.176	0.469
Type 4	0.183	1098	1.395	20	0.158	0.400
Type 4	0.244	1098	1.039	15	0.140	0.311

Optical Properties (RTE Method)

Material	Optical Thickness	Extinction Efficiency	Hemispherical Reflection	Hemispherical Transmission
Type 1	0.25	0.083	0.092	0.125
Type 2	1	0.620	0.096	0.574
Type 3	1	0.242	0.217	0.260
Type 4	2.5	1.813	0.213	0.512

Table 3.1: Table properties of the targets tested in this paper

The number of configurations required to produce relatively smooth directional distributions of reflection and transmission ranged between 500 and 1000. Depending on the target properties, such as particle size, refractive index, and the number of spheres in the sample, the total simulation time was a few minutes up to two days on the Auburn University compute cluster. The time required to run a VRTE calculation took about five hours on a desktop computer.

Given in 3.1 are relevant simulation parameters and global calculation results for the PWPP simulations. The four test cases correspond to 1: $a = 1,\ \mathsf{m} = 1.31$, and RT optical thickness $\tau = 0.25$; 2: $a = 2,\ \mathsf{m} = 1.31,\ \tau = 1$; 3: $a = 1,\ \mathsf{m} = 1.5 + 0.01\mathrm{i},\ \tau = 1$; and 4: $a = 2,\ \mathsf{m} = 1.5 + 0.01\mathrm{i},\ \tau = 2.5$. Thedirectional-hemispherical reflection and transmission given in 3.1 denote the diffuse values, whereas the PWPP optical thickness corresponds to that calculated from the line-of-sight optical transmission. For the particle sizes and refractive index used in the simulations, and for a fixed RT optical thickness, an increasing particle volume fraction results in a decreasing hemispherical reflection and transmission; this result is consistent with our previous investigations [110].

Shown in Figs.3.3–3.6 are plots of diffuse transmission (scattering angle $0 \leq \theta < 90^\circ$) and reflection ($90^\circ < \theta \leq 180^\circ$) matrix elements for the four cases. The solid curves correspond to PWPP results at different particle volume fractions, and the dashed curve is the VRTE prediction. The S_{11} values have been normalized so that they integrate over a sphere to unity; absolute values of S_{11} would be obtained by multiplying the plotted curves by the total diffuse scattered fraction (hemispherical reflection + transmission). In this regard the S_{11} curves show the relative distribution of scattered radiant energy; note that the PWPP total diffuse scattering, per 3.1, decreases with increasing particle volume fraction. For all four cases, the effect of increasing f_v is to shift the relative scattering distribution towards the backwards (reflection) directions. Not surprisingly, simulation results by PWPP method approach to those by VRTE as the particle volume fraction decreases. In particular, VRTE

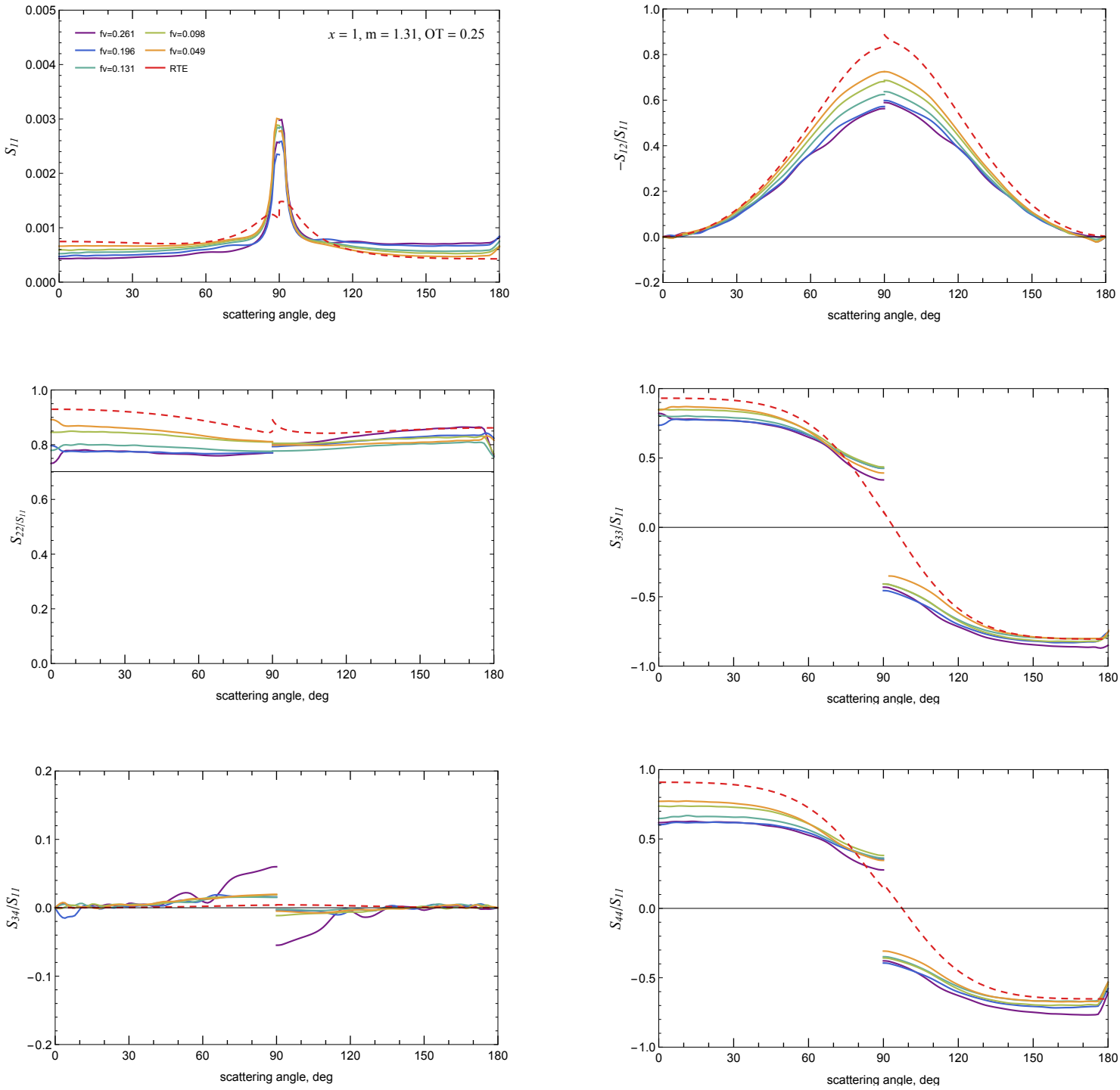

Figure 3.3: Six elements of scattering matrix are depicted as a function of polar scattering angles for different target thicknesses. The results of VRTE simulations (red dashed lines) and PWPP simulations (solid lines) are compared for $m = 1.31$, $x = 1$.

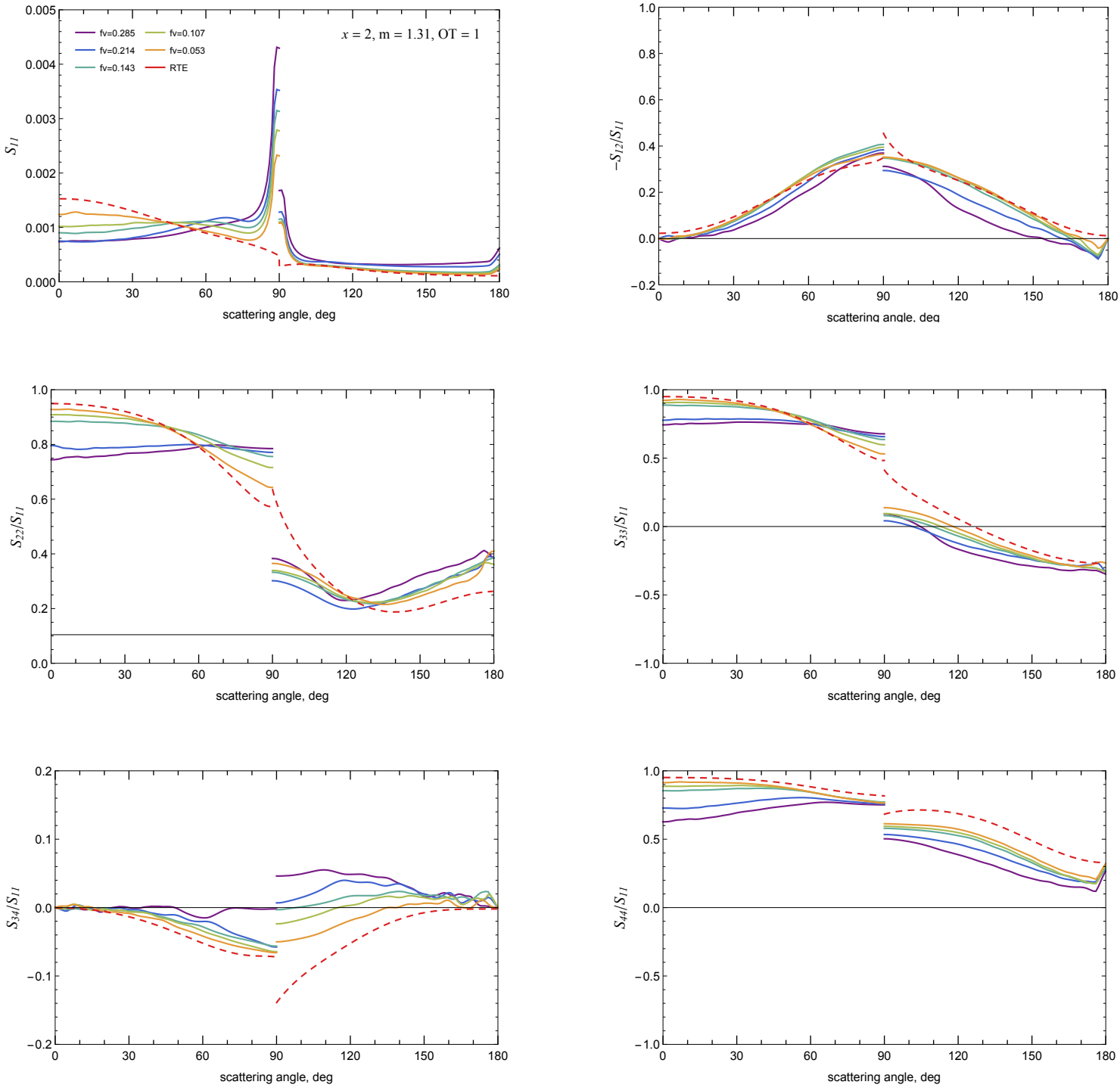

Figure 3.4: The same as in Fig.3.3, except particle size parameter is $x = 2$.

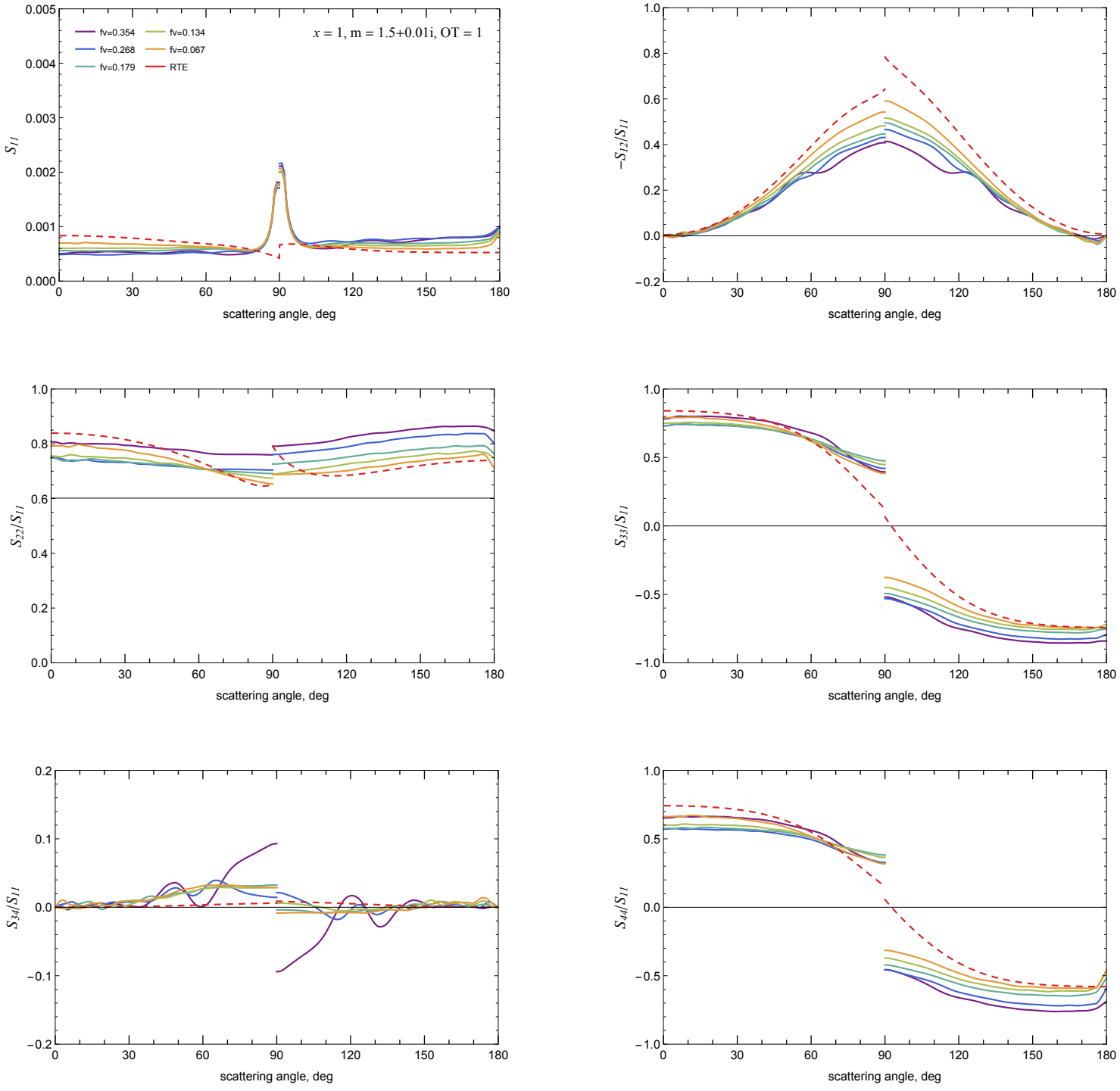

Figure 3.5: The same as in Fig.3.3, except the refractive index and particle size parameter are $m = 1.5 + 0.01i$ and $x = 1$.

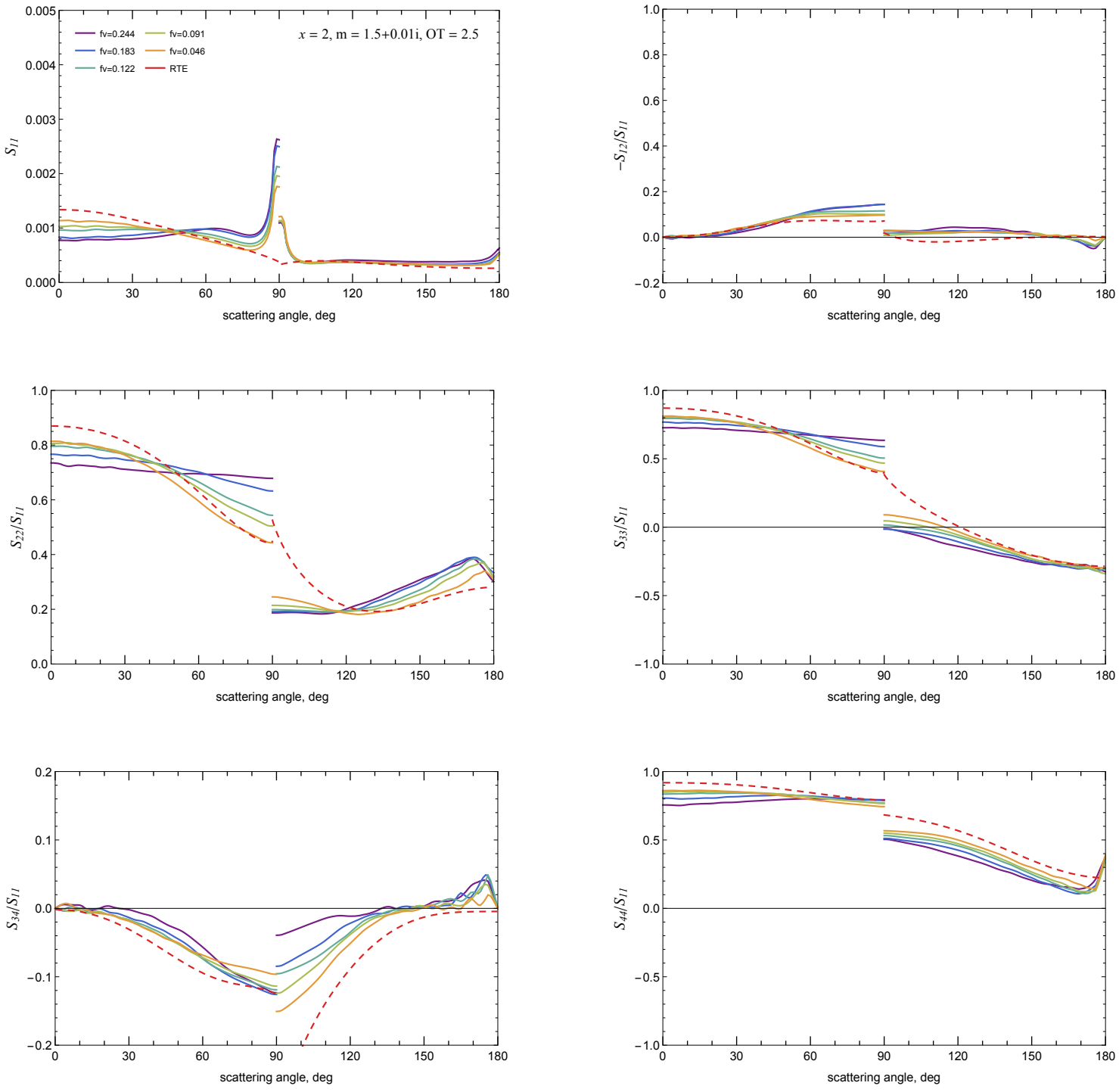

Figure 3.6: The same as in Fig.3.3, except the refractive index and particle size parameter are $m = 1.5 + 0.01i$ and $x = 2$.

and PWPP measurements for f_v= 5% are in relatively close agreement, while the PWPP results monotonically depart from VRTE as particle concentration increases. This simulation result is consistent with observations by Mishchenko et al,. and Muinonen et al,. [92, 97]. We note that for the sphere size parameters used here, a volume fraction of 5% will generally comply with the mutual far–field scattering zone condition that is a basis of the VRTE derivation [126, 96, 73, 15].

An increasing particle volume fraction tends to shift the polarimetric ratio curves in Figs. 3.3–3.6 uniformly away from the radiative transfer results. This shift is generally monotonic (increasing f_v = increasing shift), yet one exception is in Fig. 3.3 for S_{22}/S_{11} for which the direction of the shift undergoes a reversal at $f_v \sim 0.2$. With the important exception of the backwards scattering region ($\theta \sim 180°$), particle concentration effects do not appear to create distinct features in the polarimetric ratio curves.

3.3.1 Opposition effects

A key distinction between the PWPP and VRTE model results are the coherent backscattering (CB) effects occurring in the small angular region about $\theta = 180°$. Such effects arise from phase interference of waves scattered by a discretely random inhomogeneous medium: in the backwards direction, such interference will be constructive and will lead to the so–called brightness opposition (BO) and polarization opposition (PO) effects [93, 89].

There have been several experimental and theoretical examinations into the dependency of the opposition effects to the optical properties of the scatterers. Nelson et al. in 2000 ([101]) discussed this dependency to the particle size parameter and compared their experimental measurements to the theoretical results by Mishchenko ([88]). The PO effects by the regolith surfaces had been observed and studied by Shkuratov et al. in [117], in which simulations were conducted to show how different optical properties such as albedo, particle size, and volume packing density affect the coherent interference. The works by Hapke et al.

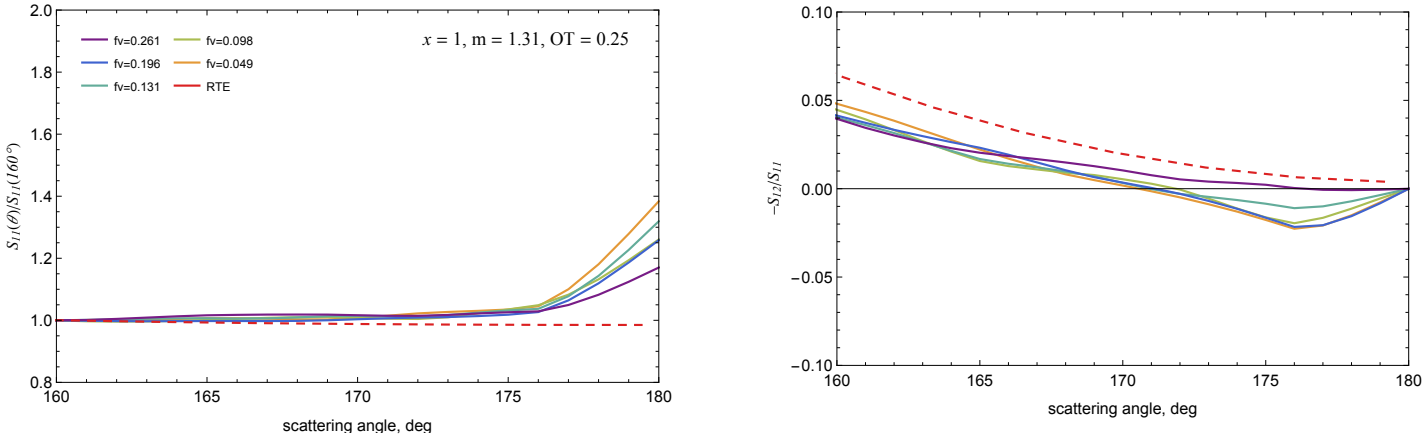

Figure 3.7: S_{11} and S_{12} at the coherent backscattering direction as a function of polar scattering angles for different target thicknesses. The results of VRTE simulations (dotes lines) and PWPP simulations (solid lines) are compared for $m = 1.31$, $x = 1$.

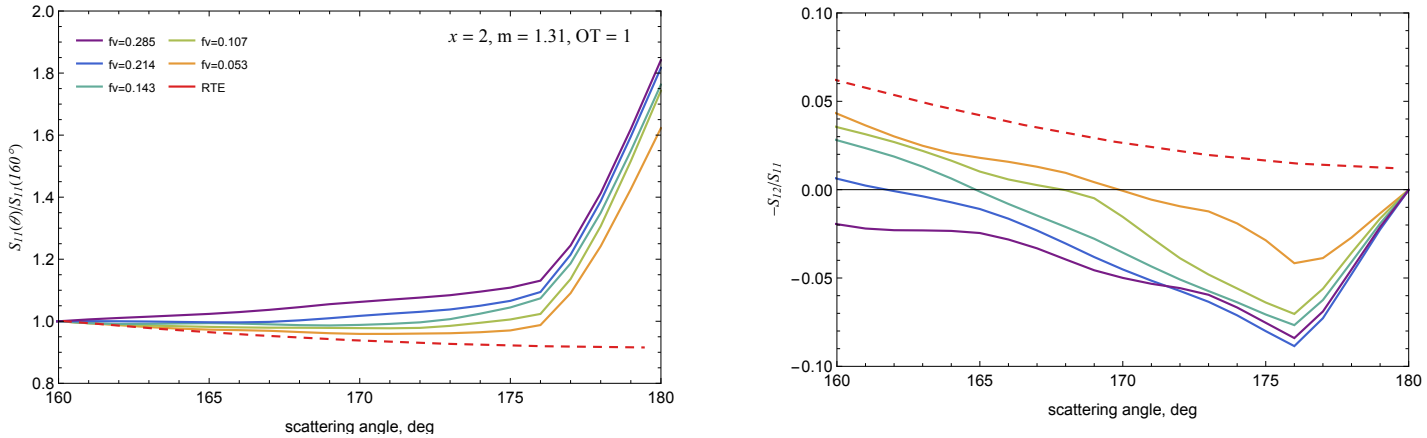

Figure 3.8: The same as in Fig.3.7, except particle size parameter is $x = 2$.

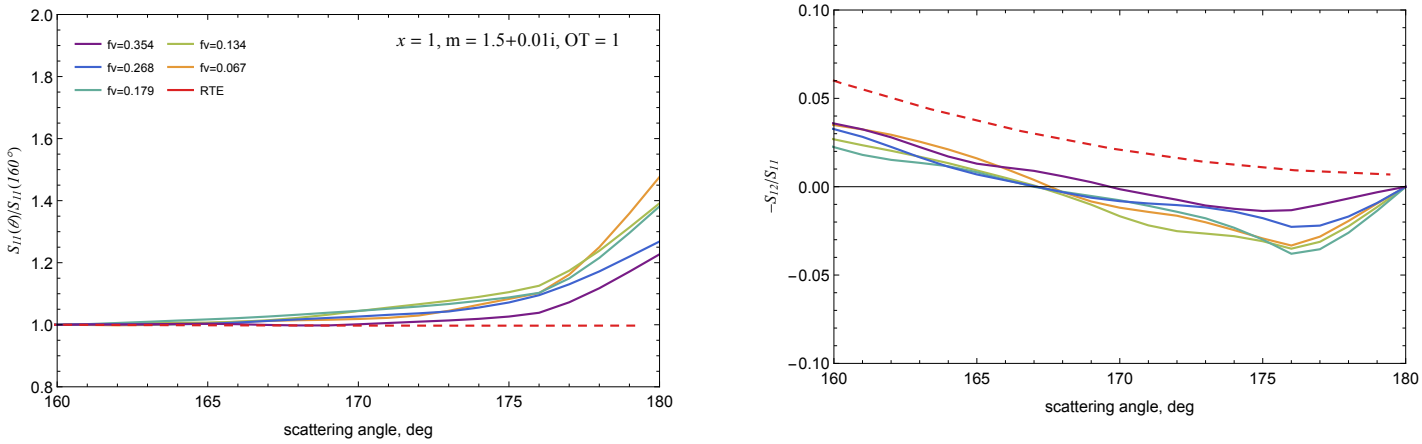

Figure 3.9: The same as in Fig.3.7, except the refractive index and particle size parameter are $m = 1.5 + 0.01i$ and $x = 1$.

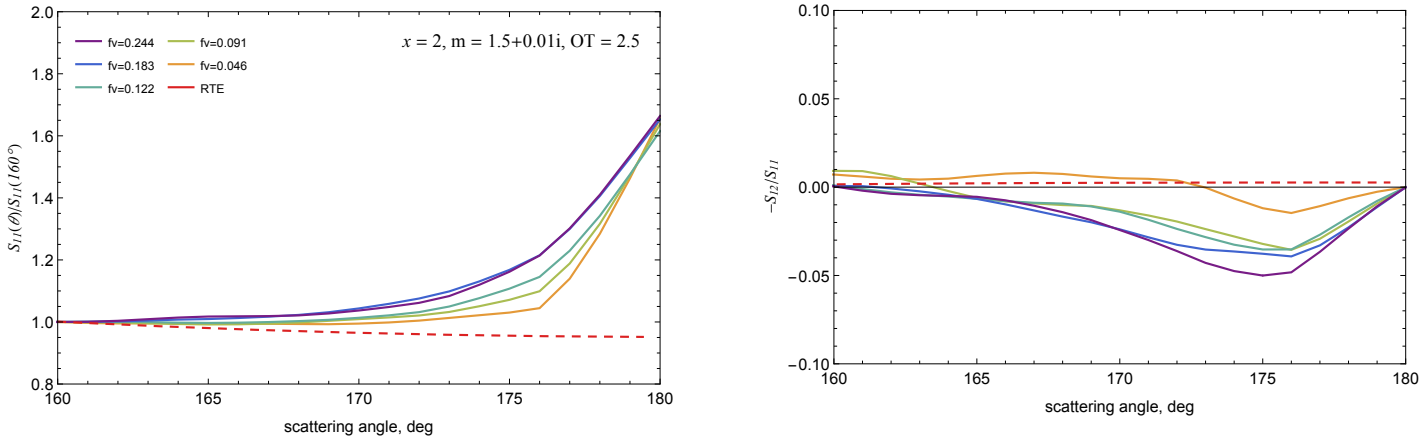

Figure 3.10: The same as in Fig.3.7, except the refractive index and particle size parameter are $m = 1.5 + 0.01i$ and $x = 2$.

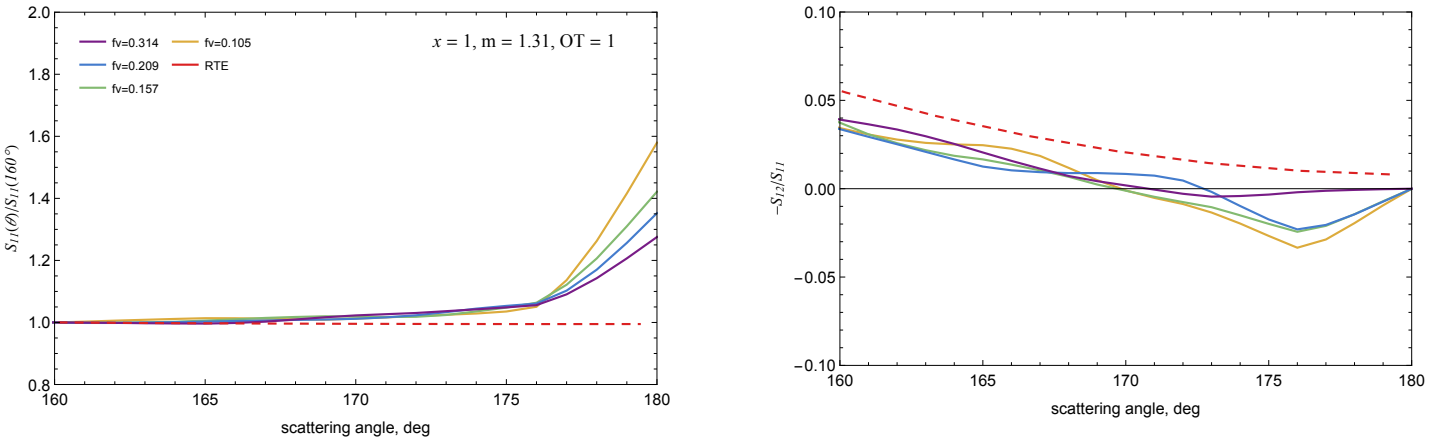

Figure 3.11: The same as in Fig.3.7, except the refractive index and particle size parameter are $m = 1.31$ and $x = 1$.

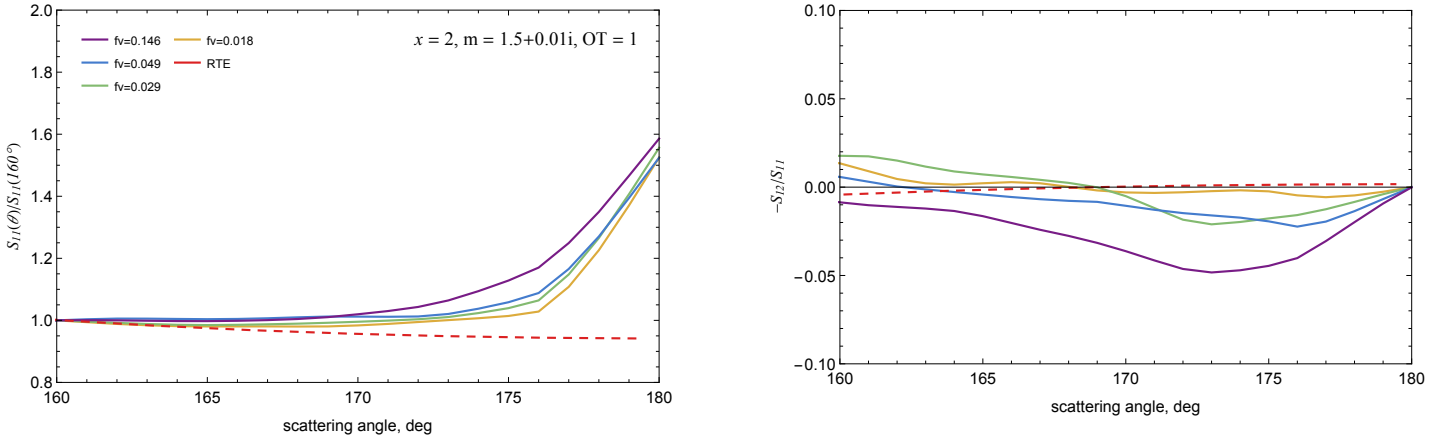

Figure 3.12: The same as in Fig.3.7, except the refractive index and particle size parameter are $m = 1.5 + 0.01i$ and $x = 2$.

[49], [50] and Helfenstein et al. [51] provide results showing that low albedo targets create pronounced brightness opposition peaks. It has also been shown in [24] that the angular width of BO and PO peaks increases as the particle size parameter become smaller. The dependency of CB peaks to its baseline is explained by Mishchenko et al. in the book [94].

Details of the S_{11} and $-S_{12}/S_{11}$ reflection predictions, in the range $160^\circ \leq \theta \leq 180^\circ$, are shown in Figs. 3.7-3.10. As is seen in the graphs, all PWPP model results produce a BO peak at 180° and a negative polarization branch. Such behavior is absent in the VRTE model, which is incapable of accounting for phase interference effects. For the specific calculation parameters used here, the height of the BO peak appears to be strongly dependent on the dimensionless particle size and the particle volume fraction. For size $a = 1$ and both values of refractive index, increasing volume fraction results in a decreasing BO peak, whereas the opposite trend is the case for $a = 2$. In all results the height of the peak ranges from 1.2 to 1.8 of the baseline S_{11}; theoretically, the maximum BO peak height must be twice the baseline or less [94]. A precise estimation of the width of the BO peak is difficult due tothe fact that the width is only marginally larger than the PWPP angular resolution, which for the calculations performed here is approximately $\Delta\theta \sim 2\pi/W \sim 3.6^\circ$. Nevertheless, the size $a = 2$ results, for both refractive indices, indicate that the width of the BO peak increases with increasing volume fraction; this is consistent with the theoretical understanding of brightness opposition, for which the width of the peak is inversely proportional to the mean free path, and, for fixed particle properties, will increase with increasing particle concentration.

Analogous trends are seen for the polarization opposition effects in Figs. 3.7–3.10. The depth of the PO branch decreases with volume fraction for size $a = 1$, and the opposite trend occurs for $a = 2$. Likewise, the $a = 2$ particles produce a wider negative polarization branch than that for $a = 1$.

To examine the effect, if any, of the optical thickness on the BO and PO behavior, additional calculations were performed, corresponding to $a = 1$, $\mathsf{m} = 1.31$ with $\tau = 1$ (i.e.,

the optical thickness used for the $a = 2$ ice particles), and $a = 2, \mathsf{m} = 1.5 + 0.01\mathsf{i}$ with $\tau = 1$ (that used for the $a = 1$ mineral particles). Results, which are shown in Figs. 3.11 and 3.12, are entirely consistent with those previously discussed: increasing concentration results in a smaller BO peak and negative polarization branch for $a = 1$, whereas the opposite is the case for $a = 2$.

We should mention that in the PWPP method, the prime function of the unit cell is to model a sufficiently large representational sample of the inhomogeneous medium. In this regard, the size requirement for the cell (i.e., the choice of dimensionless cell width W) is that it be well in excess of the largest length scale characterizing the structure of the inhomogeneous medium; this length scale will typically be on the order of the particle size. We use a cell width of 100 in the calculations, and this choice is dictated more on the need to provide sufficiently small angular resolution ($2\pi/W$) of the scattered field. To test whether the results were independent of W, we performed a limit set of calculations using a cell width of 150, and results from these calculations were not significantly different than those for W=100. An illustration is given in Fig. 3.13, which shows the BO peak for the particle conditions of Fig. 3.7, corresponding to $f_v = 0.261$, as calculated for W=100 and 150.

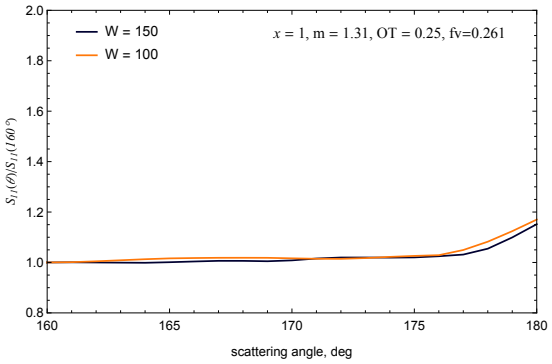

Figure 3.13: S_{11} at the coherent backscattering direction as a function of polar scattering angles for targets of different widths, w=100 and w=150.

3.4 Conclusions

The exact plane wave plane parallel (PWPP) and the phenomenological VRTE methods have been used to predict the polarimetric scattered radiation fields by monodisperse, randomly distributed wavelength–sized spherical particles. Our predictions indicate that an increase in particle volume fraction shifts the angular distribution of scattered radiation towards the backwards direction, relative to that predicted by a RT model with the same particle size, composition, and optical thickness. In addition, increasing particle concentration generally – but not always – results in a monatomic shift of the S_{ij}/S_{11} ratios away from the VRTE predictions.

The PWPP model can predict brightness opposition and polarization opposition features that are consistent with previous modeling efforts using exact simulation methods [24]. Further refinement of the PWPP model is needed to extent the angular resolution of the method while maintaining tractable computational overhead. For the present, random–media based modeling efforts, the dominant fraction of the PWPP computational time is spent on collecting an adequate number of solutions to specific, randomly–sampled particle configurations in the unit cell, so that the speckle features, which dominate the scattering patterns for specific solutions, can be sufficiently averaged out to reveal the bulk medium behavior. Our current efforts are aimed at finding some shortcut to this issue.

Chapter 4

Direct simulation of spectral reflectance by pigment–binder coatings.

Abstract

In this research we studied the prediction of spectral reflection and transmission by pigment-binder coatings in order to examine the effects of physical and optical properties of pigment particles such as chemical composition, particle volume fraction, and particle size parameter. The simulations have been performed using the Plane Parallel Plane Wave (PWPP) method which is based on a solution to the frequency domain Maxwell's equations for particulate systems excited by plane wave incident fields. The primary objective of this project stems from detecting potential materials which produce similar reflectivity of titania (titanium dioxide) particles and identifying conditions that reduce the diffuse and coherent transmission of visible light through particulate deposits.

4.1 Introduction

Titanium dioxide (TiO_2, titania) particles are present in various aspects of human daily life [133, 123, 120, 7]. In recent decades, these particles have been considered as an alternative material of many resources of light scattering in papers, plastics, coating, sunscreen, inks, food coloring, and pigment materials mainly due to their high reflectivity, the whitening effect, and that they are inert material (mechanically and chemically stable).

The TiO_2 powder is produced from a variety of titanium ores via the older sulfate or newer chloride processes [39, 31, 32]. After mineral products are purified they are converted into crystalline pigment particles in specific sizes. Both methods, sulfate and chloride, produce pigment grades in crystal forms; however, titanium dioxide bash particles produced by sulfate process are usually utilized in paper or fiber productions due to having softer properties. In general, the production process of the TiO_2 particles is so competitive and mostly confidential so it is almost impossible to describe all available production processes and its cost in details. More details of the production process can be find in [99, 116, 84].

Over the years, TiO_2 is the highest opacifying pigment used in coating industries, but it is also the most costly one. High demand of titanium dioxide particles and the supply shortage have forced coating industries to find a balance between cost and quality. One method includes partial substitution of TiO_2 with low-cost pigments. So finding a less expensive material that doesn't reduce quality and effectiveness is substantial to reducing the cost of TiO_2 formulations.

In this chapter, we examine the directional-hemispherical reflectance by non–TiO_2 pigment systems. First, the effects of the pigment optical and physical properties (such as the particle size, volume concentration, particle shape, and the layer deposit structure) have been tested on scattering characterizations of pigment-binder coatings composed of randomly positioned TiO_2 particles. We also studied the effects of adding to, or replacing the TiO_2

pigment material by particles having different chemical compositions. In this simulation, the layer deposit was modeled as a system composed of TiO_2 and non–TiO_2 pigment particles in spherical, rectangular cubic, and ellipsoid geometries.

We also conducted simulations to examine how particle configurations such as crystal structure, alter reflection. The primary goal was that how particle arrangements and movements affect scattering properties. A subroutine by MATHEMICA software was developed to create a perfect lattice by TiO_2 particles and these particles were osculating around their positions in random directions till perfect random media was created. For the next section, the aggregation effects have been studied. To achieve this goal, A FORTRAN code has been developed to create an aggregate modeled deposit from a perfect random medium. The process starts with N monomers, and sequentially assembles aggregated particles by combining one pair of particles at a time. Using the PWPP code, one can measure the effects of adding agglomeration to the system on reflected energy. The particle configuration algorithm has been modified to include spacer particle components into the system. The basic idea is that the spacer particles can be solid or hollow air–filled spheres, with a refractive index equal to the binder. Computations will examine the effects of spacer particle radii and volume fractions, and shell thickness, on the spectral hemispherical reflectance.

4.2 Computational results and discussion

As we discussed the PWPP method in the chapter 2, the methodology provides the comprehensive computational tools to predict the scattering properties of particulate plane parallel media. In this study, we examined how changes to the pigment particle characteristic such as particle size distribution (PSD), particle size, particle packing density, refractive index, and particle positions alter the optical properties e.g., albedo, extinction coefficient, optical thickness, and spectral scattering properties of the film. As opposed to the phenomenological RTE/VRTE technique, the PWPP method is based on the direct solution to the Maxwell's

wave equations (MWEs) so it simulates physical first principles and represents all relevant pigment, binder characteristics (particle aggregation, anisotropic material, particle shape).

The pigments–binder systems, in these computations, are composed of randomly positioned particles and are generated using Monte Carlo method with a known microscopic configuration of the film and the particle distribution function. As mentioned in the last chapter, the framework of the PWPP method is based on the periodic plane parallel system so the deposit is modeled as an infinite film in the lateral directions. The method solves the MWEs for the given configuration and repeats the calculations to find an average of the solutions. Note that the number of the average processes depends on the tolerance parameter and the solution fluctuation. Similar to other computations in this research all the lengths are scaled based on the wavenumber ($k = 2\pi/\lambda$) and medium thickness is extended to $\pm\infty$ in x–y plane to represent a plane parallel medium. The incident field is considered in normal direction in the following computations. All input quantities are listed and can be found in the following table, table 4.1.

A FORTRAN-90 implementation is used to develop the PWPP code which was run on the Auburn University super cluster. Each PWPP data point is generated based on the average of the 10 randomly—sampled configurations of the target. The time required to run each data point is varying between 5 min to 3 days depends on the number of particles on the system. Also, it is important to note that the calculation performed in this study were basically a shakedown cruise for the PWPP method as applied to TiO_2-binder systems. Specifically, we determined the parameters in the numerical method which optimizes the solution time for the system. We established that the method can, in a reasonable amount of computational time and resources, compute reflection for relatively thin (H=20-30) systems. Also, the method was tested to calculate reflection for systems that are optically thick, corresponding to a line-of-sight transmittance through the medium

Optical and physical properties	**Quantities used in simulations**
Dimensionless target width	W = 100
Dimensionless target thickness	Depends on the application
Reflective index of TiO_2	m = 2.7
Reflective index of the mixing material	m = 2.4
Reflective index of the binder material	m = 1.54
Reflective index of the back surface material	m = 1.54
Reflective index of the front surface material	m = 1.54
Incident direction	$\theta = 0$, $\phi = 0$ (normal incident field)
Particle shape	Depends on the application
Wavelength	560nm
Particle diameter (for TiO_2)	232nm
Particle size parameter (for TiO_2)	x = 1.302
Particle diameter (for m=2.4)	275nm
Particle size parameter (for m=2.4)	x = 1.543
Particle volume fraction	Ranging from 0 to 0.4
Particle PSD standard deviation	0.186
Deposit optical depth	Depends on the application
Dipole spacing	0.2
Number of configurations	10 - 50
Sticking probability (in aggregation calculations)	1
Rotation probability (in aggregation calculations)	0

Table 4.1: Table of optical and physical properties used in this chapter

of 0.01 or less. This simulation is more important in the sense that the PWPP code is able to do the computations for thicker deposit condition.

In overall, the objective of the calculations is to identify conditions that maximize the hemispherical reflectance for a fixed layer thickness and fixed volume of pigment material that can meet the real condition of pigment–binder coatings. The layer thickness used in the calculations will be on the order of 5μ to 10μ, which should be sufficient to capture the effects of multiple scattering among the particles.

4.2.1 TiO_2 particles

Shown in Fig.4.1 is the directional-hemispherical reflection by a system of spherical TiO_2 particles (m=2.7) with size parameter of 1.302; this corresponds to a volume-mean diameter of 232nm at 560nm wavelength. Each solid curve in the figure corresponds to a system of a fixed thickness (dimensional thickness$\times 2\pi/\lambda$) which is ranging from 10 to 100.

As it was expected, the reflectance monotonically increases as the target gets thicker. However, target thickness variations have more effects on thinner slabs comparing to the thicker ones. As the deposit thickness becomes larger than around 60, the reflection does not change significantly with increasing the layer thickness.

Also, not surprisingly, increasing the pigment volume fraction led to the increment of the hemispherical reflection. However, this effect is negligible for larger TiO_2 packing density (larger than 0.15). Note that the hemispherical reflection by the system decreases as the deposit volume fraction become larger than 0.24.

4.2.2 Replacing TiO_2 particles

The main purpose of this section is to identify materials with different chemical compositions that added to or replaced by the TiO_2 pigment particles so the whole system can have the same scattering characterization as pure TiO_2 particles. Two types of replacement

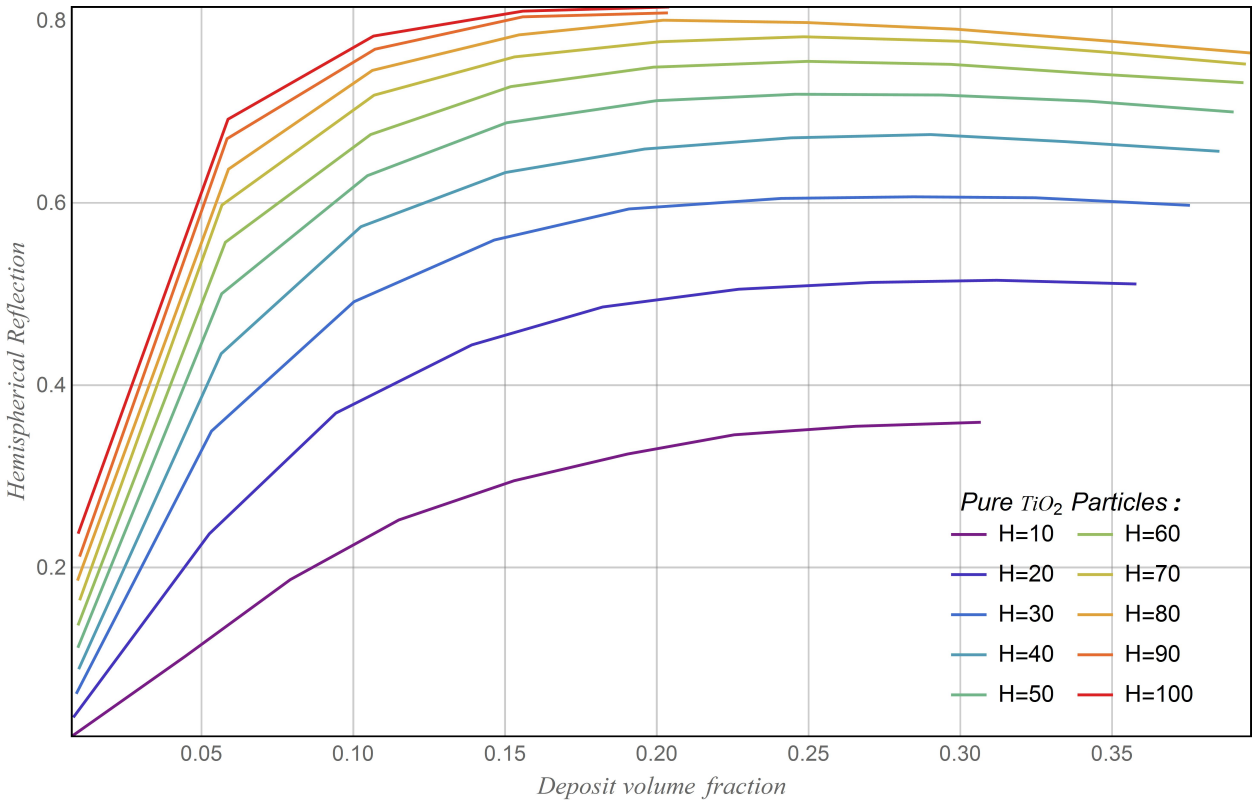

Figure 4.1: Spectral reflection as a function of particle packing density for systems in various thicknesses composed of TiO_2 particles.

material were considered, corresponding to refractive indices of 2.1 and 2.4. It should mention that all components in this computation have spherical shapes with a lognormal PSD with dimensionless standard deviation of 0.1. The binder material used in these calculations has a refractive index of 1.54, and the binder/pigment film is backed by a substrate with refractive index of 1.54 (i.e., pure binder). Calculation performed for deposits of m=2.1 (type 1 material/particle) and m=2.4 (type 2 material/particle) consisted of particles with radius ranging from a=200nm to 300nm at the wavelength 560nm. Computational results are shown in Figs.4.2 and 4.3. Each plot in the figures represents the spectral reflection as a function of particle volume fraction for various deposit thicknesses for a fixed particle size.

One can observe that type 1 particles are incapable of producing reflection radiation fields anywhere close to titanium dioxide particles. This is not surprising, since the contrast between m=2.1 and the binder (m=1.54), is relatively small. Fig.4.3 indicates the computational results for type 2 material. One can see that these particles could produce reflection comparable to TiO_2 powders.

Fig.4.4 shows reflection vs. volume fraction for a system of particles of type 2. The thickness is fixed at H=30, and sphere size parameter is ranging from x=1.122 to 1.683. Shown also are the results from Fig. 1, i.e., TiO_2 reflection vs. volume fraction at a thickness of H=20 (the dotted line). One implication of the plot is that the m=2.4 particle size has a relatively small effect on reflection. The plot also shows that a system of m=2.4 particles, with H=30 and f_v= 0.3, could produce reflection comparable to a TiO_2 system at 2/3 the volume fraction and 2/3 the thickness.

4.2.3 Adding non–titanium dioxide particles to the system

Following simulations in this work were carried out on the basis of the results of last sections. It was shown that materials with refractive indices m=2.1 and m=2.4 are incapable of

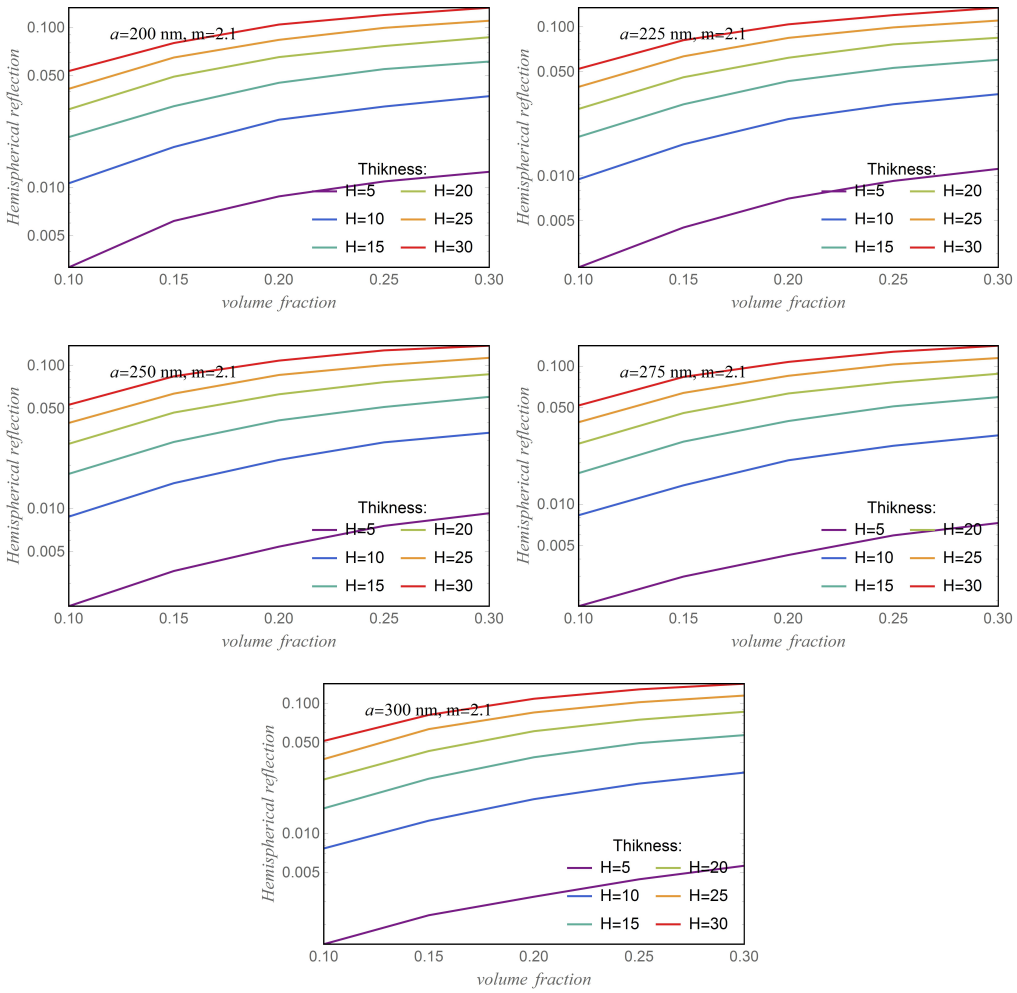

Figure 4.2: PWPP computations for spectral hemispherical reflectance from modeled deposit with refractive index of m=2.1 as a function of particle volume fraction.

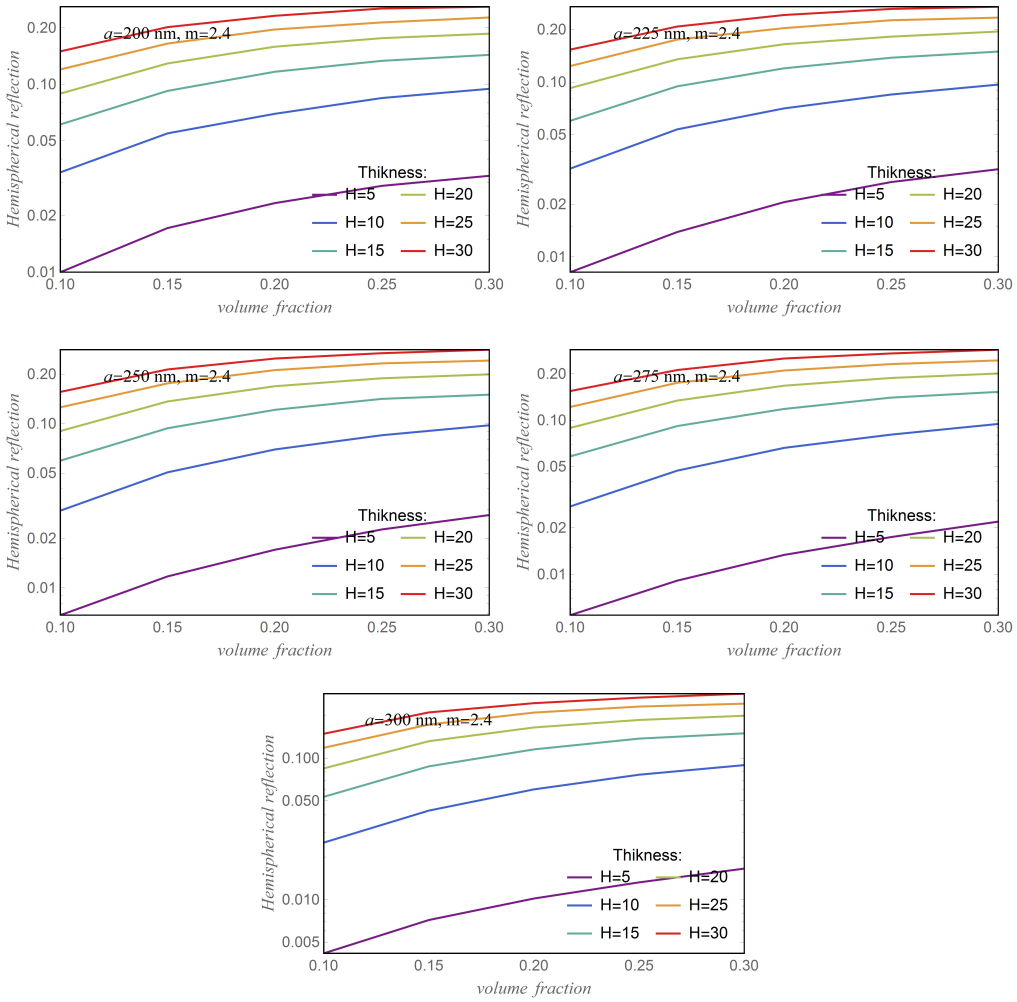

Figure 4.3: The same as Fig.4.2 except for particles with refractive index of m=2.4.

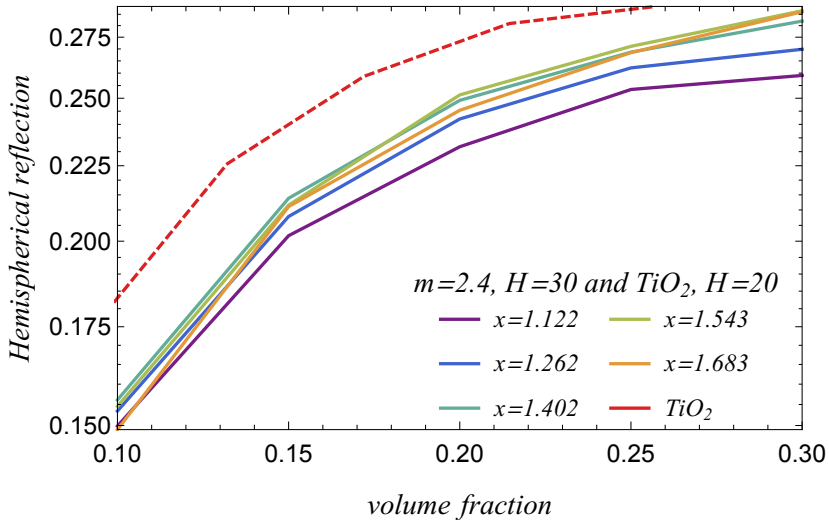

Figure 4.4: PWPP computations for spectral hemispherical reflectance by deposit with m=2.4 at different particle size comparing to the TiO_2 particles.

replacing reflection fields produced by TiO_2 particles. However, the latter substance could produce larger reflectance comparing to the former one.

The PWPP calculations in Fig.4.5 are the results for directional-hemispherical reflection by a system of a mixture of spherical particles corresponding to refractive indices of 2.7 and 2.4 with size parameters 1.302 and 1.543 respectively. The horizontal coordinate is the total volume fraction of the particulate material in the layer, the layer thickness is fixed at 50 ($dimensionalthickness \times (2\pi/\lambda) = 50$). Each curve in the figure represents a modeled deposit consisted of TiO_2 particles with constant volume fraction as the mixing particles are added to the system, and its particle density is increased to 40%. The dotted line is the result from Fig.4.1, the simulation results of a deposit composed of pure pigment particles for a volume fraction ranging from 0.009 to 0.37.

One can see that addition of the m=2.4 material to a system containing m=2.7 material increases reflection fields. However, this increment in negligible as the packing density of the system is getting close to 0.15 and this is due to the fact that system is basically saturated insofar as multiple scattering is concerned. Moreover, hemispherical reflection by the system

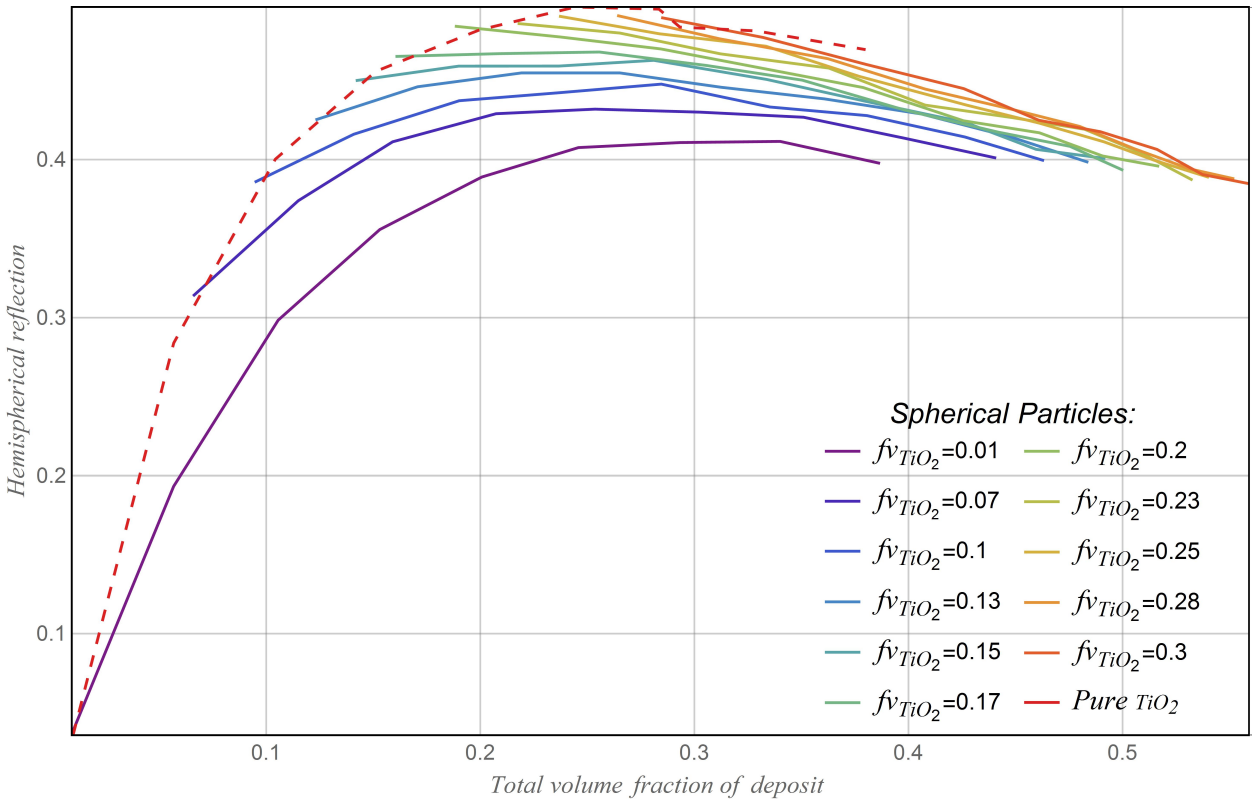

Figure 4.5: PWPP computations for spectral hemispherical reflectance by a composite modeled deposit composed of spherical TiO_2 and type 2 particles with non–dimensional thickness of 50.

decreases as the deposit volume fraction become larger than 0.24 and this effect can be observed in all cases even for the system of pure pigment material.

4.2.4 Different particle shape

Due to the diversity of particle shapes in natural pigment particles, it is questionable whether to use spherical particle shapes in simulations or not. This factor complicates accurate quantitative modeling of electromagnetic scattering. So we consider other particle shapes (e.g., cubic particles) in this study to examine how reflectance in randomly discrete media depends on the physical properties of scatterers.

Similar to the last section, the system is composed of TiO_2. Four categories of particle geometries were considered in the calculations including sphere, ellipse, cube, and rectangle with log-normal particle size distribution. All simulations have been performed for the layer of non–dimensional thickness $Hk = 50$, where k is the wavenumber ($k = 2\pi/\lambda$). The volume–mean dimensionless radius, 116nm at 560nm wavelength, is the same as that used for TiO_2 particles. The oval and rectangular particle geometries were defined such that the sphere and cube particles are elongated in one direction with aspect ratio of 2 and 3. Note that like other computations, the refractive index of the binder, back, and front surfaces is 1.54.

The results for reflected fields by a fixed layer thickness ($dimensionlessthickness = H = 50$) composed of TiO_2 particles in different shapes are shown in Fig.4.6,.

Comparing this result clearly show that scattering properties by the system are not affected by the particle shape significantly. It is due to the fact that the effective volume of the particles has not been changed and only particle shape has been replaced and the volume-mean parameter of all particle shapes follows the same distribution as that for the sphere. Yet, we can conclude that the assumption of spherical particle shape overestimates the reflected radiance among other geometrical shapes. Also, elongating particles in one direction decrease reflection for a fixed particle volume.

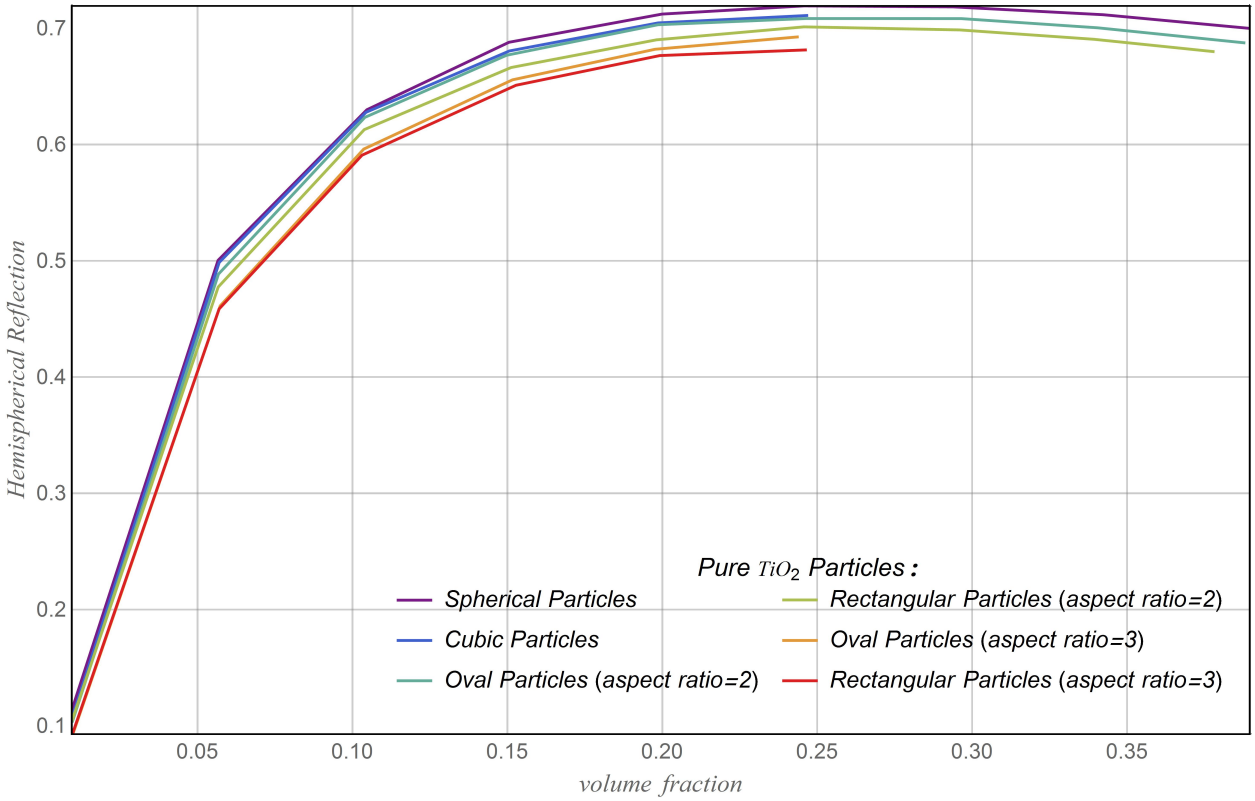

Figure 4.6: Computations for spectral hemispherical reflectance by a deposit of thickness 50 consisted of the TiO_2 particles in four different shapes.

4.2.5 Lattice structure and the effect of randomness movements in the lattice

The chemical and optical properties of a thin film composed of titanium dioxide particles plays an important role in various industries such as photovoltaic, photochromic, electro-luminescence, catalytic devices and sensors [100, 70, 63, 103, 38]. The key feature in this field is to understand how different morphologies of TiO_2 thin film surface alter the absorption capacities [40, 5]. Formenti [36] for the first time used TiO_2 as a photocatalyst and till this decade these particles have been used widely in water splitting, disinfection, and detoxification processes [86, 65, 66, 6].

The primary goal of this section is to study how the scattering properties by a pigment–binder film change as the pigment particles evolve from a perfect lattice structure to a random configuration. Note that all perfect lattice designs in our simulations are simple cubic structures with different number of particles in a fixed volume of a a thin deposit film ($HK = 20, WK = 100$). Particle size in the computation are considered as the same size of TiO_2 particles. Similar to other calculations the front and back surfaces had the same refractive index as the binder materials (m=1.54).

Simulations are begun with a perfect lattice structure composed of a small number of TiO_2 particles, $N_p = 25$, which represents a system of volume packing density f_v=0.001. In the next step, particles started Brownian motions around their previous positions. Particles are allowed to have random walks in the range of 0 to particle diameter size, 1.302, in random directions in each step. In order to have a perfect randomly positioned particles, we repeated each process in 6 different steps and each time particles started to move from their previous locations. Then a layer of particle lattice is added to the initial step, perfect lattice structure, and all procedures are repeated for a new modeled deposit lattice. The number of particles increases to 4055 representing a crystal layer with f_v=0.15.

The following figure (Fig.4.7) is an example of a simple cube crystal layer with f_v=0.021 as the particles diffuse away from their lattice positions.

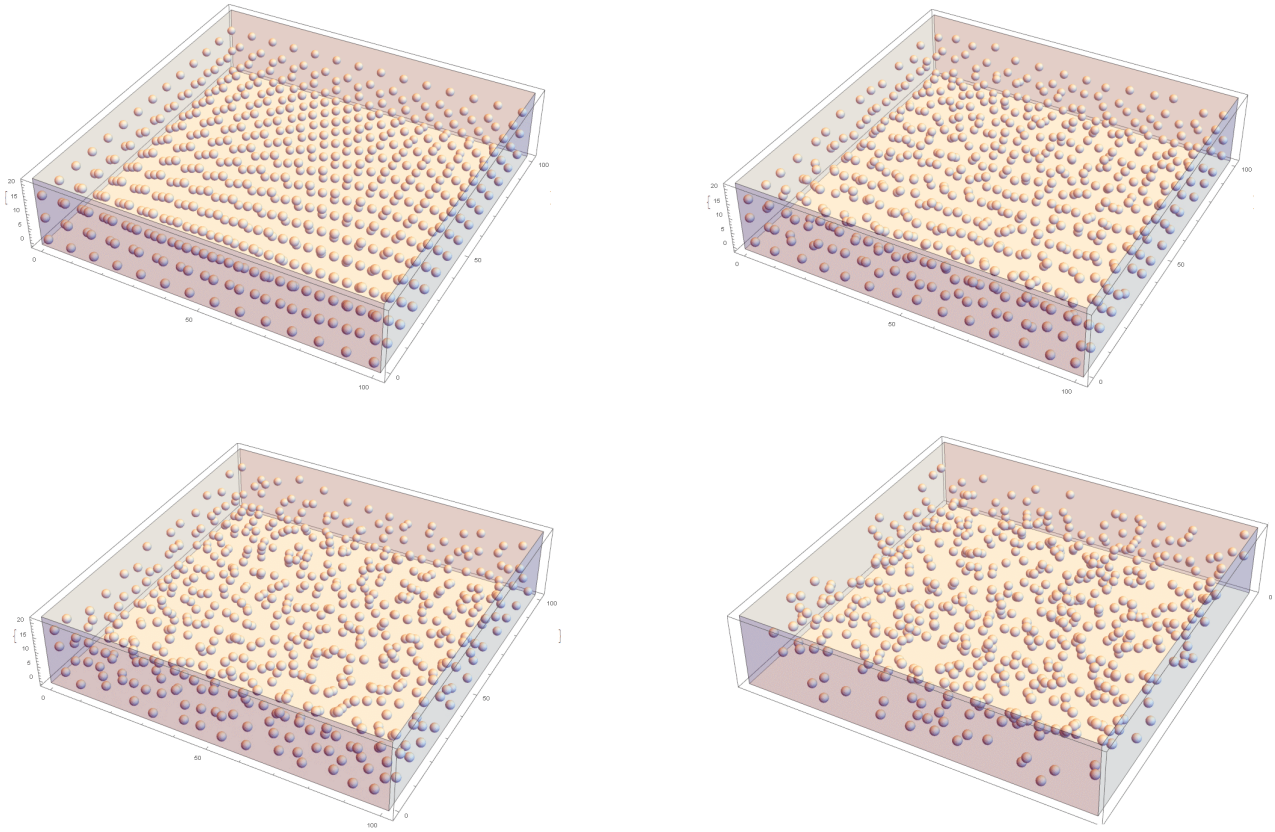

Figure 4.7: Graphics show a sampled deposit as particle positions deviates from the perfect lattice structure (left top picture) to a perfect random one (right bottom picture). The deposit is composed of particles with the size parameter of 1.302 representing the volume packing density of f_v=0.021.

Simulation results for hemispherical reflection are plotted in the Fig.4.8 as a function of the particle volume fraction. In this figure, the dotted-dashed purple line shows the reflection by the perfect lattice deposit as the particle number is increasing which is equivalent to increase the volume fraction of the medium since the target volume is constant. The solid lines represent 5 different steps corresponding to particles diffusion movements towards a random system. The dashed orange curve is the simulation results by perfect randomly positioned particles.

A remarkable feature of the dotted-dashed purple curve in Fig.4.8 is the sharp maximums for some volume fraction values. This dependency of the reflection by perfect lattice structures to the particle volume fraction can be difficult to analyze and it is required to study the scattering by diffraction grids and photonic crystals. As randomness is added to the system, the oscillation of hemispherical reflected radiation become more negligible; however, the sharp reflection peaks still can be observed in solid lines around the volume fraction of 0.06. The results for perfect random media is not surprising. The interference effects between the scattered fields for randomly positioned particles smooth the reflection curve.

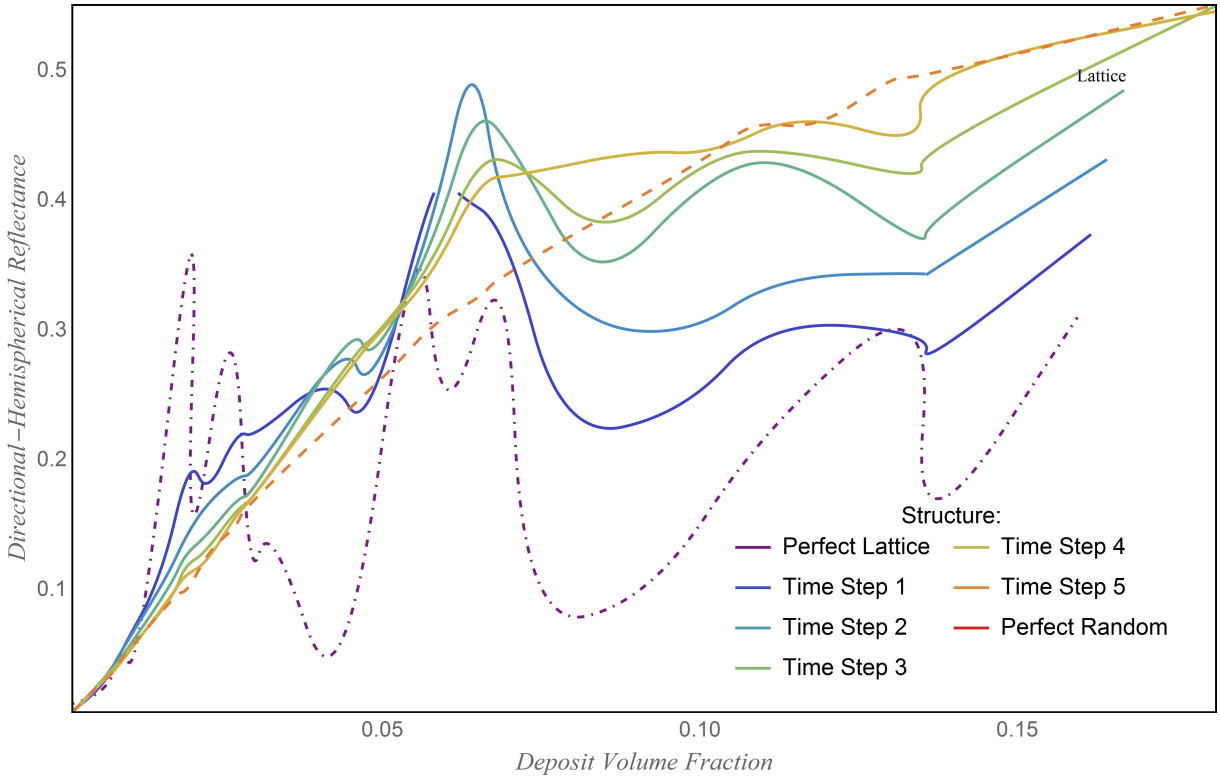

Figure 4.8: Computations for spectral hemispherical reflectance by the system composed of TiO_2 particles in different structures.

Investigating the effects of the particle randomness on the directional-hemispherical reflectance in perfect lattice systems arose a question which how the pair correlation function

(PCF) is changing in the sample deposits. Also, the visual inspection allows to distinguish more details in a crystalline and a random positioned structure. In this part, we attempt to address this issue by computing the PCF for two lattice configurations. Plots in Figs.4.9 and 4.10 illustrate the PCF measurements as a function of distance for systems of volume fractions of 0.15 and 0.10 respectively. Note that the pair correlation function or radial distribution function indicates how particle density in a particulate system depends on distance of a specified particles. In other word, PCF represents the probability of finding a center of a particle at a given distance from a reference particle.

One can see that the PCF computations for crystals include different peaks that is due to the lattice constant. As the randomness is adding to the system these peaks are smoothing out. The PCF is almost uniform and goes to 1 for randomly disperse particles. This pattern was expected since scatterers are not overlapped and have no structure in the perfect random system .

4.2.6 Adding spacer particles to the system

In this section, particles with a refractive index equal to the binder material (m=1.54, referred to as spacer particles) are added to the deposit. Similar to the previous parts, the effects are studied for a deposit with a fixed TiO_2 particle volume fraction (for each plotline) as the spacer particles were gradually added to the system. The spacer particles are essentially invisible (i.e., non–scattering), as they are index matched with the binder material. In this respect the spacer particle can have only an indirect effect on reflection, by altering the distribution statistics of the pigment particles. In this calculation, the dimensionless target thickness is H=20 and spacer particles have the same size as TiO_2 particles ($x_{spacer} = x_{TiO_2} = 1.302$).

Fig.4.11 shows the effects of adding the spacer particles to the system. Not surprisingly, a deposit with the larger packing density of TiO_2 particles has a higher reflection. However,

addition of the spacer particles does not affect the hemispherical reflection in any noticeable way. The oscillatory, slightly decreasing trend in reflection for volume fraction > 0.3 is likely an artifact with the Monte Carlo algorithm used to create the particle layer: the spacer particles were added first, followed by the TiO_2, and for high spacer volume fractions it becomes increasingly difficult to randomly find points in the system to place all of the titanium dioxide particles.

We also extended the calculations for the same system as the binder particle size parameter has been increased to the three times of the TiO_2 particle size parameter ($x_{spacer} = 3.906$). Results are presented in the Fig.4.12.

4.2.7 Aggregation effects

We also present simulations to examine the effects of pigment particle aggregation on the hemispherical directional reflection. To do this we developed subroutines for simulating Brownian diffusion and aggregation of the particles within the unit cell, and computations of reflection properties are performed at different points along the aggregation process. The volume-mean diameter of particles are the same: 232nm at 560nm wavelength.

The calculations begin with a random distribution of monomer particles (spheres) in the unit cell, per the standard Monte Carlo procedure. The monomers are then allowed to take random walks, in spatial steps of one discretization element at a time. Monomers coming into contact are assumed to stick to each other, and the combined particle (the aggregate) is treated as a single particle in subsequent diffusion steps. Ultimately the algorithm will produce a single aggregated particle, in the form of a fractal-like structure.

The following graphics (Fig.4.13) illustrate the structure of the cell at the initial condition and at the end of the aggregation process; the particles are represented as cubes to make the graphical rendering computationally tractable. As can be seen, the effects of aggregation are most evident for low particle volume fractions. The left pictures on Fig.4.13 represent

discrete randomly positioned particles of f_v=0.01 and f_v=0.05 and the right ones shows the same deposits for complete diffusion-limited aggregation.

Fig.4.14 illustrate the directional-hemispherical reflection for aggregated systems of spherical TiO_2 particles for different deposit volume fractions. The horizontal axis represents the number of diffusion steps (random walks).

The results show that for the system with volume packing density smaller than 10% the aggregation causes a sudden decrease in the hemispherical reflection. However, for larger particle density the effects of aggregation appear to be minor. Indeed, for volume fractions exceeding around 20%, the particle system will become completely aggregated (i.e., one continuous aggregate, analogous to an aerosol) in only a few hundred random walk steps. The plots are based upon a single simulation, and the noise/oscillations in the reflectance are likely artifacts due to the specific structure of the particle system; these effects would be damped out by averaging over multiple configurations.

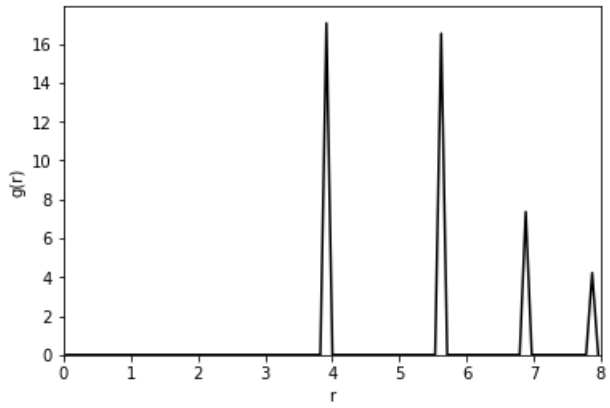

(a) Perfect lattice

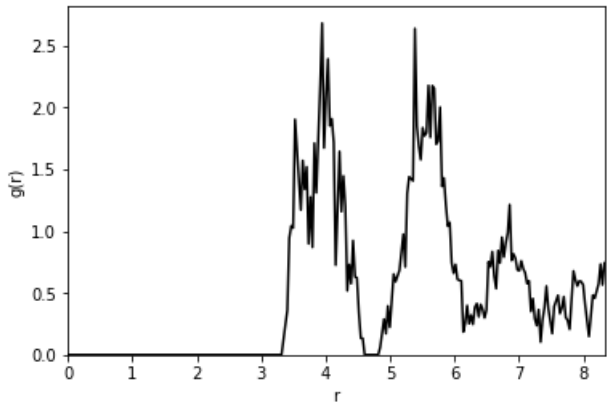

(b) Time step 1

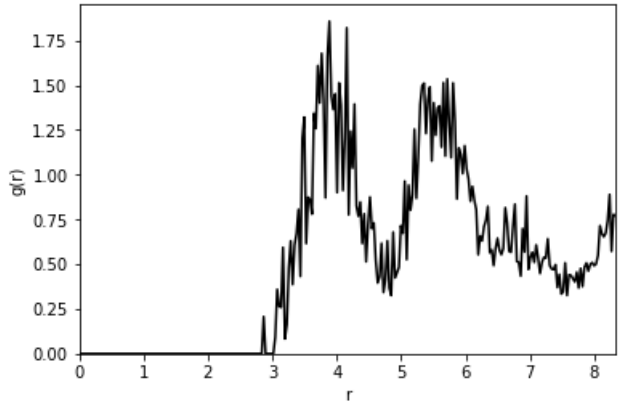

(c) Time step 2

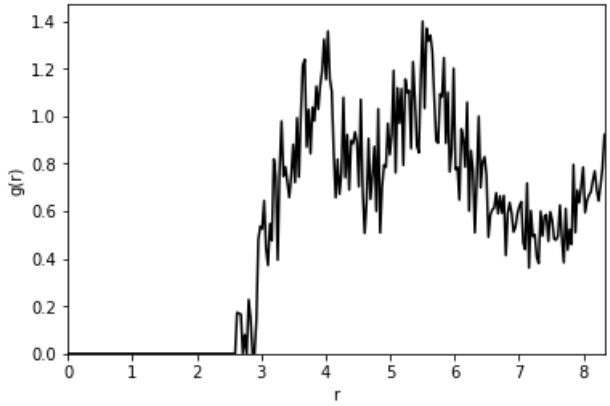

(d) Time step 3

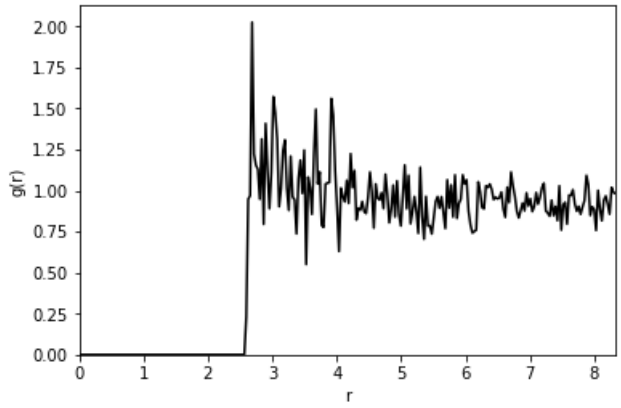

(e) Time step 3

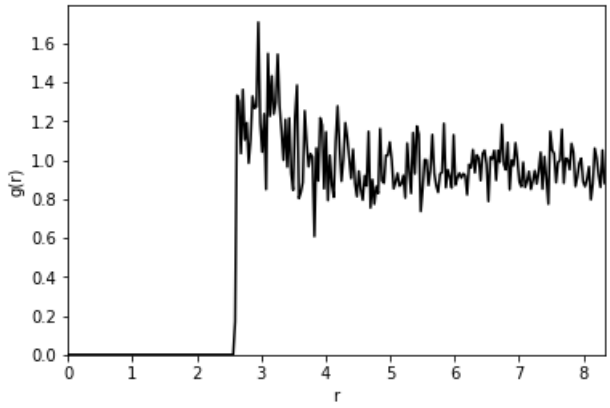

(f) Perfect Random

Figure 4.9: From left to right: perfect lattice as the randomness is added to the system. The deposit volume fraction and the dimensionless target thickness are f_v=0.15 and H=20.

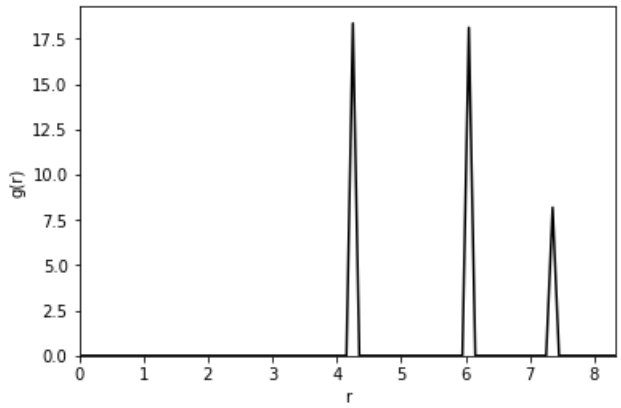

(a) Perfect lattice

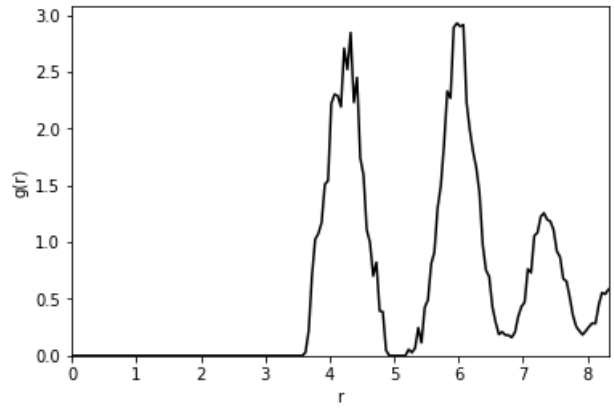

(b) Time step 1

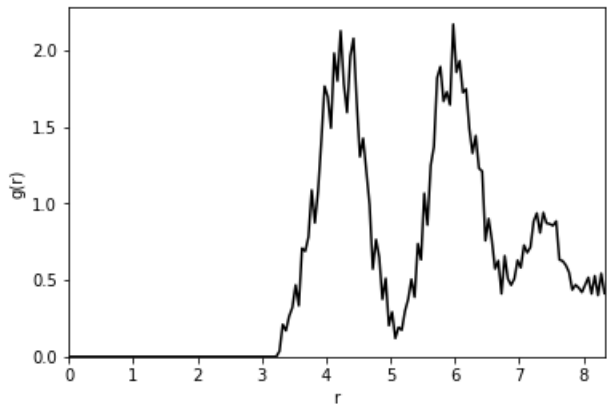

(c) Time step 2

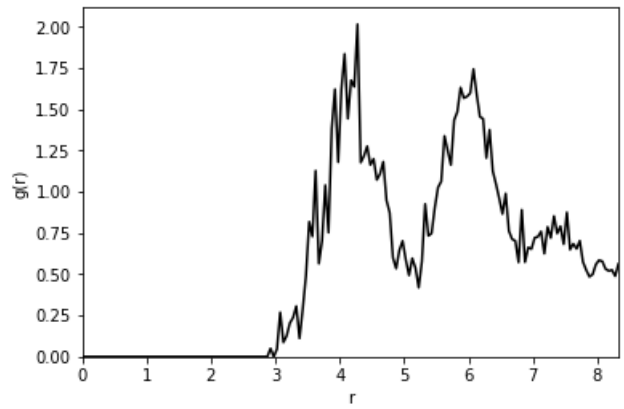

(d) Time step 3

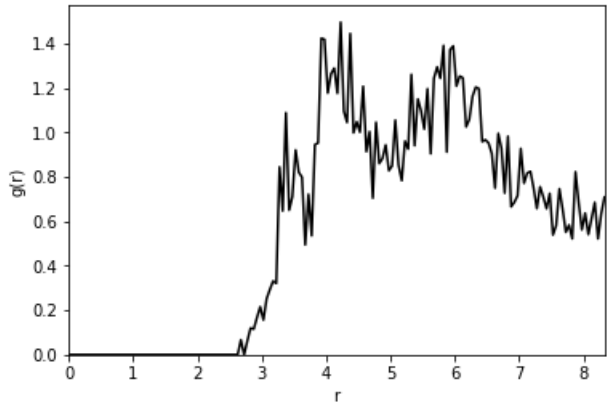

(e) Time step 3

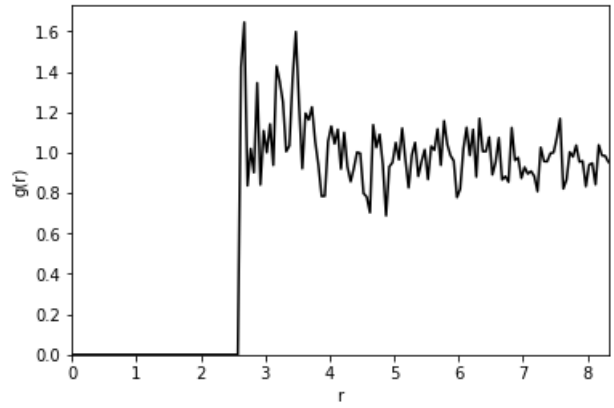

(f) Perfect Random

Figure 4.10: The same as Fig.4.5 except for a system with particle volume fraction of f_v=0.10.

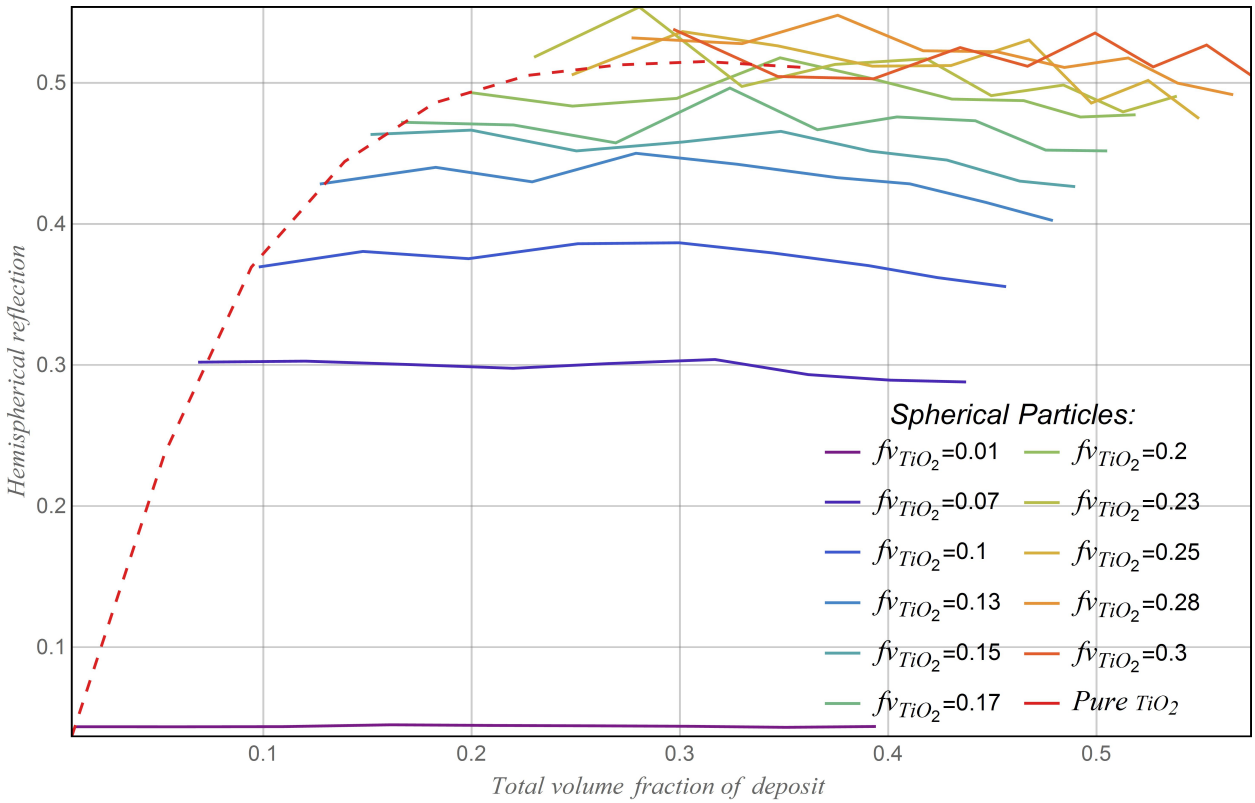

Figure 4.11: PWPP computations for spectral hemispherical reflectance by a composite modeled deposit with dimensionless thickness of 20 composed of spherical spacer and TiO_2 particles with the same size $x_{TiO_2} = x_{spacer} = 1.302$.

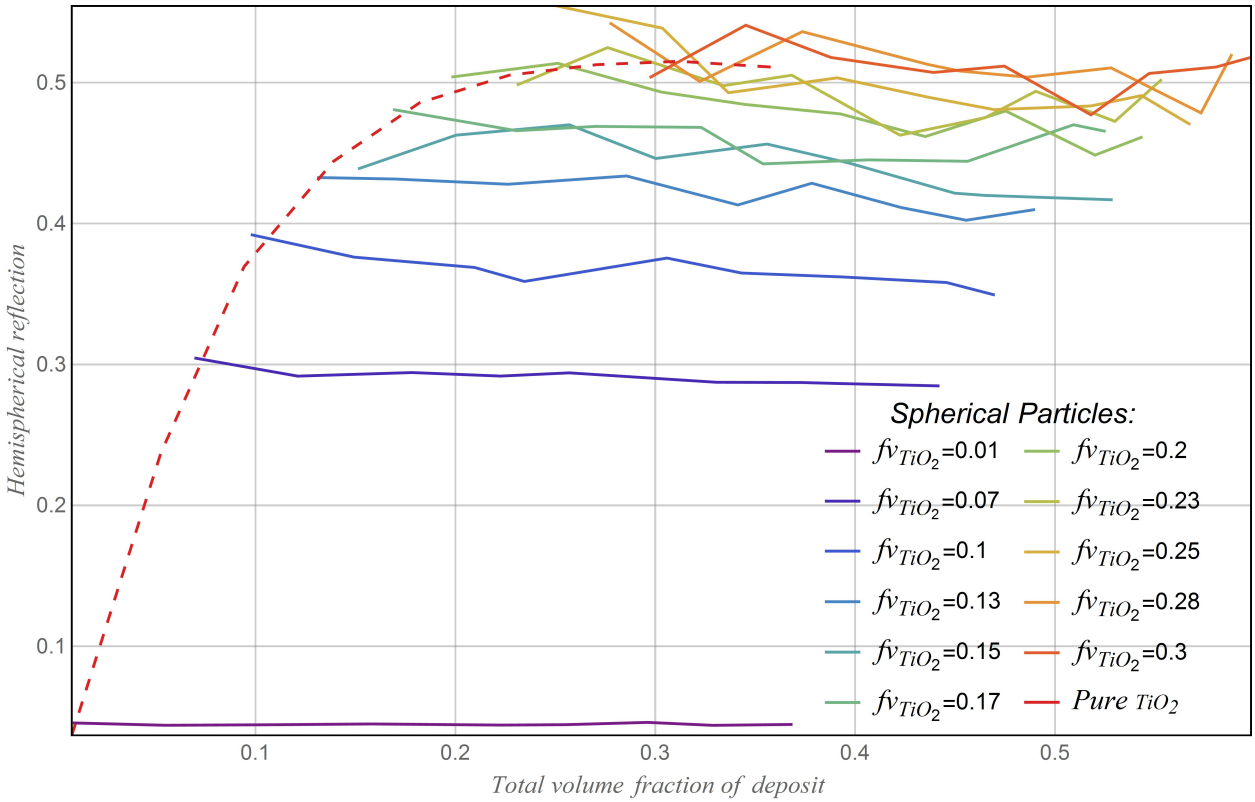

Figure 4.12: The same as Fig.4.11, except that $x_{TiO_2} = 1.302$ and $x_{spacer} = 3.906$.

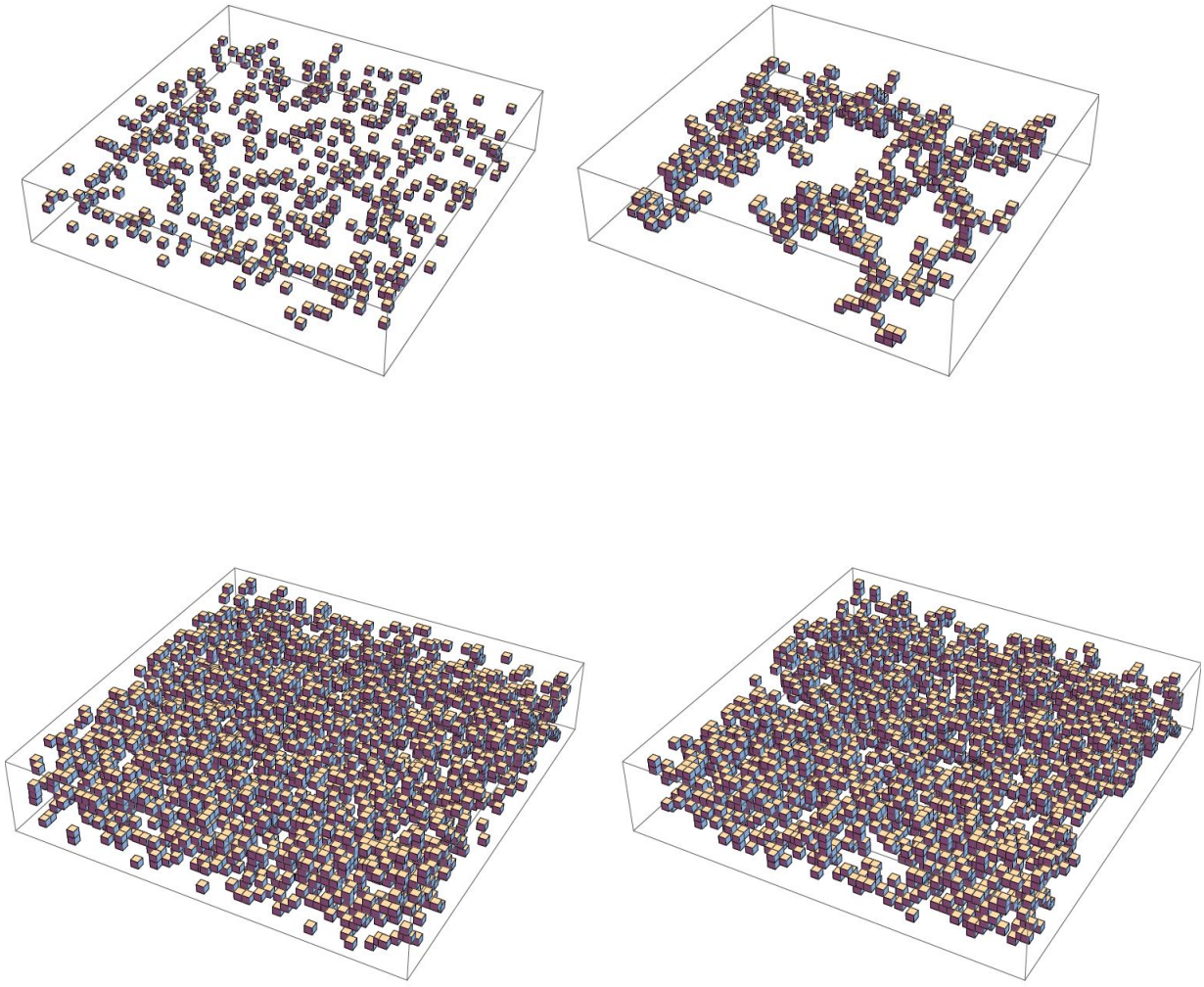

Figure 4.13: Top graphics represent the system of volume fraction of f_v=0.01 and the bottom ones shows the deposit of f_v=0.05.

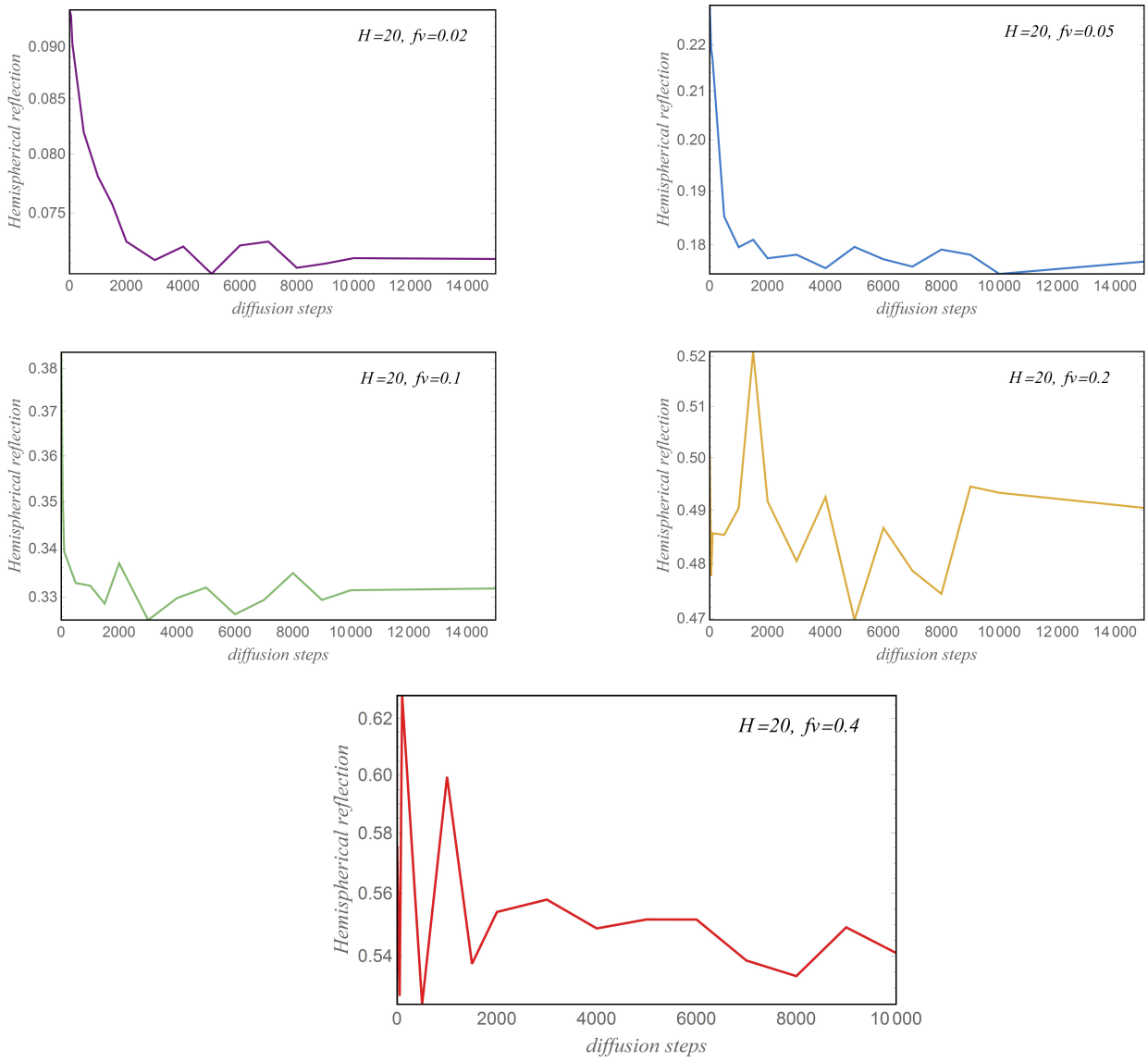

Figure 4.14: PWPP computations for hemispherical reflectance by cluster aggregated systems consisting of TiO_2 spherical particles (m=2.7) with different particle volume fractions.

4.3 Conclusion and future works

In this research, we presented the simulation results for a system composed of titanium dioxide particles and/or mixed system of titania and non–TiO_2 particles in different geometrical shapes with various structure. Computations were simulated using the PWPP method that was able to run for real pigment-binder coating condition i.e., optically thick layers.

One implication of the results was that non–TiO_2 particles with refractive index of m=2.4 and 2.1 were incapable of reproducing the spectral reflection by TiO_2 particles. Also, calculation based on the assumption of spherical particles does not affect the scattering properties of the test deposit. However, computations for different particle sizes of materials types 1 and 2 shows that the dependency of the reflection on the particle size is more significant. Also, results demonstrated that adding particles with the refractive index of m=2.4 to the pure TiO_2 has increased the directional-hemispherical reflection. We also computed the hemispherical reflection for a perfect lattice deposit as the randomness was added to the system. One could see a sudden increase of reflection at specific values of the particle packing density. The reflection dependency on particle aggregation can be more complex if different factors can be included in the problem, such has sticking probability, particle rotation, and particle shape. To examine these effects further calculations are required. Preliminary results indicate that the spacer particles do not significantly influence reflectance from initially particle systems; it could, however, change how subsequent particle aggregation alters the reflection.

Various extensions to this work is possible. Further work is needed to study the effects of absorbing pigment particles on film transmission. In this regard, one can also examine the spectral scattering properties by particulate system composed of a binary mixture of TiO_2 and absorbing pigment particles. As mentioned earlier, the dependency of aggregated system to the sticking probability, particle rotation, and particle shape is unknown. We

intend to identify conditions which minimize the coherent and diffuse transmission of visible light through the film, as a function of particle characteristics and film thickness.

Chapter 5

Conclusions, summary, future work.

5.1 Summary and conclusion

Due to new advanced techniques to detect and identify particulate material in the remote sensing methods, there is a demonstrated need for a detailed understanding of how different chemical and morphological properties of a deposition of particulate material alter the observable radiometric and polarimetric characteristics. To this end, we have developed and applied direct simulation methods based on superposition solutions to Maxwell's wave equations to predict the change in spectral bidirectional reflectivity, absorptivity, and polarized scattering fields. The multiple sphere T-matrix method (MSTM) was initially used to determine the bidirectional reflectance and transmittance from plane parallel layers of randomly distributed, wavelength—sized particles. The method is based on an exact superposition solution to Maxwell's time harmonic wave equations for a deposit of spherical particles that are exposed to a plane incident wave. We use a FORTRAN-90 implementation of this solution (the Multiple Sphere T Matrix (MSTM) code), coupled with parallel computational platforms, to directly simulate the reflection from particle layers via a configurational averaging strategy. We also used the phenomenological modeling methods based on the radiative transport equation to observe under what conditions the RTE methods can accurately predict the scattering properties (spectral-directional reflection and absorption) of spherical particle deposits and what the error is between the exact results and those generated via the macroscopic RTE.

The results are plotted for refractive indices of m=1.54, 2.5, 1.9+0.03i, 1.46+2.75i, and 0.15+3.15i representing pigments, silica, quartz, and gold particles. Plots show hemispherical reflection properties as a function of target optical depth for increasing values of the particle volume fraction. The RTE results tends to agree well with the MSTM outputs when the particle packing density of the system is less than around 0.05. For larger particle volume fractions, MSTM results monotonically increase or decrease from the RTE data. In response to the size parameter effects, we examined different particle size parameter ranging from 1 to 4 for the above—mentioned materials. One can see from results that the particle size parameter affects the spectral reflectance behavior in dense media. For material with large imaginary refractive index, the particle volume fraction have a larger effect on larger particle size parameter. While, for less absorbent material, the difference between the RTE and MSTM results are greater for smaller particle size parameter. The simulation data are also presented for directional absorption. As can be seen, surprisingly the volume packing density of the system and the particle size parameter do not significantly affect absorption properties.

In the chapter 3, a direct simulation method has been used in order to assess the radiative transfer equation (RTE) when applied to high volume fraction conditions when the polarization effects are included. As mentioned before, the RTE is strictly valid only in the limit of vanishing particle packing density. Because of this issue, the validity of the RTE when applied to densely packed media is questionable. The plane wave plane parallel method (PWPP) has been used as the exact simulation methodology for deposits of spherical, wavelength-size particles. This method is based on a DDA formulation in which a unit cell, representing the particulate medium, is repeated periodically in the lateral directions to infinity. The algorithm is implemented using FORTRAN-90 coupled with the parallel computational platform-MPI. Simulations have performed on sufficiently thick deposit layers to account for particle interaction effects. The adding and doubling technique is used as the solution to the VRTE. In this model, the bulk coefficients of the absorbing and scattering

media (the extinction coefficient, albedo, and scattering phase function) are obtained by Mie theory. Another objective of this research was to examine features in EM scattering that arise due to multiple scattering in dense particulate systems. One of these phenomena is Opposition effect the so-called coherent backscattering and shadow-hiding effects which are essential for interpretation of polarimetric remote sensing observations. The relationship between the photometric opposition effects by different physical and optical properties of the scattering particles, such as composition, sizes, structure, and density has been studied

Computations are performed for the refractive indices of 1.31 and 1.5+0.01 representing ice and mineral particles with size parameter of one and two. The particle volume fraction of the samples varies from around 0.05 to 0.3 for a fixed deposit optical thickness. The results unambiguously demonstrated that the PWPP and VRTE predictions of the directional reflected and transmitted Stokes vectors converge when the particle volume fraction is below five percent and that is consistent with our previous results. For higher particle packing density, the PWPP results for S_{11} and S_{ij}/S_{11} depart monotonically from ones generated by the VRTE. Also of interest in our data are the results for the coherent backscattering. In order to study this scattering phenomenon we concentrate on the results of S_{11} and $-S_{12}/S_{11}$ by the PWPP method in the range of $160 \leq \theta \leq 180$. We have observed a strong dependency of brightness opposition peaks and polarization opposition depths to the particle volume fraction and size parameter.

In the last chapter, we conduct simulations to study the hemispherical reflection of titanium dioxide layers and compare the results with the scattering properties by non–TiO_2 coating materials. The primary motivation of this project stems from the potential of using non-titanium dioxide pigment particles to reproduce the scattering properties by titania films. The TiO_2 refractive index used in the calculations was 2.7. Two categories of non-absorbing particles represented by refractive indices of m=2.1 and m=2.4 are examined. The particles have five values of characteristic size parameters from 200 nm to 300 nm. Computations for

each set deposit are made using five values of target thickness ranging from 5 to 30 as the packing density increases from 10% to 30%. The study use a benchmark description, based on the simulated scattering properties by TiO_2 deposited layers of thickness H=20 consisted of spherical particles with size parameters of 1.302 and volume fraction of 0.2. The incident field at wavelength of 560 nm is normal to the model deposit. A FORTRAN implementation of the PPWP formulation has been used to perform the simulations on the Auburn University HOPPER cluster. For each set of model parameters, the directional-hemispherical reflection is calculated by averaging over 10 different configurations using polydispersion spherical distribution. There are several implication of the results plotted in the chapter 4. The following observations are

Highlighted: 1) For a fixed film thickness, reflection is maximized for TiO_2 particles volume fractions around 20%. 2) Pigment particles with m=2.4, 2.1 produce significantly lower reflection relative to TiO2. 3) Spherical particles produce largest reflection for a fixed volume of particle material. 4)Reflection by a lattice structure of TiO_2 particles has strong spectral and concentration dependence, yet relatively minor deviations from a lattice structure produces reflection behavior typical of a random system. 5) Preliminary results indicate that the adding the spacer particles does not significantly influence reflectance from initially unaggregated particle systems; it could, however, change how subsequent particle aggregation alters the reflection.

5.2 Future work

As mentioned before, it is well known that the radiative transfer equation (RTE) is strictly valid only in the limit of vanishing particle volume fraction. Because of this issue, the validity of the RTE when applied to densely packed media is questionable. In the future, we hope, if possible, to use a direct simulation method to extend and modify the phenomenological RTE or VRTE so it can applied to high volume pacing density conditions.

Observations in the cosmic dust and planetary aerosols indicate that the majority of these environments contains large aggregate structures which affect the light scattering characteristics of the dust. Opposition effect behaviors is one of the essential factors to study scattering characteristics of by cosmic dust and planetary regolith in remote sensing techniques. To better understand how the optical, chemical properties, and morphology of a fractal aggregates alter the scattering properties, we are carrying out detailed numerical simulations of scattering from modeled particulate media. The samples will be modeled as fractal clusters consisted of spherical shape monomers. One important factor to study the multiple scattering effects between the monomers is aggregate morphology. In order to study this effect, we will consider chain-like fractals which have cluster dimension smaller than 2 and densely packed pile clusters with fractal dimension close to 3. Emphasis will be placed on how aggregation among the particles in the medium – occurring in either ballistic or diffusive mechanisms – alters the height and width of the coherent backscattering peak and the negative polarization branch near zero phase angle.

The reflection dependency on particle aggregation can be more complex if different factors can be included in the problem, such has sticking probability, particle rotation, and particle shape. So the next step in pigment–binder coatings simulations is to examine the dependency of reflectance radiation fields on the above—mentioned parameters. We would like to identify conditions which minimize the coherent and diffuse transmission of visible light through the film, as a function of particle characteristics and film thickness. In particular, we plan to examine the effect of absorbing pigments or a binary mixture of TiO_2 and absorbing pigment on film transmission.

References

[1] MA Al-Nimr and VS Arpaci. Radiative properties of interacting particles. *Journal of heat transfer*, 114(4):950–957, 1992.

[2] M Benassi, RDM Garcia, and CE Siewert. A generalized spherical harmonics solution basic to the scattering of polarized light. *Zeitschrift für angewandte Mathematik und Physik ZAMP*, 36(1):70–88, 1985.

[3] MQ Brewster and CL Tien. Radiative transfer in packed fluidized beds: dependent versus independent scattering. *Journal of Heat Transfer*, 104(4):573–579, 1982.

[4] VN Bringi, VV Varadan, and VK Varadan. Coherent wave attenuation by a random distribution of particles. *Radio Science*, 17(5):946–952, 1982.

[5] Shelly D Burnside, Valery Shklover, Christophe Barbé, Pascal Comte, Francine Arendse, Keith Brooks, and Michael Grätzel. Self-organization of tio2 nanoparticles in thin films. *Chemistry of materials*, 10(9):2419–2425, 1998.

[6] IM Butterfield, PA Christensen, A Hamnett, KE Shaw, GM Walker, SA Walker, and CR Howarth. Applied studies on immobilized titanium dioxide films ascatalysts for the photoelectrochemical detoxification of water. *Journal of applied electrochemistry*, 27(4):385–395, 1997.

[7] Maria I Cabrera, Orlando M Alfano, and Alberto E Cassano. Absorption and scattering coefficients of titanium dioxide particulate suspensions in water. *The Journal of Physical Chemistry*, 100(51):20043–20050, 1996.

[8] JD Cartigny, Y Yamada, and CL Tien. Radiative transfer with dependent scattering by particles: part 1—theoretical investigation. *Journal of heat transfer*, 108(3):608–613, 1986.

[9] Kenneth M Case and Paul Frederick Zweifel. Linear transport theory. 1967.

[10] Edmond D Cashwell and Cornelius Joseph Everett. A practical manual on the monte carlo method for random walk problems. 1959.

[11] CK Chan and CL Tien. Radiative transfer in packed spheres. *Journal of Heat Transfer*, 96(1):52–58, 1974.

[12] Subrahmanyan Chandrasekhar. *Radiative transfer*. 2013.

[13] Patrick C Chaumet, Adel Rahmani, and Garnett W Bryant. Generalization of the coupled dipole method to periodic structures. *Physical Review B*, 67(16):165404, 2003.

[14] Patrick C Chaumet and Anne Sentenac. Numerical simulations of the electromagnetic field scattered by defects in a double-periodic structure. *Physical Review B*, 72(20):205437, 2005.

[15] Hean-Teik Chuah, Saibun Tjuatja, Adrian K Fung, and Jonathan W Bredow. Radar backscatter from a dense discrete random medium. *IEEE transactions on geoscience and remote sensing*, 35(4):892–900, 1997.

[16] Stuart W Churchill, George Charles Clark, and Cedomir M Sliepcevich. Light-scattering by very dense monodispersions of latex particles. *Discussions of the Faraday Society*, 30:192–199, 1960.

[17] Kinsell L Coulson, Jitendra V Dave, and Z Sckera. Tables related to radiation emerging from a planetary atmosphere with rayleigh scattering. 1960.

[18] Boris Davison and John Bradbury Sykes. Neutron transport theory. 1957.

[19] JF De Haan, PB Bosma, and JW Hovenier. The adding method for multiple scattering calculations of polarized light. *Astronomy and Astrophysics*, 183:371–391, 1987.

[20] JF De Haan, PB Bosma, and JW Hovenier. The adding method for multiple scattering calculations of polarized light. *Astronomy and Astrophysics*, 183:371–391, 1987.

[21] C Devaux and CE Siewert. Thef n method for radiative transfer problems without azimuthal symmetry. *Zeitschrift für Angewandte Mathematik und Physik (ZAMP)*, 31(5):592–604, 1980.

[22] Howard DeVoe. Optical properties of molecular aggregates. i. classical model of electronic absorption and refraction. *The Journal of chemical physics*, 41(2):393–400, 1964.

[23] Howard DeVoe. Optical properties of molecular aggregates. ii. classical theory of the refraction, absorption, and optical activity of solutions and crystals. *The Journal of chemical physics*, 43(9):3199–3208, 1965.

[24] Zh M Dlugach and MI Mishchenko. Coherent backscattering and opposition effects observed in some atmosphereless bodies of the solar system. *Solar System Research*, 47(6):454–462, 2013.

[25] Bruce T Draine. The discrete-dipole approximation and its application to interstellar graphite grains. *The Astrophysical Journal*, 333:848–872, 1988.

[26] Bruce T. Draine and Piotr J. Flatau. Discrete-dipole approximation for scattering calculations. *J. Opt. Soc. Am. A*, 11(4):1491–1499, Apr 1994.

[27] Bruce T Draine and Piotr J Flatau. Discrete-dipole approximation for periodic targets: theory and tests. *JOSA A*, 25(11):2693–2703, 2008.

[28] Bruce T Draine and Jeremy Goodman. Beyond clausius-mossotti-wave propagation on a polarizable point lattice and the discrete dipole approximation. *The Astrophysical Journal*, 405:685–697, 1993.

[29] James J Duderstadt and William Russell Martin. Transport theory. *Transport theory., by Duderstadt, JJ; Martin, WR. Chichester (UK): John Wiley & Sons, 10+ 613 p.*, 1979.

[30] Clifton E Dungey and Craig F Bohren. Light scattering by nonspherical particles: a refinement to the coupled-dipole method. *JOSA A*, 8(1):81–87, 1991.

[31] Willem PC Duyvesteyn, Bruce James Sabacky, Dirk Edmund Victor Verhulst, Paul George West-Sells, Timothy Malcome Spitler, Andrew Vince, James R Burkholder, and Bernardus Josephus Paulus Maria Huls. Processing titaniferous ore to titanium dioxide pigment, April 23 2002. US Patent 6,375,923.

[32] Willem PC Duyvesteyn, Timothy Malcome Spitler, Bruce James Sabacky, Andrew Vince, and Jan Prochazka. Processing aqueous titanium solutions to titanium dioxide pigment, April 15 2003. US Patent 6,548,039.

[33] Andrea Ferrara, Simone Bianchi, Ralf-Jürgen Dettmar, and Carlo Giovanardi. The effect of light scattering by dust in galactic halos on emission-line ratios. *The Astrophysical Journal Letters*, 467(2):L69, 1996.

[34] Piotr J Flatau. Improvements in the discrete-dipole approximation method of computing scattering and absorption. *Optics letters*, 22(16):1205–1207, 1997.

[35] PJ Flatau and BT Draine. Fast near field calculations in the discrete dipole approximation for regular rectilinear grids. *Optics express*, 20(2):1247–1252, 2012.

[36] M Formenti, F Juillet, P Meriaudeau, and SJ Teichner. Heterogeneous photocatalysis for partial oxidation of paraffins. *Chemical Technology*, (NNOV):680–+, 1971.

[37] RDM Garcia and CE Siewert. A generalized spherical harmonics solution for radiative transfer models that include polarization effects. *Journal of Quantitative Spectroscopy and Radiative Transfer*, 36(5):401–423, 1986.

[38] C Garzella, E Comini, E Tempesti, C Frigeri, and G Sberveglieri. Tio2 thin films by a novel sol–gel processing for gas sensor applications. *Sensors and Actuators B: Chemical*, 68(1-3):189–196, 2000.

[39] Manuel Jesús Gázquez, Juan Pedro Bolívar, Rafael Garcia-Tenorio, and Federico Vaca. A review of the production cycle of titanium dioxide pigment. *Materials Sciences and Applications*, 5(07):441, 2014.

[40] T Gerfin, M Grätzel, and L Walder. Molecular and supramolecular surface modification of nanocrystalline tio2 films: Charge-separating and charge-injecting devices. *Progress in inorganic chemistry: molecular level artificial photosynthetic materials*, pages 345–393, 1996.

[41] George H Goedecke, Sean G O'Brien, et al. Scattering by irregular inhomogeneous particles via the digitized green's function algorithm. *Applied Optics*, 27(12):2431–2438, 1988.

[42] JJ Goodman, Bruce T Draine, Piotr J Flatau, et al. Application of fast-fourier-transform techniques to the discrete-dipole approximation. *Opt. Lett*, 16(15):1198–1200, 1991.

[43] P Grandjean and CE Siewert. The f n method in neutron-transport theory. part ii: Applications and numerical results. *Nuclear Science and Engineering*, 69(2):161–168, 1979.

[44] IP Grant and GE Hunt. Solution of radiative transfer problems using the invariant sn method. *Monthly Notices of the Royal Astronomical Society*, 141(1):27–41, 1968.

[45] JI Hage and J Mayo Greenberg. A model for the optical properties of porous grains. *The Astrophysical Journal*, 361:251–259, 1990.

[46] James E Hansen. Multiple scattering of polarized light in planetary atmospheres. part i. the doubling method. *Journal of the Atmospheric Sciences*, 28(1):120–125, 1971.

[47] James E Hansen. Multiple scattering of polarized light in planetary atmospheres part ii. sunlight reflected by terrestrial water clouds. *Journal of the Atmospheric Sciences*, 28(8):1400–1426, 1971.

[48] James Edward Hansen. Radiative transfer by doubling very thin layers. *The Astrophysical Journal*, 155:565–573, 1969.

[49] Bruce Hapke. *Theory of reflectance and emittance spectroscopy*. Cambridge university press, 2012.

[50] Bruce Hapke, Robert Nelson, and William Smythe. The opposition effect of the moon: Coherent backscatterandshadow hiding. *Icarus*, 133(1):89–97, 1998.

[51] Paul Helfenstein, Joseph Veverka, and John Hillier. The lunar opposition effect: A test of alternative models. *Icarus*, 128(1):2–14, 1997.

[52] Laurent Hespel, Stéphane Mainguy, and Jean-Jacques Greffet. Radiative properties of scattering and absorbing dense media: theory and experimental study. *Journal of Quantitative Spectroscopy and Radiative Transfer*, 77(2):193–210, 2003.

[53] HC Hottel, AF Sarofim, WH Dalzell, and IA Vasalos. Optical properties of coatings. effect of pigment concentration. *AIAA Journal*, 9(10):1895–1898, 1971.

[54] Joop W Hovenier, Cornelis VM van der Mee, and Helmut Domke. *Transfer of polarized light in planetary atmospheres: basic concepts and practical methods*, volume 318. 2014.

[55] JW Hovenier. Multiple scattering of polarized light in planetary atmospheres. *Astronomy and Astrophysics*, 13:7, 1971.

[56] William M Irvine. Multiple scattering by large particles. *The Astrophysical Journal*, 142:1563, 1965.

[57] Akira Ishimaru. Wave propagation and scattering in random media. volume 1-single scattering and transport theory. *Wave propagation and scattering in random media. Vol. 1, by Ishimaru, A.. New York (NY, USA): Academic Press, 267 pp. Research supported by the US Air Force, NSF, and NIH, 1978*, 1, 1978.

[58] Akira Ishimaru and Yasuo Kuga. Attenuation constant of a coherent field in a dense distribution of particles. *JOSA*, 72(10):1317–1320, 1982.

[59] Magdy F Iskander, HY Chen, and JE Penner. Optical scattering and absorption by branched chains of aerosols. *Applied optics*, 28(15):3083–3091, 1989.

[60] G Ito, JA Arnold, and TD Glotch. T-matrix and radiative transfer hybrid models for densely packed particulates at mid-infrared wavelengths. *Journal of Geophysical Research: Planets*, 122(5):822–838, 2017.

[61] Hironobu Iwabuchi. Efficient monte carlo methods for radiative transfer modeling. *Journal of the atmospheric sciences*, 63(9):2324–2339, 2006.

[62] John David Jackson. Classical electromagnetics. *Wiley, New York*, 1975.

[63] Andreas Kafizas, Charles W Dunnill, and Ivan P Parkin. The relationship between photocatalytic activity and photochromic state of nanoparticulate silver surface loaded

titanium dioxide thin-films. *Physical Chemistry Chemical Physics*, 13(30):13827–13838, 2011.

[64] Massoud Kaviany and BP Singh. Radiative heat transfer in porous media. *Advances in Heat Transfer*, 23(23):133–186, 1993.

[65] Shahed UM Khan, Mofareh Al-Shahry, and William B Ingler. Efficient photochemical water splitting by a chemically modified n-tio2. *science*, 297(5590):2243–2245, 2002.

[66] Klaus P Kühn, Iris F Chaberny, Karl Massholder, Manfred Stickler, Volker W Benz, Hans-Günther Sonntag, and Lothar Erdinger. Disinfection of surfaces by photocatalytic oxidation with titanium dioxide and uva light. *Chemosphere*, 53(1):71–77, 2003.

[67] TJ Kulp, RL Sommersa, KL Krafcika, BE Millsa, TA Reichardta, JK Dorrancea, CF LaCasse IVb, KH Fuerschbachb, and J Cravenb. Ideal-system morphology and reflectivity measurements for radiative-transfer model development and validation. In *Proc. of SPIE Vol*, volume 9840, pages 98400H–1, 2016.

[68] S Kumar and CL Tien. Dependent absorption and extinction of radiation by small particles. *Journal of heat transfer*, 112(1):178–185, 1990.

[69] AA Lacis, J Chowdhary, B Cairns, and MI Mishchenko. Modeling errors in diffuse-sky radiation. *Geophys. Res. Lett*, 25:135–138, 1998.

[70] Gerardo Larramona, Christophe Choné, Alain Jacob, Daisuke Sakakura, Bruno Delatouche, Daniel Péré, Xavier Cieren, Masashi Nagino, and Rocío Bayón. Nanostructured photovoltaic cell of the type titanium dioxide, cadmium sulfide thin coating, and copper thiocyanate showing high quantum efficiency. *Chemistry of materials*, 18(6):1688–1696, 2006.

[71] J Lenoble. Application de la methode des harmoniques spheriques au cas de la diffusion anisotrope. *COMPTES RENDUS HEBDOMADAIRES DES SEANCES DE L ACADEMIE DES SCIENCES*, 252(14):2087, 1961.

[72] Kuo-Nan Liou. *An introduction to atmospheric radiation*, volume 84. Academic press, 2002.

[73] Hui Lu, Toshio Koike, Hiroyuki Tsutsui, Tobias Graf, D Kuria, Hydeyuki Fujii, and M Mourita. A radiative transfer model for soil media with considering the volume effects of soil particles: Field observation and numerical simulation. In *Geoscience and Remote Sensing Symposium, 2006. IGARSS 2006. IEEE International Conference on*, pages 1736–1739. IEEE, 2006.

[74] LX Ma, JY Tan, JM Zhao, FQ Wang, and CA Wang. Multiple and dependent scattering by densely packed discrete spheres: Comparison of radiative transfer and maxwell theory. *Journal of Quantitative Spectroscopy and Radiative Transfer*, 187:255–266, 2017.

[75] Y Ma, VK Varadan, and VV Varadan. Enhanced absorption due to dependent scattering. *Journal of heat transfer*, 112(2):402–407, 1990.

[76] Daniel Mackowski. Van de hulst essay: The dda, the rte, and the computation of scattering by plane parallel layers of particles. *Journal of Quantitative Spectroscopy and Radiative Transfer*, 189:43–59, 2017.

[77] Daniel Mackowski and Bahareh Ramezan Pour. A plane wave model for direct simulation of reflection and transmission by discretely inhomogeneous plane parallel media. *Journal of Quantitative Spectroscopy and Radiative Transfer*, 2018.

[78] Daniel W Mackowski. Calculation of total cross sections of multiple-sphere clusters. *JOSA A*, 11(11):2851–2861, 1994.

[79] Daniel W Mackowski. Calculation of total cross sections of multiple-sphere clusters. *JOSA A*, 11(11):2851–2861, 1994.

[80] Daniel W Mackowski and Michael I Mishchenko. Calculation of the t matrix and the scattering matrix for ensembles of spheres. *JOSA A*, 13(11):2266–2278, 1996.

[81] Daniel W Mackowski and Michael I Mishchenko. Direct simulation of multiple scattering by discrete random media illuminated by gaussian beams. *Physical Review A*, 83(1):013804, 2011.

[82] DW Mackowski and MI Mishchenko. A multiple sphere t-matrix fortran code for use on parallel computer clusters. *Journal of Quantitative Spectroscopy and Radiative Transfer*, 112(13):2182–2192, 2011.

[83] JR Maiorino and CE Siewert. The fn method for polarization studies—ii numerical results. *Journal of Quantitative Spectroscopy and Radiative Transfer*, 24(2):159–165, 1980.

[84] Pekka I Makinen. Coated titanium dioxide pigment and a process for the production of the same, March 8 1983. US Patent 4,375,989.

[85] VA Markel. Coupled-dipole approach to scattering of light from a one-dimensional periodic dipole structure. *Journal of Modern Optics*, 40(11):2281–2291, 1993.

[86] Andrew Mills and Soo-Keun Lee. A web-based overview of semiconductor photochemistry-based current commercial applications. *Journal of Photochemistry and Photobiology A: Chemistry*, 152(1-3):233–247, 2002.

[87] MI Mishchenko. The fast invariant imbedding method for polarized light: computational aspects and numerical results for rayleigh scattering. *Journal of Quantitative Spectroscopy and Radiative Transfer*, 43(2):163–171, 1990.

[88] MI Mishchenko. The angular width of the coherent back-scatter opposition effect: an application to icy outer planet satellites. *Astrophysics and space science*, 194(2):327–333, 1992.

[89] Michael I Mishchenko. *Electromagnetic scattering by particles and particle groups: an introduction*. Cambridge University Press, 2014.

[90] Michael I Mishchenko, Janna M Dlugach, Edgard G Yanovitsku, and Nadia T Zakharova. Bidirectional reflectance of flat, optically thick particulate layers: an efficient radiative transfer solution and applications to snow and soil surfaces. 1999.

[91] Michael I Mishchenko, Janna M Dlugach, Maxim A Yurkin, Lei Bi, Brian Cairns, Li Liu, R Lee Panetta, Larry D Travis, Ping Yang, and Nadezhda T Zakharova. First-principles modeling of electromagnetic scattering by discrete and discretely heterogeneous random media. *Physics Reports*, 632:1–75, 2016.

[92] Michael I Mishchenko, Dennis H Goldstein, Jacek Chowdhary, and Arthur Lompado. Radiative transfer theory verified by controlled laboratory experiments. *Optics letters*, 38(18):3522–3525, 2013.

[93] Michael I Mishchenko, Jean-Marc Luck, and Theo M Nieuwenhuizen. Full angular profile of the coherent polarization opposition effect. *JOSA A*, 17(5):888–891, 2000.

[94] Michael I Mishchenko, Larry D Travis, and Andrew A Lacis. *Multiple scattering of light by particles: radiative transfer and coherent backscattering*. Cambridge University Press, 2006.

[95] Alexander E Moskalensky, Alyona L Litvinenko, Vyacheslav M Nekrasov, and Maxim A Yurkin. A physical model of blood platelets shape and its effect on light scattering. In *Electromagnetic Theory (EMTS), 2016 URSI International Symposium on*, pages 583–585. IEEE, 2016.

[96] Saba Mudaliar. Some issues with using radiative transfer approach to scattering from layered random media with rough interfaces. *IEEE Transactions on Antennas and Propagation*, 57(11):3646–3654, 2009.

[97] K Muinonen, MI Mishchenko, JM Dlugach, E Zubko, A Penttilä, and G Videen. Coherent backscattering verified numerically for a finite volume of spherical particles. *The Astrophysical Journal*, 760(2):118, 2012.

[98] Karri Muinonen, Johannes Markkanen, Antti Penttilä, Timo Väisänen, and Jouni Peltoniemi. Multiple scattering by dense random media: Numerical solution. In *Electromagnetic Theory (EMTS), 2016 URSI International Symposium on*, pages 400–403. IEEE, 2016.

[99] Charles David Musick, Austin H Reid Jr, and Lu Zhang. Titanium dioxide nanopowder manufacturing process, April 24 2007. US Patent 7,208,126.

[100] VJ Nagpal, RM Davis, and SB Desu. Novel thin films of titanium dioxide particles synthesized by a sol-gel process. *Journal of materials research*, 10(12):3068–3078, 1995.

[101] RM Nelson, BW Hapke, WD Smythe, and LJ Spilker. The opposition effect in simulated planetary regoliths. reflectance and circular polarization ratio change at small phase angle. *Icarus*, 147(2):545–558, 2000.

[102] Thomas H Painter and Jeff Dozier. Measurements of the hemispherical-directional reflectance of snow at fine spectral and angular resolution. *Journal of Geophysical Research: Atmospheres*, 109(D18), 2004.

[103] Isabel Pastoriza-Santos, Dmitry S Koktysh, Arif A Mamedov, Michael Giersig, Nicholas A Kotov, and Luis M Liz-Marzán. One-pot synthesis of ag@ tio2 core- shell nanoparticles and their layer-by-layer assembly. *Langmuir*, 16(6):2731–2735, 2000.

[104] Antti Penttilä. Quasi-specular reflection from particulate media. *Journal of Quantitative Spectroscopy and Radiative Transfer*, 131:130–137, 2013.

[105] Patricio Piedra and Hans Moosmüller. Optical losses of photovoltaic cells due to aerosol deposition: Role of particle refractive index and size. *Solar Energy*, 155:637–646, 2017.

[106] Karly M Pitman, Michael J Wolff, and Geoffrey C Clayton. Application of modern radiative transfer tools to model laboratory quartz emissivity. *Journal of Geophysical Research: Planets*, 110(E8), 2005.

[107] Scott A Prahl. The adding-doubling method. In *Optical-thermal response of laser-irradiated tissue*, pages 101–129. 1995.

[108] Scott A Prahl, Martin JC van Gemert, and Ashley J Welch. Determining the optical properties of turbid media by using the adding–doubling method. *Applied optics*, 32(4):559–568, 1993.

[109] Edward M Purcell and Carlton R Pennypacker. Scattering and absorption of light by nonspherical dielectric grains. *The Astrophysical Journal*, 186:705–714, 1973.

[110] Bahareh Ramezan pour and Daniel Mackowski. Radiative transfer equation and direct simulation prediction of reflection and absorption by particle deposits. *Journal of Quantitative Spectroscopy and Radiative Transfer*, 189:361–368, 2017.

[111] Thomas A Reichardt and Thomas J Kulp. Radiative transfer modeling of surface chemical deposits. In *SPIE Defense+ Security*, pages 98400M–98400M. International Society for Optics and Photonics, 2016.

[112] Makiko Sato, Kiyoshi Kawabata, and James E Hansen. A fast invariant imbedding method for multiple scattering calculations and an application to equivalent widths of co2 lines on venus. *The Astrophysical Journal*, 216:947–962, 1977.

[113] Roland Schmehl, Brent M Nebeker, E Dan Hirleman, et al. Discrete-dipole approximation for scattering by features on surfaces by means of a two-dimensional fast fourier transform technique. *JOSA A*, 14(11):3026–3036, 1997.

[114] FM Schulz and K Stamnes. Angular distribution of the stokes vector in a plane-parallel, vertically inhomogeneous medium in the vector discrete ordinate radiative transfer (vdisort) model. *Journal of Quantitative Spectroscopy and Radiative Transfer*, 65(4):609–620, 2000.

[115] FM Schulz, K Stamnes, and F Weng. Vdisort: an improved and generalized discrete ordinate method for polarized (vector) radiative transfer. *Journal of quantitative spectroscopy and radiative transfer*, 61(1):105–122, 1999.

[116] Jonathan Sherman. Nanoparticulate titanium dioxide coatings, and processes for the production and use thereof, November 25 2003. US Patent 6,653,356.

[117] Yu Shkuratov, A Ovcharenko, E Zubko, O Miloslavskaya, K Muinonen, J Piironen, R Nelson, W Smythe, V Rosenbush, and P Helfenstein. The opposition effect and negative polarization of structural analogs for planetary regoliths. *Icarus*, 159(2):396–416, 2002.

[118] CE Siewert. A discrete-ordinates solution for radiative-transfer models that include polarization effects. *Journal of Quantitative Spectroscopy and Radiative Transfer*, 64(3):227–254, 2000.

[119] CE Siewert and P Benoist. The f n method in neutron-transport theory. part i: Theory and applications. *Nuclear Science and Engineering*, 69(2):156–160, 1979.

[120] Threes G Smijs and Stanislav Pavel. Titanium dioxide and zinc oxide nanoparticles in sunscreens: focus on their safety and effectiveness. *Nanotechnology, science and applications*, 4:95, 2011.

[121] S Sukhov, D Haefner, and A Dogariu. Coupled dipole method for modeling optical properties of large-scale random media. *Physical Review E*, 77(6):066709, 2008.

[122] CL Tien. Thermal radiation in packed and fluidized beds. *Journal of Heat transfer*, 110(4b):1230–1242, 1988.

[123] Benedicte Trouiller, Ramune Reliene, Aya Westbrook, Parrisa Solaimani, and Robert H Schiestl. Titanium dioxide nanoparticles induce dna damage and genetic instability in vivo in mice. *Cancer research*, 69(22):8784–8789, 2009.

[124] L Tsang and JA Kong. Multiple scattering of electromagnetic waves by random distributions of discrete scatterers with coherent potential and quantum mechanical formalism. *Journal of Applied Physics*, 51(7):3465–3485, 1980.

[125] L Tsang and JA Kong. Effective propagation constants for coherent electromagnetic wave propagation in media embedded with dielectric scatters. *Journal of Applied Physics*, 53(11):7162–7173, 1982.

[126] Leung Tsang, KH Ding, and B Wen. Dense media radiative transfer theory for dense discrete random media with particles of multiple sizes and permittivities. *Progress in Electromagnetic Research*, 6(5):181–225, 1992.

[127] Timo Väisänen, Antti Penttilä, Johannes Markkanen, and Karri Muinonen. Validation of radiative transfer and coherent backscattering for discrete random media. In *Electromagnetic Theory (EMTS), 2016 URSI International Symposium on*, pages 396–399. IEEE, 2016.

[128] H C Van de Hulst. *Multiple light scattering: tables, formulas, and applications*. Elsevier, 2012.

[129] HC Van de Hulst. Multiple light scattering. vols. 1 and 2. *Multiple light scattering. Vols.1 and 2., by van de Hulst, HC. New York, NY (USA): Academic Press, 739 p.*, 1, 1980.

[130] Vasundara V Varadan, Akhlesh Lakhtakia, and Vijay K Varadan. Scattering by three-dimensional anisotropic scatterers. *Antennas and Propagation, IEEE Transactions on*, 37(6):800–802, 1989.

[131] Gorden Videen, Evgenij Zubko, Wenbo Sun, Yuriy Shkuratov, and Alex Yuffa. Mixing rules and morphology dependence of the scatterer. *Journal of Quantitative Spectroscopy and Radiative Transfer*, 150:68–75, 2015.

[132] PC Waterman and NE Pedersen. Electromagnetic scattering by periodic arrays of particles. *Journal of applied physics*, 59(8):2609–2618, 1986.

[133] Alex Weir, Paul Westerhoff, Lars Fabricius, Kiril Hristovski, and Natalie Von Goetz. Titanium dioxide nanoparticles in food and personal care products. *Environmental science & technology*, 46(4):2242–2250, 2012.

[134] Boheng Wen, Leung Tsang, Dale P Winebrenner, and Akira . Dense medium radiative transfer theory: comparison with experiment and application to microwave remote sensing and polarimetry. *Geoscience and Remote Sensing, IEEE Transactions on*, 28(1):46–59, 1990.

[135] Fuzhong Weng. A multi-layer discrete-ordinate method for vector radiative transfer in a vertically-inhomogeneous, emitting and scattering atmosphere—i. theory. *Journal of Quantitative Spectroscopy and Radiative Transfer*, 47(1):19–33, 1992.

[136] WJ Wiscombe. On initialization, error and flux conservation in the doubling method. *Journal of Quantitative Spectroscopy and Radiative Transfer*, 16(8):637–658, 1976.

[137] Y Yamada, JD Cartigny, and CL Tien. Radiative transfer with dependent scattering by particles: Part 2—experimental investigation. *Journal of heat transfer*, 108(3):614–618, 1986.

[138] Maxim A Yurkin and Alfons G Hoekstra. The discrete dipole approximation: an overview and recent developments. *Journal of Quantitative Spectroscopy and Radiative Transfer*, 106(1):558–589, 2007.

[139] Ft Yusef-Zadeh, M Morris, and RL White. Bipolar reflection nebulae-monte carlo simulations. *The Astrophysical Journal*, 278:186–194, 1984.

[140] Hao Zhang and Kenneth J Voss. Comparisons of bidirectional reflectance distribution function measurements on prepared particulate surfaces and radiative-transfer models. *Applied optics*, 44(4):597–610, 2005.

[141] Evgenij Zubko, Yuriy Shkuratov, and Gorden Videen. Effect of morphology on light scattering by agglomerates. *Journal of Quantitative Spectroscopy and Radiative Transfer*, 150:42–54, 2015.